

LIGHT EXTRACTION AND DEGRADATION MECHANISM STUDY OF ORGANIC
LIGHT EMITTING DIODES

By

CHENG PENG

A DISSERTATION PRESENTED TO THE GRADUATE SCHOOL
OF THE UNIVERSITY OF FLORIDA IN PARTIAL FULFILLMENT
OF THE REQUIREMENTS FOR THE DEGREE OF
DOCTOR OF PHILOSOPHY

UNIVERSITY OF FLORIDA

2017

© 2017 Cheng Peng

To my mom, dad and wife

ACKNOWLEDGMENTS

First and foremost, I would like to thank my great parents, who are always loving and supporting me.

I would like to thank my wife, who I met and married during my Ph. D. career. She always helps me with her patience and wisdom.

I would like to thank my research adviser, Dr. Franky So for his guidance in both work and life. I appreciate the time and help from Dr. Stephen Pearton, Dr. Rajiv Singh, Dr. Henry Sodano, Dr. Andrew Rinzler and Dr. Brent Gila for agreeing to serve on my Ph. D. supervisory committee. I also would like Dr. Kirk Schanze for supporting me in my research.

I also want to acknowledge all my lab mates for their kind help and collaboration through my Ph. D. career. They are Do Young Kim, Cephas Small, Michael Hartel, Song Chen, Jae Woong Lee, Wooram Youn, Jesse Manders, Tzung-Han Lai, Wonhoe Koo, Shuyi Liu, Zhe Ying, Erik Klump, Danae Constantinou, Xiangyu Fu, Sujin Park, Hyeonggeun Yu, Rui Liu, Michael Sexton, Szuheng Ho, Wesley Hamlin, Jong Hyun Kim, Alessandra Pereira, Ying Chen, Dewei Zhao, Nathan Shewmon, Byoung-Hwa Kwon, Hye-Yun Park, Nilesh Barange, Monica Samal Barange, Chen Dong, Xueping Yi, Qi Dong, Shichen Yin, Dong-Hun Shin, Amin Salehi, Yuanhang Cheng, Yu Luo and Stephen Amoah. Together we made a good team.

I also want to thank other collaborators from outside the group. They are Zhenxing Pan and Jaime Leganés. I appreciate their support and help with their excellent abilities and great personalities.

Finally, I would like to say thanks to all my friends in University of Florida, around Gainesville, in North Carolina State University and in Raleigh over the past five years

and four months. They all made a colorful and great memory I will keep in my life forever.

TABLE OF CONTENTS

	<u>page</u>
ACKNOWLEDGMENTS.....	4
LIST OF FIGURES.....	8
LIST OF ABBREVIATIONS.....	11
ABSTRACT	13
CHAPTER	
1 FUNDAMENTALS OF ORGANIC SEMICONDUCTORS AND ORGANIC LIGHT EMITTING DIODES	15
Molecular Orbitals	15
Organic Semiconductor Thin Films	16
Photo-physics of Organic Molecules.....	17
Excitons and Intermolecular Exciton Energy Transfer	19
Charge Transport.....	22
Fundamentals of OLEDs.....	23
Electronics of OLEDs.....	25
Terminology of Photometry.....	27
Optics of OLEDs	28
Optical Simulation of OLEDs by Setfos.....	33
Optical Simulation of OLEDs by FDTD	38
Fabrication of OLEDs.....	41
Characterization of OLEDs	42
2 BILAYER CORRUGATED STRUCTURS AND THEIR APPLICATIONS IN OLED	50
Introduction	50
Bilayer Corrugated Structure Fabrication and Characterization	51
Corrugated OLED Fabrication and Characterization	54
Summary and Conclusions	58
3 QUANTITATIVE MODE ANALYSIS OF CORRUGATED OLEDs FROM ANLGE RESOLVED ELECTROLUMINESCENCE SPECTROSCOPY DATA (ARES).....	64
Introduction	64
Simulation of ‘Single-Crystal’ Nanostructured OLEDs	66
Calculation of Scattering Strength by Comparison between Simulation and Measurement.....	68
Calculation of Scattering Efficiency of Trapped Modes	72
Calculation of ‘Poly-Crystal’ Nanostructured OLEDs	75

Summary and Conclusions	76
4 OPTICAL SIMULATION OF CORRUGATED OLEDs BY FDTD AND THE COMBINED EFFECTS OF OPTICAL AND ELECTRICAL PERSPECTIVES	81
Introduction	81
Optical Simulation by FDTD using Reciprocity Theorem	83
Comparison between ‘Dome’ and ‘Square’ Structures	83
Comparison between ‘Rod’ and ‘Hole’ Structures.....	88
Summary and Conclusions	89
5 PHOTOLUMINESCENCE AND ELECTROLUMINESCENCE DEGRADATION ANALYSIS IN ORGANIC LIGHT EMITTING DIODES.....	95
Introduction	95
Characterization of Degradation	96
Theoretical Model	97
Emitter Concentration Effect on Stability of 4CzIPN OLEDs	98
Emitter Concentration Effect on Stability of Dopant 1 OLEDs.....	102
Mixed Host Effect on Dopant 1 OLEDs Stability	103
Summary and Conclusions	104
6 SUMMARY AND FUTURE WORK	113
LIST OF REFERENCES	116
BIOGRAPHICAL SKETCH.....	122

LIST OF FIGURES

<u>Figure</u>		<u>page</u>
1-1	A schematic showing the molecular orbitals and energy diagram of benzene. ³²	43
1-2	The Jablonski diagram showing the main electronic processes in an organic molecule.	43
1-3	A schematic showing a typical OLED stack structure. The thicknesses are not to scale.	44
1-4	A schematic showing the working mechanism of an OLED under voltage bias.	44
1-5	Schematics showing the working mechanisms of phosphorescence and TADF.	45
1-6	CIE "physiologically-relevant" luminous efficiency function (the Stockman & Sharpe cone fundamentals).	45
1-7	The CIE standard observer color matching functions.	46
1-8	The CIE 1931 color space chromaticity diagram.	46
1-9	Schematics showing the typical device configurations.	47
1-10	A schematic depicting the main energy dissipation channels in a typical bottom emission OLED.	47
1-11	The energy distribution into the main energy dissipation channels as a function of ETL thickness in a typical bottom emission OLED.	48
1-12	Multilayer impact at 520 nm of a typical bottom emission OLED.	48
1-13	A 2D contour of the multilayer impact of a typical bottom emission OLED at different wavelengths.	49
2-1	Bilayer corrugation sample structure and materials.	59
2-2	Morphology control by PBD thickness.	60
2-3	Morphology control by Alq ₃ thickness.	60
2-4	Morphology control by annealing temperature.	61
2-5	Corrugated OLED fabrication and structure.	61

2-6	The performance of the corrugated OLED (red) and the control planar OLED (black).	62
2-7	The electron dominant device JV performance with the device energy diagram included.	62
2-8	The operational stability performance of the corrugated OLED and the control planar OLED.....	63
3-1	A schematic showing the air cone and Bragg diffraction equation.....	77
3-2	The multilayer impact spectrum as a function of in-plane wavevector of a planar OLED. The three features in red are TMWG, TEWG and SPP from left to right, respectively.....	77
3-3	A schematic depicting the six-direction scattering associated with a hexagonal structure.....	77
3-4	A comparison between simulated and measured data. The left four figures show the simulated data and the right four figures show the measured data. The four set of data are from two detection angles ϕ and two polarization directions.	78
3-5	Dashed lines highlighting the features with the associated reception angles. Dashed lines in red show scattered TMWG and SPP modes, which are simulated. Dashed lines in yellow show scattered TEWG mode, which is not included in the simulation. The reason is explained previously.	79
3-6	Plots of scattering strength of TMWG and SPP modes as a function of reception angle and polarization.....	79
3-7	A schematic depicting Bragg diffraction equation with random scattering directions.	80
3-8	A comparison of far field emission pattern at 520 nm between ‘single-crystal’ structure and ‘poly-crystal’ structure.	80
3-9	The measured angle resolved spectra data with the baseline subtracted.	80
4-1	The out-coupling problem towards a certain emission angle of an in-cavity dipole is equivalent to the in-coupling problem of a far-field dipole from that direction into the cavity.	90
4-2	The refractive index contour of two grating structures.	90
4-3	The z component of the light field.....	91
4-4	The z component of the light field with the emitting layer highlighted in red.	91

4-5	Plots showing the integrated E_z over the EML as a function of incident angles for two structures	92
4-6	Plots showing the static electric field intensity distribution inside the cavity with two structures.	92
4-7	Plots showing the integrated E_z over the EML weighted by the static electric field as a function of incident angles for two structures.	92
4-8	The refractive index map of the two structures.	93
4-9	The z component of the light field with the emitting layer highlighted in red.	93
4-10	Plots showing the integrated E_z over the EML as a function of incident angles for two structures.	93
4-11	Plots showing the integrated E_z over the EML weighted by the static electric field as a function of incident angles for two structures.	94
5-1	The measurement setup of PL measurement during a constant-current degradation test. Inset: A plot showing an example data set measured from a green OLED showing the degradation of both EL and PL.	105
5-2	Emitter concentration effect of 4CzIPN OLEDs.	106
5-3	Measured and fitted EL and PL degradation of 4CzIPN devices with different emitter concentrations.	107
5-4	Dopant 1 OLED structure..	108
5-5	Measured and fitted EL and PL degradation of Dopant 1 devices with different emitter concentrations.	109
5-6	Drive voltages of OLED devices.	110
5-7	The effect of a mixed host on the OLED stability and emission zone length.	111
5-8	Simulated data with different effective emission zone lengths based on measured 10% emitter concentration single host Dopant 1 OLED data.....	112

LIST OF ABBREVIATIONS

4CzIPN	(4s,6s)-2,4,5,6-tetra(9H-carbazol-9-yl)isophthalonitrile
AFM	Atomic Force Microscope
Alq ₃	Tris(8-hydroxy-quinolinato)aluminum
CE	Current Efficiency
CIE	International Commission on Illumination
CT	Charge Transfer
Dopant 1	4-carbazolyl-2-methylisoindole-1,3-dione
EL	Electroluminescence or Electroluminescent
EML	Emitting Layer
EQE	External Quantum Efficiency
EBL	Electron Blocking Layer
EIL	Electron Injection Layer
ETL	Electron Transport Layer
HAT-CN	1,4,5,8,9,11-hexaazatriphenylene-hexacarbonitrile
HBL	Hole Blocking Layer
HIL	Hole Injection Layer
HTL	Hole Transport Layer
HOMO	Highest Occupied Molecular Orbital
IC	Internal Conversion
ISC	Intersystem Crossing
IQE	Internal Quantum Efficiency
Ir(ppy) ₃	Tris(2-phenylpyridine)iridium(III)
ITO	Indium Tin Oxide
LiF	Lithium Fluoride

Liq	8-Hydroxyquinolinolato-lithium
LUMO	Lowest Unoccupied Molecular Orbital
mCBP	3,3-di(9H-carbazol-9-yl)biphenyl
NPB	N,N'-bis(naphthalen-1-yl)-N,N'-bis(phenyl)-benzidine
OLED	Organic Light Emitting Diode
PEDOT:PSS	Poly(3,4-ethylenedioxythiophene):polystyrenesulfonate
PBD	2-(4-biphenylyl)-5-(4-tert-butylphenyl)-1,3,4-oxadiazole
PDMS	Polydimethylsiloxane
PL	Photoluminescence or Photoluminescent
T2T	2,4,6-tris(biphenyl-3-yl)-1,3,5-triazine
TADF	Thermally Activated Delayed Fluorescence
TAPC	di-[4-(N,N-ditolyl-amino)-phenyl]cyclohexane
TcTa	Tris(4-carbazoyl-9-ylphenyl)amine
TPBi	2,2',2''-(1,3,5-benzinetriyl)-tris(1-phenyl-1-H-benzimidazole)
TPD	N,N'-bis(3-methylphenyl)-N,N'-diphenylbenzidine

Abstract of Dissertation Presented to the Graduate School
of the University of Florida in Partial Fulfillment of the
Requirements for the Degree of Doctor of Philosophy

LIGHT EXTRACTION AND DEGRADATION MECHANISM STUDY OF ORGANIC
LIGHT EMITTING DIODES

By

Cheng Peng

December 2017

Chair: Franky So

Major: Materials Science and Engineering

The light extraction efficiency of common bottom emission OLEDs is limited to 25-30%. One of the commonly used approaches to exceed this limitation is to corrugate the interfaces. Herein, a simple process will be introduced to fabricate a corrugated OLED containing a corrugated bilayer ETL by thermal annealing due to the big difference between the glass transition temperatures between the two materials. We show that the morphology of the corrugated structure can be tuned by the annealing temperature and the layer thicknesses. The corrugated OLED with the corrugated bilayer ETL shows better efficiency and stability than the control planar OLED.

The scattering efficiency of waveguide and SPP mode by the corrugation remains challenging to quantify. Herein, we demonstrate a quantitative analysis on the scattering efficiency of the corrugation of waveguide mode and SPP mode. The calculation is based on optical simulation using Bragg diffraction equation and fitting with the measured data of corrugated OLEDs. We successfully quantified the extraction efficiency of waveguide mode and SPP mode using a hexagonal close-packed corrugation and a random corrugation.

The scattering strength of waveguide mode by corrugation remains an open topic. Herein, we applied the reciprocity theorem in finite difference time domain simulation and compared the scattering strength of TMWG from different corrugations. We studied the combined effect of optical diffraction and non-uniform electric field.

The control of emission zone is crucial to OLED stability. It is challenging to probe the emission zone. A new and simple methodology will be introduced to quantitatively probe the emission zone of OLEDs by comparing the PL degradation of OLEDs with the EL degradation during continuous electrical operation. This approach is first validated by investigating OLEDs using the well-known 4CzIPN. We then applied this approach to investigate the emitter concentration effect on the stability of OLEDs using Dopant 1. Based on our results, the Dopant 1 OLEDs show much less pronounced emitter concentration effect due to the relatively worse electron transport in the EML, compared with 4CzIPN OLEDs. We were able to widen the emission zone by the use of a mixed host.

CHAPTER 1

FUNDAMENTALS OF ORGANIC SEMICONDUCTORS AND ORGANIC LIGHT EMITTING DIODES

Molecular Orbitals

Organic semiconductors are organic small molecules, oligomers and polymers that are conductive in a solid film.¹ Organic molecules all have carbon atom chains, combined with other atoms such as H, N, O, S and halogen atoms. According to the molecular orbitals theory, when the electron clouds of adjacent atoms overlap, the intrinsic atomic electron energy levels split and form a lower energy bonding level and a higher energy antibonding level. Figure 1-1 shows a schematic of the molecular orbitals energy diagram of benzene. The overlapping of electrons with the spherical electron cloud forms σ -bond and anti-bond and the overlapping of p electrons with the spindle-configuration electron cloud forms π -bond and anti-bond. The s-bonds with a much higher bonding energy form the chains of the molecule while the electrons in the π -bonds can be shared with adjacent atoms forming an intra-molecular delocalized π electron system, which gives rise to the conductivity of such kind of organic molecules. In the solid state, adjacent organic molecules interact with each other mainly by van der Waals forces. Compared with the covalent bonds in inorganic semiconductors such as silicon and gallium nitride, van der Waals interaction is much weaker, which fails to form band structures. π electrons are not inter-molecular delocalized and there are no conduction band and valence band. Nevertheless, the electron energy levels of an organic semiconductor solid are a consequence of the interaction of molecular π electron systems of all the molecules. Highest-occupied-molecular-orbital (HOMO) and lowest-unoccupied-molecular-orbital (LUMO) are two terms with similar physical meanings to the valence band edge and the conduction band edge in terms of electron

energy levels. Due to the molecular interactions, the energy gap between the HOMO and LUMO of an organic semiconductor solid is smaller than the gap between the ground state and excited state of a single molecule, which can be observed in the photo-physics measurement comparing a dilute solution and a solid sample.

Organic Semiconductor Thin Films

Thanks to the intra-molecular π electron delocalization and the inter-molecular π - π coupling, organic semiconductor thin films can have a moderate vertical charge mobility on the order of 10^{-6} to $10^{-3} \text{ cm}^2/(\text{V}\cdot\text{s})^2$ even in an amorphous film, though still a lot lower than common inorganic semiconductors. This moderate charge mobility is sufficient to supply charges in a thin film vertical device with the thickness on the order of 100 nm, such as organic light emitting diodes. Since the inter-molecular van der Waals forces are weak compared with chemical bonds, the electrons are localized on single molecules. However, under electric fields, electrons can have inter-molecular transport through ‘hopping’ process, in which electrons hop from one molecular to another over the energy barrier between them. The barrier shape can be influenced by the electric field, giving rise to a field dependent charge mobility. Organic semiconductors can transport electrons and holes. Electron transport happens when excess electrons on the LUMO level hop through molecules under the electric field. Hole transport happens when electron vacancies on the HOMO level, which are referred to as holes, hop through molecules under the electric field. In general, organic semiconductor solids have a higher hole mobility than the electron mobility.

Photo-physics of Organic Molecules

Electrons in the conjugated π -systems dominate the photophysical properties.

When the organic solid is in its electronic ground state, all the electrons on the HOMO levels despite small fluctuation. Due to Pauli's exclusion principle, each molecular HOMO has two electrons with opposite spins. The total spin quantum number is zero, indicating the ground state is a singlet state with only one allowable secondary spin quantum number. When external energy is provided to the molecules, electrons can be excited to the excited states, the LUMO level, leaving behind a hole on the HOMO state. This generated pair of opposite charges can interact with each other by Coulombic forces. This interaction is particularly significant in organic solids due to a relatively lower dielectric constant compared with common inorganic semiconductors. The electron-hole pair bounded by Coulombic interaction forms a meta-stable quasi-particle, exciton. The interaction energy bounding this quasi-particle can be as high as 1 eV.³ Excitons are an important feature of organic solids, which distinguish organic semiconductor solids from the inorganic counterparts. When an electron is on the excited states, leaving behind another electron on the ground state, the spin states of the two electrons are not limited by Pauli's exclusion principle. The total spin quantum numbers can be zero and one. When the total spin quantum number is zero, the exciton is a singlet exciton as the ground state. When the total spin quantum number is one, the exciton is a triplet exciton as there are three allowed secondary spin quantum numbers minus one, zero and one. Based on quantum chemistry theories, the electrons in the triplet states generally have a lower energy than the electrons in the singlet states. The ground state and the excited states are not only containing one state. Electronic, vibrational, rotational and translational freedoms of the organic molecule broaden each

molecular level into manifolds. The Jablonski diagram as shown in Figure 1-2 illustrates the energy levels of organic molecules and the transitions between them. For spin-conserved quantum transitions such as electric dipole transitions, molecules can only undergo transitions from singlet states to singlet states or from triplet states to triplet states. For other transitions that do not require spin-conservation such as thermally activated transitions, molecules can undergo transitions between singlet states and triplet states. The transition from singlet state to triplet states is inter-system crossing (ISC) and the transition from triplet state to single state is reverse inter-system crossing (RISC). Under photo-excitation from the ground singlet state, as the absorption of a photon is an electric dipole transition, the conservation of total spin quantum number requires that the final state must be a singlet state, too. Depending on the photon energy, the final state of this electric dipole transition can be anywhere in the singlet state manifold. This electronic transition is almost instantaneous compared with the nuclear motion time so that the nuclear coordinates hardly change during the transition. Right after this transition, a rapid relaxation takes place and the electron relaxes to the lowest point of this manifold with changed nuclear coordinates. If a radiative decay follows, the nuclear coordinates remain unchanged during the electronic transition and the electron goes back to the ground state manifold, followed by another relaxation process. This entire process involving the photo-excitation and radiative transition is described by the Franck–Condon principle, which explains the widely observed Stokes shift from the absorption spectrum to the fluorescence spectrum. This photon-photon conversion described above is called photoluminescence. The radiative transition from the excited singlet state to the ground state generating photons is called fluorescence.

Fluorescence has a rate on the order of 10^9 s⁻¹. The term photoluminescence quantum yield (PLQY) is used to quantify the efficiency of photo-generated fluorescence, defined as the ratio of emitted photons to the absorbed photons. PLQY is directly related to the ratio between radiative decay rate and non-radiative decay rate. Researchers have already developed many organic molecules with PLQY close to 100%, which contributes to the success of OLEDs.

Excitons and Intermolecular Exciton Energy Transfer

Excitons are electron-hole pairs bounded by Coulombic interaction in a similar manner as a hydrogen atom. Excitons can fall into two main categories according to the radius, Frenkel excitons and Wannier-Mott excitons. Frenkel excitons have a stronger interaction energy and a small radius localized on a single molecule. Excitons in organic solids usually are Frenkel excitons due to the lower dielectric constants and the stronger Coulombic interaction. Wannier-Mott excitons are weakly bounded excitons with a much larger radius delocalized on several adjacent molecules. Excitons in inorganic semiconductor solids usually are Wannier-Mott excitons due to the higher dielectric constants and thus a stronger electric screening. The weak Coulombic interaction makes the excitons only exist at low temperatures.

There are another special kind of excitons, charge transfer (CT) excitons, which lies between the two kinds of excitons described above in terms of the radius. A CT exciton is also referred to as an exciplex. It is an exciton formed by a pair of electron and hole on two molecules next to each other. The interaction energy of a CT exciton is weaker than a Frenkel exciton. It plays an important role in the charge separation process in polymer solar cells and is also utilized recently as the host species in high-efficiency OLED emitting layers.

As an electron-hole pair, excitons do not have a net charge. Excitons can diffuse in the organic solids without net charge transport. The transport of excitons has been extensively studied and is categorized into three kinds. The first kind is through a radiative mechanism. Exciton can transfer from one molecule to another molecule by emission and absorption of a photon. This transfer does not require any interaction between the donor molecule and the acceptor molecule. The transfer rate apparently depends on the radiative rate of the donor molecule and the absorbing ability of the acceptor molecule as well as the overlap of the emission spectrum of the donor molecule and the absorption spectrum of the acceptor spectrum. The second kind is Förster resonance energy transfer (FRET). FRET is a non-radiative mechanism. The energy is transferred through a dipole-dipole Coulombic-like interaction. Analogous to the interaction between two electric dipoles, this interaction is long-range with the FRET rate inversely proportional to R^6 , with R representing the distance between the donor and the acceptor molecules. The FRET rate also depends on the relative orientation of the two molecules similar to the interaction between electric dipoles and the overlap of the emission spectrum of the donor molecule and the absorption spectrum of the acceptor spectrum as if there are an emission and absorption process of a virtual photon. The typical interaction length can be as much as 10 nm. FRET requires the conservation of spin, so the fast energy transfer of singlet excitons usually occurs through FRET. Note that the previous two kinds of exciton transfers do not involve the real electron transfer from one molecule to another. The third kind of energy transfer is Dexter transfer through charge exchange. The electron and the hole on the donor molecule are transferred to the acceptor molecule's LUMO and HOMO, respectively.

Dexter transfer is short-range and the transfer rate decreases exponentially as the distance between the two molecules increases. Dexter transfer is also independent on the transition dipole moments of the emission and the absorption processes. As the charge exchange process requires the overlap of electron cloud from the donor and acceptor molecules, the interaction length is only within 1 nm. Dexter transfer only requires the spin conservation of the entire donor and acceptor system, so energy can be transferred between triplet states as well as between singlet and triplet states.

The transfer of excitation energy enables the interaction between excitons with excitons or other species such as charges. Given that the electric dipole transition from the triplet excited state to the singlet ground state is spin-forbidden, the triplet excitons are usually much longer lived than the singlet excitons, resulting in a longer diffusion length and thus a higher possibility of interaction with other species. Therefore, triplet-triplet interaction and triplet-polaron interaction are widely studied phenomena. Polarons are basically charges relaxed on molecules. Polarons are important for organic molecules due to the interaction between the charges and the molecular vibrations and rotations, giving rise to a non-trivial localization energy. Triplet-triplet interaction can lead to the annihilation of triplets, which are blamed for the loss of efficiency of OLEDs under high injection conditions. In this situation, it is referred to as triplet-triplet annihilation (TTA). Triplet-triplet interaction can lead to a higher-energy excited molecule, which is blamed for the operational degradation of OLEDs. Triplet-polaron interaction, which is often referred to as triplet-polaron quenching (TPQ), can also lead to the loss of excitons as well as lead to higher-energy excited molecules, thus usually playing a negative role in the OLED performance.

Charge Transport

As briefly introduced in the last section, polarons are an important charged species in organic solids. When charges exist in the organic solids, due to relatively weak electric screening in the organic solids, the charge polarizes the environment molecules. The charge together with the polarized environment is treated as a quasi-particle, polaron. Under electric fields, polarons transport in amorphous organic solids by hopping. Though band-like transport behavior of polarons is observed in crystalline organic solids with a high mobility, in amorphous organic solids, the hopping process is different than a band-like transport and is thermally activated. The mobility has an Arrhenius type dependence on the temperature.

$$\mu = \mu_0 \exp\left(-\frac{E_A}{k_B T}\right) \quad (1-1)$$

Where μ_0 is the intrinsic mobility at $T \rightarrow \infty$ and E_A is the activation energy, which can be viewed as the energy barrier to move one electron from one molecule to another. The energy barrier is also influenced by the polarization of the environment, which causes the localization of charges. The energy barrier between molecules can be lowered by the electric field, giving rise to the field dependence of mobility, known as the Frenkel-Poole effect.

$$\mu \propto \exp\left(-\frac{q(\varphi_B - \sqrt{\frac{qE}{\pi\varepsilon}})}{k_B T}\right) \quad (1-2)$$

Where q is the charge of the polaron, φ_B is the energy barrier at zero electric field, E is the electric field, and ε is the dielectric constant. $\sqrt{\frac{qE}{\pi\varepsilon}}$ quantifies the lowered amount of the energy barrier by the electric field.

Fundamentals of OLEDs

Organic light emitting diodes (OLEDs) are vertical thin film devices converting electricity to light using the electroluminescence of organic molecules.

Organic active layers are sandwiched between two electrodes. At least one of the two electrodes is semi-transparent or transparent, through which generated light leaves the device. In a typical OLED structure, there are several different organic functional layers, which are hole injection layer (HIL), hole transport layer (HTL), electron blocking layer (EBL), emitting layer (EML), hole blocking layer (HBL), electron transport layer (ETL) and electron injection layer (EIL) consecutively from the anode to the cathode. A schematic of the typical structure OLED is shown in Figure 1-3. When an external voltage is applied to the two electrodes, electrons and holes are injected from the two opposite electrodes. Electrons and holes then transport under the electric field towards the other electrode. After electrons and holes meet on the organic molecules, they form pairs bounded by the Coulombic interaction. The OLED structure is often designed in such a way that excitons are generated in the EML, where light with a specific spectrum can be generated. A schematic of the OLED working mechanism is shown in Figure 1-4. These electron-hole pairs are electrically generated excitons. Unlike photo-generated excitons, electrically generated excitons are not the result of spin-conserved absorption process. Both singlet excitons and triplet excitons can be generated with the population ratio of 1:3 according to the spin statistics. In conventional organic semiconductor materials, only singlet excitons can undergo spin-conserved radiative fluorescence process generating photons. The photon energy is determined by the exciton energy of the emitting molecule. The generated photons then escape the device with a light extraction efficiency. Limited by the 1:3 generation ratio

between singlet excitons and triplet excitons, the internal quantum efficiency (IQE) of this type of fluorescent OLEDs cannot exceed 25%. IQE quantifies the amount ratio between generated photons in the active layer and the injected carriers. Other than the 25% limitation due to spin statistics, IQE is primarily determined by the recombination efficiency of injected carriers and the quantum yield of the emitting molecule. The former one is determined by the device charge balance. When the charges are imbalanced, there will be electrons or holes leaking out of the EML without recombination. The quantum yield of the emitting molecule is determined by the molecule itself related to the PLQY as well as the interaction between the emitting molecule with other species in the EML. As mentioned previously, TTA and TPQ can lower the quantum yield of the emitting molecule.

The 25% IQE limit can be exceeded by introducing other mechanisms. Phosphorescent materials⁴ and thermally activated delayed fluorescent (TADF) materials⁵ have been developed to harvest the originally non-radiative triplet excitons. In phosphorescent materials, which are often organometallic complexes, mixing of triplet states and singlet states due to spin-orbital coupling is taken advantage of by introducing heavy metal atoms. The mixing enhances the ISC from the singlet state to the triplet state and enables the radiative transition from the triplet state to the ground state. This radiative transition is much slower than fluorescence with a rate on the order of $1\text{e}6 \text{ s}^{-1}$ and referred to as phosphorescence. By harvesting triplet excitons, phosphorescent materials improve OLED IQE to near 100%. TADF materials harvest triplet excitons in a different way. TADF materials are designed in such a way that the LUMO orbital and the HOMO orbital are separate in space, which leads to a small

triplet-singlet energy difference $\Delta E_{ST} < 0.1$ eV. Even at room temperature, the thermal energy is sufficient to activate a significant RISC rate, which enables the harvest of triplet excitons. Since the RISC is still much slower than the common fluorescence, a signature of TADF materials is a delayed component in the transient PL. Schematics depicting the mechanisms of phosphorescence and TADF are shown in Figure 1-5.

Even the IQE of OLEDs can be improved to near 100% by using phosphorescent and TADF materials, not all the generated photons can leave the device, with the light extraction efficiency less than unity. The light extraction efficiency is defined as the ratio of the number of photons leaving the device to the number of photons generated in the EML. In a common bottom emission OLED with glass as the substrate and ITO as the bottom electrode, the light extraction efficiency is about 25%~30%, implying that most of the generated photons are trapped in the device.

Electronics of OLEDs

When a voltage bias is applied across the OLED device, electrons are injected from the cathode and holes are injected from the anode. The injection efficiency is determined by the energy barrier at the interfaces. The difference between the Fermi level of the cathode and LUMO of the organic material in contact determines the electron injection barrier. The difference between the Fermi level of the anode and HOMO of the organic material in contact determines the hole injection barrier. ITO is the common anode material from a bottom emission OLED with a work function of 4.4-4.5 eV.^{6, 7} This work function results in an energy barrier of about 1 eV with commonly used HTL materials. One usual way is to increase the work function of ITO by surface treatment such as UV ozone.⁸ Another usual way is to add a HIL to facilitate the hole injection.⁹ Commonly used HIL materials include transition metal oxides such as

Molybdenum oxide.¹⁰ On the opposite side, metals with lower work functions are good candidates for the cathode. Magnesium-silver alloy with a 9:1 volume ratio is used as the cathode material, given the low function of magnesium about 3.6 eV.¹¹ Aluminum is widely used as the cathode materials with a thin EIL of lithium fluoride.¹² Though the work function of aluminum around 4.1 eV is more than 1 eV higher than the LUMO of commonly used ETL organic materials, the use of a 1 nm thick LiF layer as the EIL significantly enhances the electron injection. A possible explanation is that under the bombarding of evaporated aluminum, LiF decomposes and diffuses into the ETL acting as an n type dopant.¹³ The n doping of ETL forms the near Ohmic contact between the ETL and the cathode. Direct doping of HTL and ETL is another way to enhance injection as well as transport.¹⁴

Under the electric field, the injected electrons and holes transport towards the opposite electrodes. ETL and HTL materials are designed in such a way that they have efficient charge injections from the electrodes and reasonable charge transport mobilities. Sandwiched between the ETL and HTL is the EML. Holes and electrons are injected into the EML and they form excitons. For high-efficiency OLEDs, EMLs are composed of a matrix material called the host and the emitter to avoid the emitter bimolecular interactions such as TTA. The LUMO and HOMO level alignments between adjacent materials are very important to make sure that no significant energy barriers are present that impede the carrier injection in the relevant direction. To achieve a high IQE, it requires all the carriers recombine in the EML. To achieve this goal, EBL and HBL are added on the two sides of the EML to create high barriers to prevent carriers from leaving the EML.¹⁵

Terminology of Photometry

In radiometry, light is measured by the absolute power distribution of radiation in space using the unit such as watt and joule, while in photometry, light is measured by the weighted power according to the sensitivity of the human eye. Photometry is widely used in the device performance characterization in the area of display and lighting. As the human eye can only perceive the visible light and is most sensitive to the green light, a wavelength dependent photopic luminosity function is used to model the human eye responsivity, when the radiant intensity in W/sr is converted to the luminous intensity in lm/sr (cd). The photopic luminosity function is the CIE standard curve used in the CIE 1931 color space and is plotted in Figure 1-6.

Taking the human eye sensitivity into consideration, photometry has a series of physical quantities to characterize light. Luminous flux in the unit of lm measures the luminous energy per unit time. Luminous intensity in the unit of cd measures the luminous flux per unit solid angle. Luminance in the unit of cd/m² measures the luminous intensity per unit projected source area. The luminous flux in lm can be calculated from the spectral radiant flux in W/nm using the equation

$$\Phi_V = 683.002 \text{ lm/W} \cdot \int V(\lambda) \Phi_{e,\lambda} d\lambda \quad (1-3)$$

Where Φ_V is the luminous flux in lm, $V(\lambda)$ is the normalized dimensionless photopic luminosity function, $\Phi_{e,\lambda}$ is the spectral radiant flux in W/nm and λ is the wavelength in nm.

These physical quantities in photometry are used to characterize the performance of OLED. As OLED is an area light source, luminance is used to measure the brightness of OLED. The current efficiency (CE) is defined as the luminance at unit input current. The unit of CE is cd/A. Luminous efficacy, also called power efficiency, is

used to measure the luminous flux at unit input power. The unit is lm/W. These two efficiencies are both influenced by the emission spectrum of the OLED.

The emission spectrum of the OLEDs is characterized by a set of CIE color coordinates (X, Y, Z) in the CIE 1931 color space. The three values are calculated by the equations below,

$$X = \int L_{e,\Omega,\lambda}(\lambda) \bar{x}(\lambda) d\lambda \quad (1-4)$$

$$Y = \int L_{e,\Omega,\lambda}(\lambda) \bar{y}(\lambda) d\lambda \quad (1-5)$$

$$Z = \int L_{e,\Omega,\lambda}(\lambda) \bar{z}(\lambda) d\lambda \quad (1-6)$$

Where $L_{e,\Omega,\lambda}(\lambda)$ is the spectral radiance in W/(sr·nm). The three weighting functions are the CIE standard observer color match functions as plotted in Figure 1-7.

Oftentimes, the coordinates are normalized and a set of x, y, Y parameters are designed so that Y equals the luminance and x, y are calculated as,

$$x = \frac{X}{X+Y+Z} \quad (1-7)$$

$$y = \frac{Y}{X+Y+Z} \quad (1-8)$$

The two parameters x and y can specify a color as shown in the CIE 1931 color space chromaticity diagram in Figure 1-8.

Optics of OLEDs

As defined previously, the light extraction efficiency measures the percentage of photons leaving the device relative to the generated photons. This light extraction efficiency is determined by the optical properties of OLEDs. Before the optical properties of OLEDs are discussed, the two common OLED configurations should be mentioned first. According to whether the light is coming out through the substrate or not, OLEDs can be categorized into two classes, bottom emission OLEDs and top emission OLEDs, as shown in the schematics in Figure 1-9.

In the bottom emission OLEDs, the indium tin oxide (ITO) thin film is deposited on the glass substrate as the bottom transparent electrode. The top electrode is opaque, reflective and metallic. In the visible range, the refractive index of glass is about 1.5, the refractive index of ITO is about 2.0¹⁶ and the refractive index of common organic semiconductor materials in the active layers is about 1.7-1.8.^{17, 18} Given the refractive index of air is 1.0, which is much lower than the materials in the device including the glass substrate, the generated light in the active layers has several loss channels before leaving the device into the air. This will be discussed in detail in the next paragraphs.

The optics of the OLEDs primarily include two parts: the optical cavity and the interaction between the optical cavity and the excitons. The high-index ITO and organic layers together with the reflective metallic mirror form an optical cavity. The thickness of ITO is 70-100 nm and the thickness of the organic layer is 100-150 nm or can be much thicker to form higher-order resonant cavities. The discussion here is only restricted to the first-order resonant cavity with the lowest thickness, but most conclusions and concepts also perfectly apply to thicker cavities. This optical cavity contains many photonic modes, among which the most important are surface plasmon polariton (SPP) mode and the waveguided (WG) mode. The SPP mode of OLEDs exists at the interface between the organic dielectric layer and the metal.¹⁹ It is transverse magnetic (TM) and the electric field associated with the SPP mode is concentrated at the organic-metal interface, decaying exponentially away from the interface. The out-of-plane component is dominating the electric field. WG modes of OLEDs usually contain two modes,²⁰ one is transverse electric (TE) and the other is TM. A thicker optical cavity can have more

WG modes. At the wavelength in air of 520 nm, the electric field associated with the TEWG mode has the maximum in the high-index ITO layer and extends into the organic layer. For the electric field associated with the TMWG mode, the in-plane and out-of-plane components have different distributions over the thickness of the optical cavity. The in-plane component has its maximum near the middle of the organic layer while the out-of-plane component has its maximum at the interface between the organic layer and the metal, similar to the SPP mode. The WG mode and the SPP mode don't couple with the far-field traveling electromagnetic wave in the glass substrate or in the air because of the in-plane wavevector mismatch. When light travels across an interface, the boundary conditions according to the Maxwell's equations require the continuity of the wavevector component parallel to the interface. The in-plane wavevectors associated with the WG mode and the SPP mode are even larger than the total wavevector in glass and in air, while the far-field traveling wave needs to have a real out-of-plane wavevector, which leaves the in-plane component smaller than the total wavevector. Therefore, the WG mode and the SPP mode cannot couple with the far-field traveling wave outside the optical cavity.

The interaction between the exciton and the optical cavity can not only influence the light extraction efficiency, but also the quantum yield of the exciton. According to the Fermi golden rule, the radiative transition rate of the exciton is proportional to the local photonic density of states, which is proportional to the intensity of electric field associated to an optical mode in classic physics. This environmental effect on radiative transition rate is called Purcell effect. The magnitude of the enhancement is called

Purcell factor.¹⁹ All the modes with a non-zero density can contribute to the Purcell effect, including the WG mode and the SPP mode.

Purcell effect does not necessarily enhance the efficiency of the OLED. On the one hand, Purcell effect only enhances the radiative transition rate of the excitons, which does not lead to a significant enhancement in quantum yield for an already efficient molecule. On the other hand, photons generated by radiative transitions can be coupled to the WG mode and the SPP mode, while these modes cannot couple with the travelling wave outside the optical cavity, not contributing to the efficiency of the OLED, which are important energy loss channels of OLEDs. The energy coupled to the WG mode and the SPP mode eventually dissipate in the optical cavity.

Other than the photons coupled in the WG mode and the SPP mode, there are still a significant number of photons that can couple to the far field in the glass substrate and the air. However, due to the larger refractive index of glass than that of the air, about half of the light is trapped in the glass substrate as a result of the total internal reflection (TIR) at the glass-air interface.²¹

The optical distance between the radiative exciton in the EML has a significant effect on the radiation in the far field. The reflected radiation can interfere with the as-generated radiation and influence the local mode density. This effect can be treated by introducing an image radiating molecule on the opposite of the metallic mirror and evaluating the effect on the original radiating molecule. Similar to other phenomena based on interference, the Purcell factor due to this effect oscillates as the optical distance between the EML and metallic electrode increases.

All the factors interplay with each other and determines the light extraction efficiency of OLEDs. In a common bottom emission OLED, 30%-35% of the generated energy is lost in the SPP mode. 15%-20% is lost in the WG mode. 25%-30% is trapped in the glass substrate (called the substrate mode). Only 25%-30% can couple into the air (called the air mode), contributing to the OLED efficiency. The external quantum efficiency (EQE) is defined as the number of photons in the air mode divided by the number of electrons injected into the OLED.

$$EQE = IQE \times \text{light extraction efficiency} \quad (1-9)$$

Even though the IQE can be improved to near 100% by technologies such as TADF and phosphorescence, the EQE is limited to about 25%-30% by the light extraction efficiency.^{17, 22-24} A schematic showing all the main power dissipation channels is in Figure 1-10.

Even though not mentioned above, all these optical factors are wavelength dependent. Both the WG and the SPP modes are dispersive. The effect from the image radiating molecule based on interference is wavelength dependent. As the result, when the optical distance from the metallic mirror changes continuously, the Purcell factor from different wavelengths peaks at different distances. These dispersive optical factors can significantly influence the emission spectrum of OLEDs. In Figure 1-11, the energy distribution among different channels and the emission spectra are plotted as a function of ETL thickness, which is essentially the distance between the EML and the metallic mirror. These are simulation results, but are experimentally confirmed and widely accepted.

In a common top emission OLED, the optics are very different from the case of bottom emission OLEDs. The main difference is a semi-transparent top electrode

instead of a transparent ITO electrode. Due to fabrication limitation, ITO is not used as the top electrode for top emission OLEDs. Thin metal electrodes are widely used, instead. A compromise between transmittance and conductance is a key issue. Compared with the 90% transmittance ITO, the metallic top electrode has a much higher reflectance. The reflective bottom metallic electrode and the semi-transparent top electrode form an optical microcavity.²⁵ The situation becomes more complicated as the light reflected from the top electrode interfere with the light reflected from the bottom electrode. The interference is similar to the situation in a Fabry–Pérot resonator. When the optical thickness of the microcavity matches the resonance condition to form a standing wave, the Purcell effect enhances significantly the emission in the forward direction for that specific wavelength. This relatively strong microcavity effect influences the angle-dependent emission spectrum and the intensity, which is a distinct feature of top emission OLEDs.

Optical Simulation of OLEDs by Setfos

Optical simulation has been used to quantitatively analyze the optics of OLEDs. As mentioned previously, the WG mode and the SPP mode cannot couple to the air mode, so the light trapped in those two modes is not detectable without disturbing the flat interfaces. Optical simulation has the capability to help understand them.

Setfos is the software package for OLED optics simulation developed by Fluxim. All the optical simulation of planar OLED structures shown in this thesis are done with Setfos. In this section, the theories and the simulation method will be described.²⁶ In the optical simulation of OLEDs, there are some basic assumptions. Radiating excitons are treated as point driven damped harmonic dipole oscillators. All the layers have perfectly flat interfaces and infinitely extended in the substrate plane. The EML is not absorbing.

All the materials are non-magnetic. Under the electric field generated by the dipole and reflected by the interfaces, the dynamics of the dipole moment \vec{p} is described by the equation below,

$$\frac{d^2}{dt^2} \vec{p} + b_0 \frac{d\vec{p}}{dt} + \omega^2 \vec{p} = \frac{e^2}{m} \vec{E}(\omega) \quad (1-10)$$

Where b_0 is the intrinsic damping constant, ω is the angular frequency of the electric field, e is the elementary charge, m is the effective mass, \vec{E} is the electric field at the position of the dipole moment. The intrinsic damping constant is proportional to the dissipating power of the dipole in the same medium with an infinite thickness and thus no interfaces. Based on the classical theory of radiating dipole, we have

$$q_0 b_0 = \frac{p^2 \omega k_0^3}{12\pi \epsilon_0} n \quad (1-11)$$

Where k_0 is the total wavevector in vacuum and $k_0 = 2\pi/\lambda_0$. n is the refractive index of the medium, which is about 1.7-1.8 for common organic semiconductor materials in OLEDs. q_0 is the radiation efficiency of this dipole. We have the trivial equation below,

$$b_0 = q_0 b_0 + (1 - q_0) b_0 \quad (1-12)$$

Where the first term is the power of radiation and the second term is the non-radiative loss.

In an optical cavity with interfaces, the total dissipating power b will be

$$b = qb + (1 - q)b \quad (1-13)$$

Where q is the radiation efficiency in the optical cavity. Assuming that the optical cavity only has effect on the radiation known as the Purcell effect, we have

$$b = q_0 b_0 \cdot F + (1 - q_0) b_0 \quad (1-14)$$

Where F is the Purcell factor. Therefore, we have

$$q = \frac{q_0 b_0 \cdot F}{b} = \frac{q_0 F}{q_0 F + (1 - q_0)} \quad (1-15)$$

This equation also indicates that for an efficient emitter with $q_0 \sim 1$, we have $q \sim 1$.

The Purcell effect has little effect on the intrinsic efficiency, though it does enhance the radiative transition rate, which shortens the exciton lifetime.

It is expected and understood that the Purcell effect of OLEDs is also wavelength dependent and wavevector dependent, i.e. the optical cavity affects the intrinsic emission of the molecule with different amount of enhancement at different wavelengths and different wavevectors. This enhancement ratio is calculated as the Multilayer Impact in Setfos simulation. It is independent on the intrinsic spectrum of the molecule as it calculates the relative ratio. Therefore, Multilayer Impact reflects the properties of the optical cavity.

The equation calculates the intrinsic dipole radiation power is derived from the classical dipole radiation theory. The electric field generated by an oscillating dipole in vacuum is given by the equation below.

$$\vec{E} = \frac{1}{4\pi\epsilon_0} \left\{ k^2 (\vec{n} \times \vec{p}) \times \vec{n} \frac{e^{ikr}}{r} + [3\vec{n}(\vec{n} \cdot \vec{p}) - \vec{p}] \left(\frac{1}{r^3} - \frac{ik}{r^2} \right) e^{ikr} \right\} \quad (1-16)$$

The first term in the parenthesis is the far-field part and the second term is the near-field part. As the reflection and refraction at the interface are angle-dependent as shown by the Fresnel's equations, it is beneficial to expand the radiation electric field into plane waves with TM and TE polarizations. Then the reflected waves can be easily calculated using Fresnel's reflection equations.

$$r_{1,2}^{TM} = \frac{n_2^2 k_{z,1} - n_1^2 k_{z,2}}{n_2^2 k_{z,1} + n_1^2 k_{z,2}} \quad (1-17)$$

$$r_{1,2}^{TE} = \frac{k_{z,1} - k_{z,2}}{k_{z,1} + k_{z,2}} \quad (1-18)$$

Where 1 and 2 denote the two media and z denotes the out-of-plane component of the wavevector. The reflected wave and the emitted wave are then added coherently to calculate the local electric field at the location of the radiating dipole. The total radiated power can be given by,

$$L = \frac{\omega}{2} \vec{p} \cdot \text{Im} \vec{E}_{local} \quad (1-19)$$

In this equation, L is the radiated power, $\text{Im} \vec{E}_{local}$ denotes the imaginary part of the electric field at the dipole location. As usual in physics, the product of the dipole and the out-of-phase electric field it generates gives the dissipated power. As the OLED system is optically axially symmetric, the total radiated power can be decomposed to TM and TE polarized parts as a function of the in-plane wavevector. The Purcell factor at one single wavelength can then be expressed as

$$f = \int_0^{+\infty} (K^{TM}(\kappa) + K^{TE}(\kappa)) d\kappa^2 \quad (1-20)$$

Where κ is the in-plane wavevector.

Since the radiating molecule is treated as a radiating dipole moment, the orientation of the radiation dipole moment is crucial in determining the light extraction property of the optical cavity. Based on the dipole radiation equation, the magnitude of the Poynting vector is angular dependent, giving rise to a radiation profile as shown below. In general, most of the radiation power propagates in the direction perpendicular to the dipole moment. This results in very different behaviors between a vertical dipole and a horizontal dipole in the OLED optical cavity. Horizontal dipoles radiate more power with small in-plane wavevectors while vertical dipoles radiate more power with large in-plane wavevectors. As in general, modes with large in-plane wavevectors such

as the WG mode and the SPP mode do not couple with the air mode, horizontal dipoles have a higher light extraction efficiency than vertical dipoles do.

$K^{TM}(\kappa)$ and $K^{TE}(\kappa)$ are plotted in Setfos as Multilayer Impact as mentioned previously. Below in Figure 1-12 shows an example. The two functions at different wavelengths can be plotted together as a two-dimensional contour as also shown in Figure 1-13.

In this type of simulation, all the previously mentioned optical mode and effect such as the WG mode and the SPP mode are naturally included. For example, the SPP mode is a natural result when there is an interface between the dielectric and the metal. The significant imaginary refractive index of the metal gives rise to the SPP mode. The WG mode comes from the optical confinement when the refractive index of the radiating medium is higher than the bounding medium (glass).

By decomposing the integrand into different modes, Setfos can evaluate the power dissipated into different modes. In practice, this is done by setting the integration limits in a common bottom emission OLED. Given $u = \kappa/k_{organic}$ is the in-plane wavevector normalized to the total wavevector in the emissive medium, the power is dissipated in the air mode if $u \propto [0, \frac{n_{glass}}{n_{organic}})$, in the WG mode if $u \propto [\frac{n_{glass}}{n_{organic}}, 1)$ and in the evanescent mode (mostly SPP mode) if $u \propto [1, \infty)$. With this set of integration limits, the power dissipated into each mode can be calculated for all the wavelengths. Therefore, the percentage of power into each mode can also be calculated based on the intrinsic spectrum of the radiating molecule. The percentage into the air mode is the light extraction efficiency in terms of power. Then the quantum efficiency can be calculated. The total radiated power is related to the damping rate of the dipole moment,

which is inversely proportional to the exciton lifetime. There are differences in physics between the simulation and the reality in the device. As described above, the total radiating power is the result of adding power into all the modes, while the total radiating power in a real device is limited by the input power and the power conversion efficiency of the system and divided into different modes.

Note that in the simulation, the dipole model is used to deal with the radiation profile of the emitting molecule. The dipole moment \vec{p} is related more to the transition dipole moment of the molecule instead of the permanent dipole moment of the excited molecule. Though the excited molecule is described by the exciton, which is essentially a hole-electron pair, this hole-electron pair with spatial charge separation cannot be simply related to the dipole moment in the optical simulation.

Based on Fresnel equations, Setfos is designed to efficiently solve problems with flat interfaces. When it comes to corrugated interfaces, in which there are optical nanostructures with wavelength-size features widths, other simulation tools are needed.

Optical Simulation of OLEDs by FDTD

Finite-difference time-domain (FDTD) methods are another widely used simulation tool to model optical processes on OLEDs.^{27, 28} FDTD methods are grid-based differential numerical modeling methods that solve Maxwell equations in the time domain. In the computation zone, the space is divided into small sub-spaces with well-defined optical constants in each sub-space. Then the electric field \vec{E} and the magnetic field \vec{H} in each sub-space are calculated as time proceeds by finite steps. As the simulation is done in the time domain, it can deal with multiple frequencies in a single simulation. An advantage of FDTD over Setfos is that in FDTD arbitrary materials with

arbitrary interfacial optical nanostructures can be incorporated in the simulation. The cost is a long simulation time, depending on the density of the grids. In the FDTD simulation, the two time dependent Maxwell's equations are solved,

$$\text{Faraday's law of induction: } \nabla \times \vec{E} = -\frac{\partial \vec{B}}{\partial t} \quad (1-21)$$

$$\text{Ampère's circuital law: } \nabla \times \vec{H} = \vec{J} + \frac{\partial \vec{D}}{\partial t} \quad (1-22)$$

Where $\vec{E}(\vec{r}, t)$ is the electric field, $\vec{D}(\vec{r}, t) = \epsilon \vec{E}$, $\vec{J} = \sigma \vec{E}$, $\vec{H}(\vec{r}, t)$ is the magnetic field, $\vec{B}(\vec{r}, t) = \mu \vec{H}$. ϵ , σ and μ are material properties and are dependent on frequency ω . The finite difference method is used to numerically solve the differential equations.

$$\frac{df}{dx} = \lim_{\Delta x \rightarrow 0} \frac{\Delta f}{\Delta x} = \frac{f(x+h) - f(x-h)}{2h} + o(h^2) \quad (1-23)$$

A central difference is chosen because the residual is proportional to the square term as shown in the equation, which makes it a better approximation. Dividing the space and time into small sub-spaces and applying the central difference equation to a physical quantity as a function of position and time, we have

$$\frac{\partial F^n(i,j,k)}{\partial x} = \frac{F^n(i+\frac{1}{2},j,k) - F^n(i-\frac{1}{2},j,k)}{\Delta x} + O((\Delta x)^2) \quad (1-24)$$

$$\frac{\partial F^n(i,j,k)}{\partial t} = \frac{F^{n+\frac{1}{2}}(i,j,k) - F^{n-\frac{1}{2}}(i,j,k)}{\Delta t} + O((\Delta t)^2) \quad (1-25)$$

Where $F^n(i,j,k)$ denotes the physical quantity $F(x,y,z)$ at the position $(i\Delta x, j\Delta y, k\Delta z)$ and at the time $n\Delta t$. The delta quantities are the steps in space and time. Note that the finite difference is determined by the values half-step away both in space and in time and that the electric field is determined by the derivative of the magnetic field and vice versa. A special arrangement of grid and value assignment was invented called Yee lattice.²⁹ In the arrangement of Yee lattice, the electric field and the magnetic field are calculated in time and space both with a half-step difference.

Then the time dependent Maxwell's equations can be written into six equations

with finite difference. Below shows one of the six equations to calculate $E_x^{n+1}(i + \frac{1}{2}, j, k)$,

$$E_x^{n+1}\left(i + \frac{1}{2}, j, k\right) = \\ \frac{1 - \frac{\sigma(i + \frac{1}{2}, j, k)\Delta t}{2\varepsilon(i + \frac{1}{2}, j, k)}}{1 + \frac{\sigma(i + \frac{1}{2}, j, k)\Delta t}{2\varepsilon(i + \frac{1}{2}, j, k)}} \cdot E_x^n\left(i + \frac{1}{2}, j, k\right) + \frac{\Delta t}{\varepsilon(i + \frac{1}{2}, j, k)} \cdot \frac{1}{1 + \frac{\sigma(i + \frac{1}{2}, j, k)\Delta t}{2\varepsilon(i + \frac{1}{2}, j, k)}} \cdot \left[\frac{H_z^{n+\frac{1}{2}}(i + \frac{1}{2}, j + \frac{1}{2}, k) - H_z^{n+\frac{1}{2}}(i + \frac{1}{2}, j - \frac{1}{2}, k)}{\Delta y} + \frac{H_y^{n+\frac{1}{2}}(i + \frac{1}{2}, j, k - \frac{1}{2}) - H_y^{n+\frac{1}{2}}(i + \frac{1}{2}, j, k + \frac{1}{2})}{\Delta z} \right] \quad (1-26)$$

The electric field and the magnetic field are calculated in time alternatively in a 'leap frog' manner.

There are restrictions on the spatial steps and time steps to avoid producing unstable results as shown below.

$$\Delta t \leq \frac{\sqrt{\mu\varepsilon}}{\sqrt{\frac{1}{(\Delta x)^2} + \frac{1}{(\Delta y)^2} + \frac{1}{(\Delta z)^2}}} \quad (1-27)$$

Though the rigorous analysis of the restrictions will not be discussed here, it is logical that the time step has an upper limit since the propagation of energy is slower than the speed of light.

With the basic algorithm, optical problems can be solved with FDTD by translating the real-world problem into a set of simulation conditions.

Boundary conditions play a key role in the FDTD simulation. As the simulation calculates the fields in each cell within the simulation region, the larger the region is, the longer the simulation takes. It also requires a significant amount of computing resources. It is beneficial to shrink the simulation region. An effective way to realize this is design an 'absorbing' boundary that absorbs all the radiation reaching it without any

reflection as if the radiation went to infinitely far without any disturbance from any boundaries. To simulate systems with symmetry or periodicity, a periodic boundary condition can be used to reduce the size of the simulation region.

Fabrication of OLEDs

The organic thin films and OLEDs are fabricated in a lab condition either by thermal evaporation in a vacuum chamber or by spin-coating from solution in a glovebox with nitrogen atmosphere or in ambient conditions.

Indium tin oxide (ITO) is the commonly used material for bottom transparent electrodes in OLEDs. Glass substrates with pre-deposited ITO are often purchased from vendors. ITO films can also be grown by vacuum sputtering. Glass substrates with ITO films are cleaned subsequently in acetone and 2-propanol each for 15 min in an ultra-sonic bath.³⁰ UV ozone surface treatment is then used to increase the work function of ITO to facilitate hole injection and to make the surface hydrophilic.

PEDOT:PSS Clevios™ Al4083 is spun-coated on the substrate from a 25°C, PVDF 45 µm filtered solution at 4000 rpm for 40 s followed by annealing at 160 °C for 30 min in ambient to passivate to surface particles and thus to suppress the leakage current. This step is particularly important in the lifetime study of OLEDs to improve the device fabrication yield. After the annealing, the substrates are transferred to the vacuum chamber. All the organic semiconductor small molecule materials are thermally evaporated to fabrication thin films and devices. The organic materials are loaded in crucibles of ceramics or metal such as tungsten and tantalum. The crucibles are then heated by electric current through metal electrodes and wires. With the thermal energy, materials are evaporated from the crucible and travel in the chamber in a ballistic way with the mean free path longer than the dimension of the vacuum chamber. This

requires the pressure usually below 2e-6 Torr. When the materials reach the surface of the substrate in the vacuum chamber, they stick to the substrate and the film grows. The film growth rate is usually 0.5-2 Å/s. The rate of the film growth is monitored by using quartz crystal microbalance (QCM). The thickness of the thin film is measured and calibrated by profilometer or ellipsometry. Two or even more different materials can be evaporated together from separate crucibles as long as the rates are monitored independently without cross-talk. Other than the organic materials, metals such as silver and aluminum are also deposited by thermal evaporation. Shadow masks are used to define the pattern of films. The pixel area of the device is defined by the overlap of two electrodes.

After the evaporation of all the layers, the devices are transferred out of the vacuum chamber and encapsulated, if needed, with cap glasses and UV-curable resin.

Characterization of OLEDs

Luminance-Current Density-Voltage (LJV) measurement is the most basic measurement of OLEDs. In the lab condition, voltage is applied and current is measured by a Keithley source-meter. The brightness of the OLED is measured by a silicon photo-diode and calibrated by a luminance meter. Device pixel area is measured by optical microscope. Then the current efficiency can be calculated by

$$CE = \frac{\text{Luminance} \times \text{Pixel Area}}{\text{Current}} \quad (1-28)$$

Due to the optical cavity effect, the emission spectrum and intensity of OLEDs are angle-dependent. A rotation stage is needed to perform angle-dependent measurement. An optical fiber is used to collect the emission and a connected

spectrometer is used to measure the emission spectrum. The spectrometer is calibrated with a standard tungsten lamp.

As mentioned previously, EQE is also very important in characterizing the performance of OLEDs. It requires collecting the emission towards all directions. One way to realize this is to measure and integrate the angular dependent photon count. Another way is to use the integrating sphere. The integrating sphere is calibrated using a standard lamp. By using the integrating sphere, the absolute integrated spectrum of the OLEDs can be directly measured, which then can be converted to total photon count by integration over the spectrum. In a similar way to calculate EQE, the power efficiency can also be calculated by collecting emission towards all the directions considering the photopic responsivity.³¹

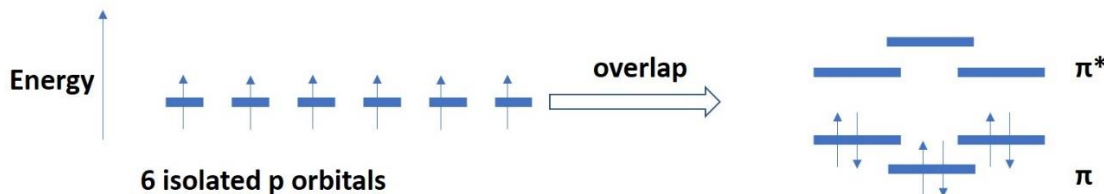


Figure 1-1. A schematic showing the molecular orbitals and energy diagram of benzene.³²

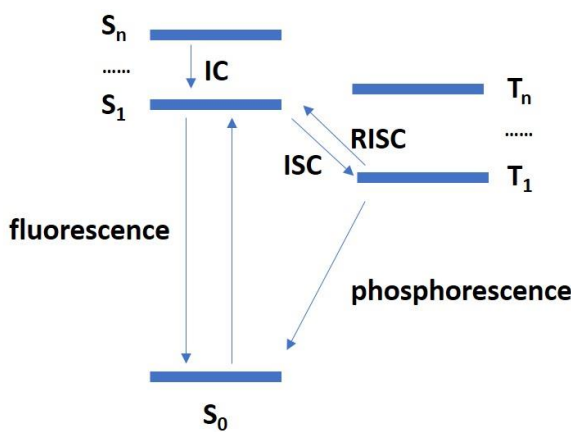


Figure 1-2. The Jablonski diagram showing the main electronic processes in an organic molecule.

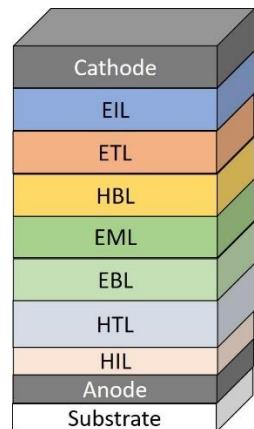


Figure 1-3. A schematic showing a typical OLED stack structure. The thicknesses are not to scale.

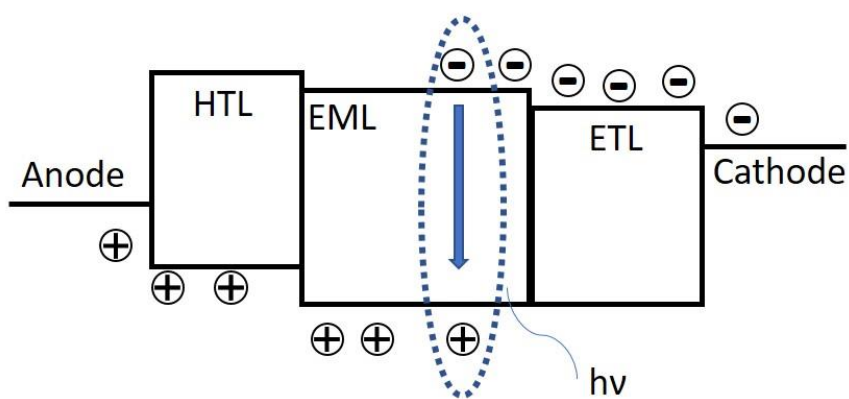


Figure 1-4. A schematic showing the working mechanism of an OLED under voltage bias.

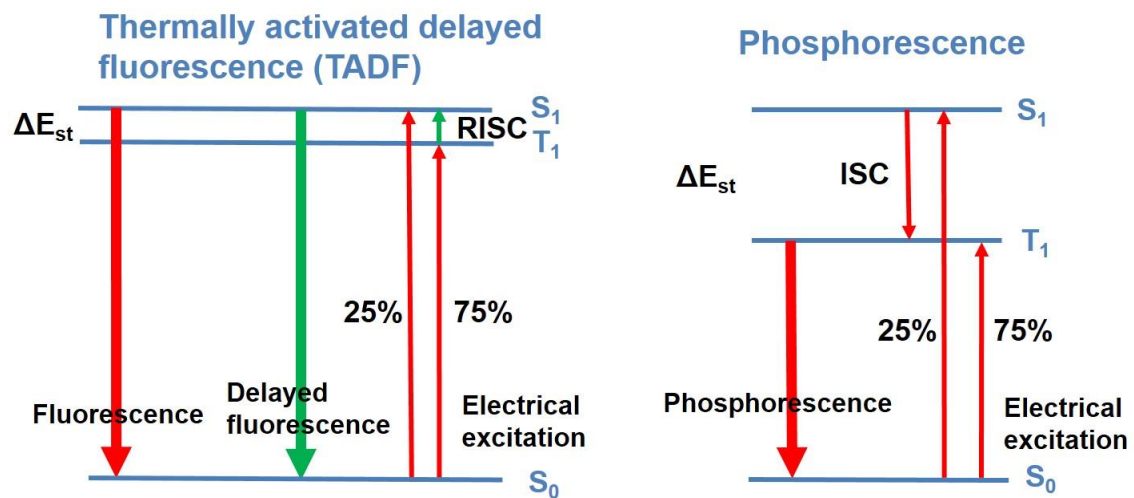


Figure 1-5. Schematics showing the working mechanisms of phosphorescence and TADF.

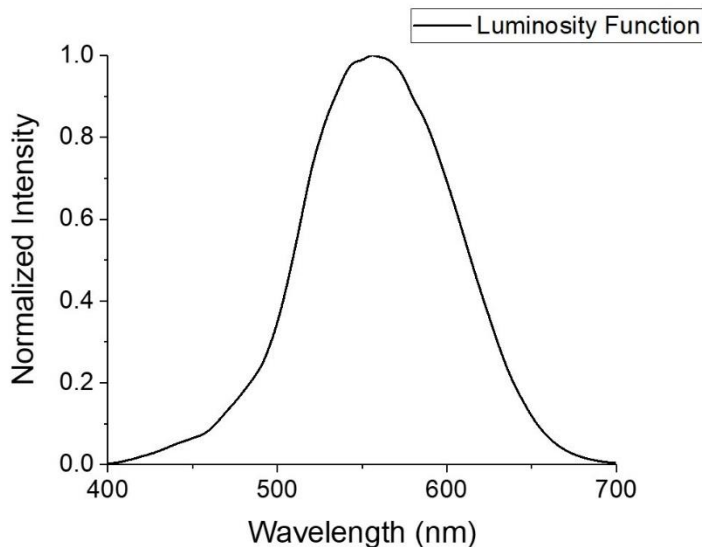


Figure 1-6. CIE "physiologically-relevant" luminous efficiency function (the Stockman & Sharpe cone fundamentals).

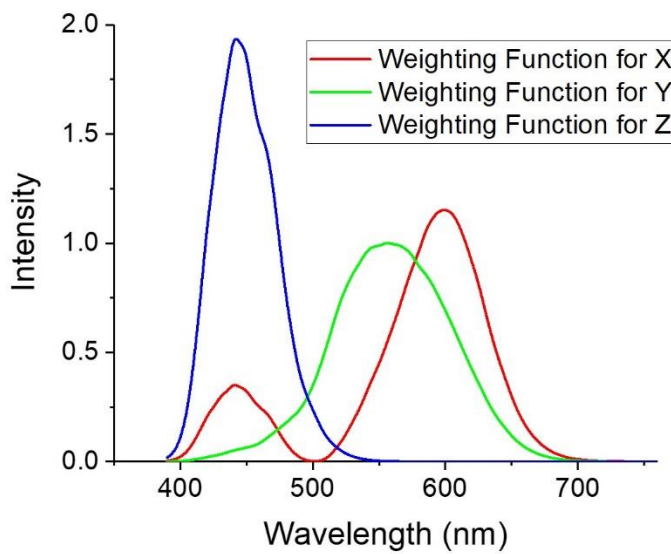


Figure 1-7. The CIE standard observer color matching functions.

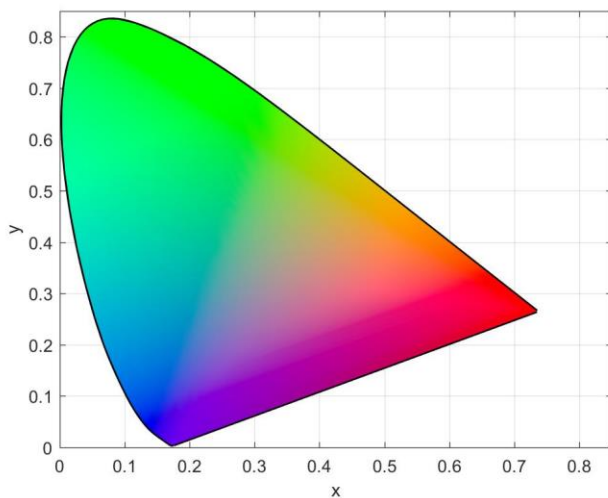


Figure 1-8. The CIE 1931 color space chromaticity diagram.

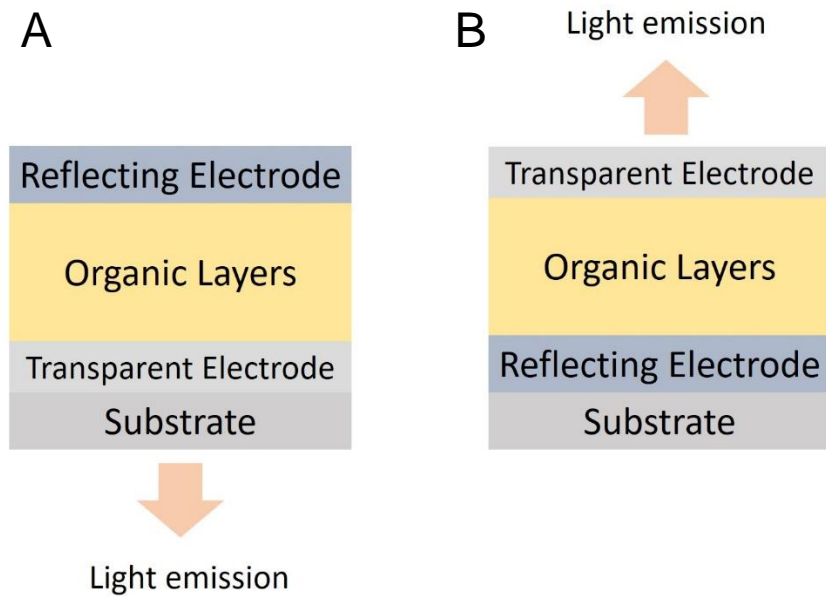


Figure 1-9. Schematics showing the typical device configurations. A) Bottom emission OLED. B) Top emission OLED.

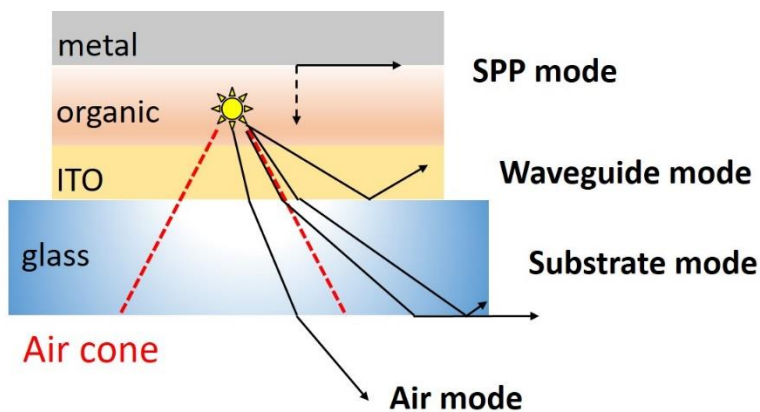


Figure 1-10. A schematic depicting the main energy dissipation channels in a typical bottom emission OLED.

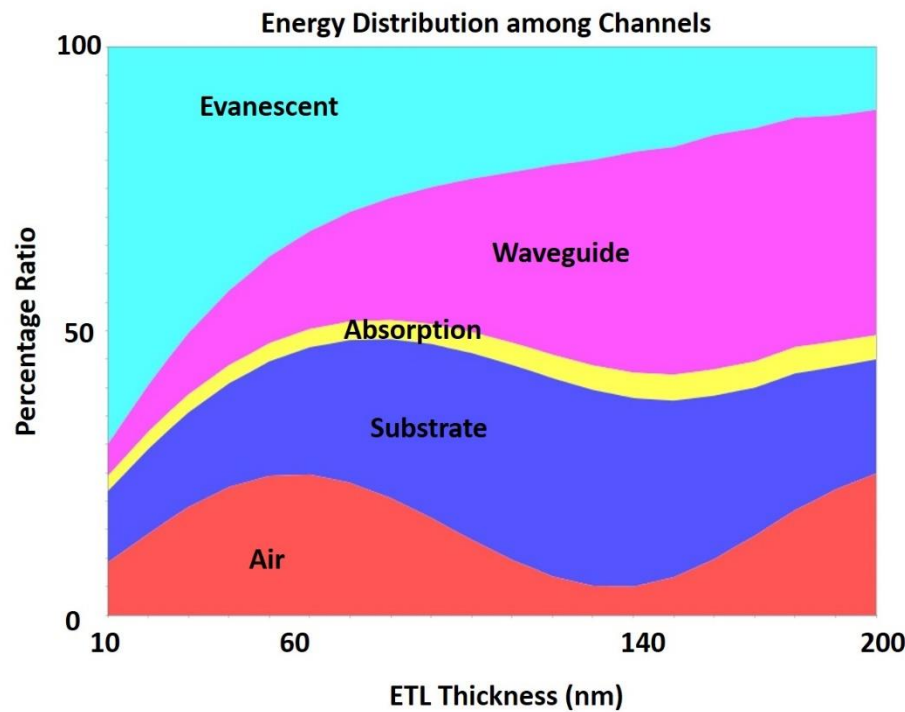


Figure 1-11. The energy distribution into the main energy dissipation channels as a function of ETL thickness in a typical bottom emission OLED.

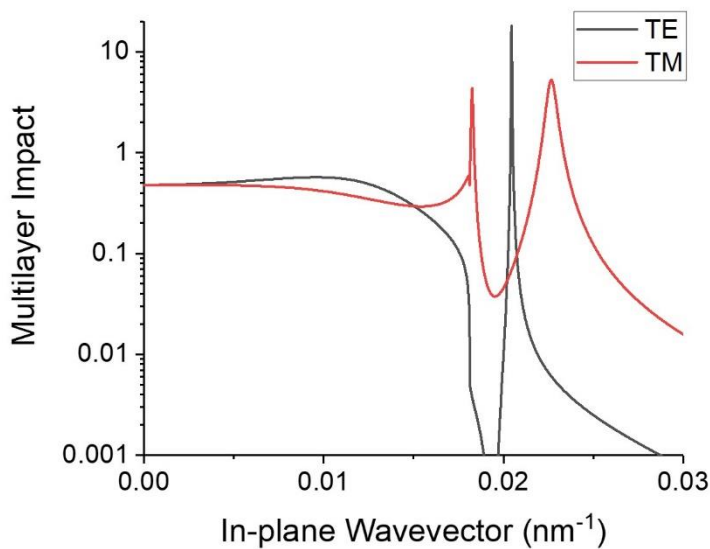


Figure 1-12. Multilayer impact at 520 nm of a typical bottom emission OLED.

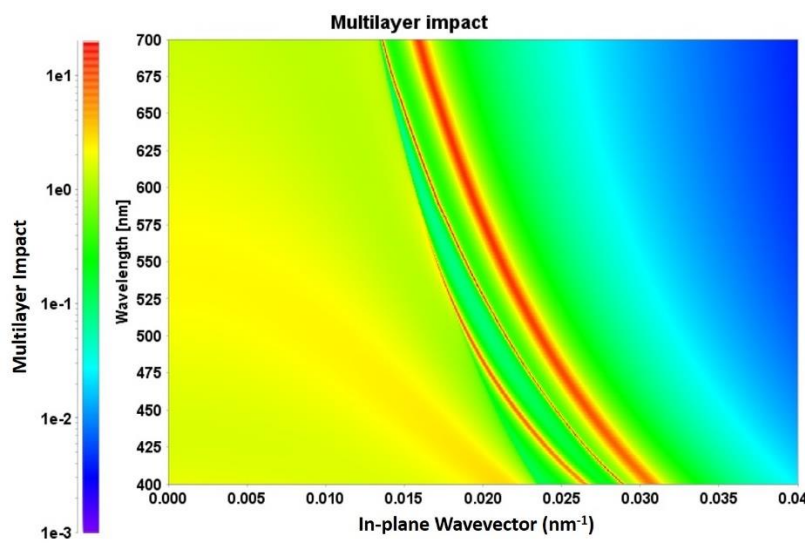


Figure 1-13. A 2D contour of the multilayer impact of a typical bottom emission OLED at different wavelengths.

CHAPTER 2

BILAYER CORRUGATED STRUCTURS AND THEIR APPLICATIONS IN OLED

Introduction

Limited by the high refractive indices of the organic materials,³³ ITO and the glass substrate, the light extraction efficiency of common bottom emission OLEDs is limited to 25-30%.^{17, 22, 24, 34-36} One of the commonly used approaches to exceed this limitation is to corrugate the interfaces, i.e. to make the interfaces optically nanostructured. When the in-plane periodicity of the nanostructure is comparable to the visible wavelength, the corrugated structure is found to be effective to extract trapped modes. Most of the corrugated structures are fabricated on the substrate before the deposition of the OLEDs on top. Herein, a simple process will be introduced to fabricate a corrugated OLED containing a corrugated bilayer ETL. This corrugated bilayer ETL consists of two electron transport organic semiconductor materials with tremendously different glass transition temperatures. Due to the big difference in the thermal and the mechanical properties, upon annealing, bilayer corrugated structure forms. We show that the morphology of the corrugated structure can be tuned by the annealing temperature and the thicknesses of the two layers. We then demonstrate a corrugated OLED with the corrugated bilayer ETL. With an appropriate combination of materials and annealing temperature, we show that the corrugated OLED with a 35% higher current efficiency compared to a planar control OLED. Additionally, the operational lifetime of the corrugated OLED is greatly improved compared with the control device with the LT90 from 1000 cd/m² enhanced by 100 times.

Bilayer Corrugated Structure Fabrication and Characterization

The corrugated structure formed by thermally annealing a thin metal film on elastomer has been investigated.³⁷ The corrugated structure is formed due to the big difference in the thermal expansion coefficient between the two materials. Upon annealing, the metal, which has a much smaller thermal expansion coefficient, induces a compressive strain in the underlying elastomer, which has a larger thermal expansion coefficient. When the annealing temperature is higher than a critical value, the compressive strain causes the bilayer to corrugate. Our idea of the bilayer organic corrugation is based on a similar strategy.

Two materials with very different thermal and mechanical properties are needed to realize similar phenomena. Though the thermal expansion coefficients of organic thin films are not widely reported, the glass transition temperature reflect the thermal property. The glass transition temperature indicated how easily in terms of thermal energy the molecules in the film start to move with a significant magnitude. Like the thermal expansion coefficient, the glass transition temperature is strongly related to the interaction between molecules. In literature, researchers already found that polymers with a higher glass transition temperature generally possess a smaller thermal expansion coefficient.³⁸ It is reasonably expected that small molecules have a similar trend. Therefore, we propose to make the bilayer corrugated structure with two materials with very different glass transition temperatures.

Among all the commonly used organic semiconductor materials, Tris(8-hydroxyquinoline)aluminum (Alq_3) is an ETL material with the glass transition temperature among the highest ~ 172 °C.³⁹ We chose 2-(4-biphenylyl)-5-(4-tert-butylphenyl)-1,3,4-oxadiazole (PBD) as the other ETL material, which is reported to

have a very low glass transition temperature ~60 °C.³⁹ We expect that Alq₃ has a much smaller thermal expansion coefficient than PBD does. A corrugated structure should form by annealing a bilayer sample with Alq₃ on top of PBD and later the results confirm this. Other than the combination of PBD/Alq₃, we found that other material combinations with very different glass transition temperatures can also form corrugated structures in a similar way upon thermal annealing. An example worth special attention is N,N' -bis(3-methylphenyl)-N,N' -diphenylbenzidine (TPD) with Alq₃. Fenter et al.⁴⁰ measured their thermal expansion coefficients and showed that TPD has an about 10-fold larger thermal expansion coefficient than Alq₃ does. Besides, TPD has a glass transition temperature around 60°C similar to PBD. This finding supports our model of the formation of corrugation with two organic materials, which correlates the thermal expansion coefficient with the glass transition temperature.

As the corrugation pitch and depth are important on the optical effect of the nanostructure to enhance the performance of OLEDs, in the initial series of experiments, we tried to optimize the corrugated structure by tuning the thermal annealing temperature and the layer thicknesses. The sample we fabricated has the following structure, glass/40 nm 2,2',2'' - (1,3,5-benzinetriyl)-tris(1-phenyl-1-H-benzimidazole) (TPBi)/PBD/Alq₃. TPBI was used as the underlying layer because in the real working OLED this material was used under the bilayer ETL. It was also found that the underlying layer has little effect of the morphology of the corrugated structure as long as the annealing temperature is not higher than the glass transition temperature of the underlying material. The schematic of the sample structure is shown in Figure 2-1.

We first investigated the effect of the PBD layer thickness on the final morphology with the annealing condition fixed at 70 °C for 30 min and the Alq3 layer thickness fixed at 20 nm. We varied the thickness of PBD (40 nm, 50 nm, 60 nm). Atomic force microscopy (AFM) was used to characterize the morphology of the corrugated structures. The images are shown in Figure 2-2. Fast Fourier transformation (FFT) was used to analyze the surface morphology periodicity. The results of the corrugation with 40 nm PBD are shown in Figure 2-2.

As shown by the AFM images, corrugated morphology is clearly formed on the samples. The root-mean-square (RMS) roughness of the corrugation increased from 31.9 nm to 39.3 nm with the PBD thickness increased from 40 nm to 60 nm. On the 60 nm PBD sample, large particles are seen and the corrugation is not as well-defined as on the other samples probably due to the crystallization of PBD layers as the annealing temperature is already higher than the glass transition temperature of PBD. The other two samples with thinner PBD layers show clearer corrugation. According to the FFT analysis, the peak in-plane period is about 1.3 μm for 40 nm PBD sample and is about 1.5 μm for the 50 nm PBD sample, while the corrugation depth for both samples is about 100 nm. Figure 2-2 shows the AFM section profile image of the 40 nm PBD layer corrugation, from which the depth can be clearly seen. The power spectral density as a function of in-plane period from the FFT analysis for the 40 nm PBD layer corrugation shows a broad peak of period at 1.3 μm. The morphological images and the broad distribution of in-plane period are in consistency with the morphology of the PDMS/AI corrugation in the literature.²⁴

We second investigated the effect of Alq₃ thickness on the corrugation morphology. The thickness of PBD is fixed at 40 nm and the annealing condition is fixed at 70 °C for 30 min. The thickness of Alq₃ is varied at 15 nm, 20 nm and 25 nm. The AFM images of the resulting morphology of the corrugations are shown in Figure 2-3.

Textured morphology developed on all three samples, while only the 20 nm Alq₃ sample shows a clear corrugation, which implies the sensitivity of the corrugation morphology on the Alq₃ thickness. A well-defined corrugation only forms at a narrow range of Alq₃ thickness, which is near 20 nm.

We third investigated the effect of the annealing temperature on the morphology of the corrugation. The layer thicknesses are fixed at PBD 40 nm and Alq₃ 20 nm. Three annealing temperatures 50 °C, 60 °C and 70 °C were tested. The AFM images are shown in Figure 2-4.

The surface roughness increased with a higher annealing temperature. The RMS roughness is 14.3 nm for the 50 °C sample, 24.2 nm for the 60 °C sample and 31.9 nm for the 70 °C sample. The increased surface roughness can be due to a higher interfacial strain between the two materials at a higher annealing temperature.

Corrugated OLED Fabrication and Characterization

The corrugated structure with 40 nm PBD and 20 nm Alq₃ was incorporated as an ETL in the OLED. The performance of the corrugated OLED was then compared with a control device with the same stack without annealing. The device structure is glass/indium tin oxide (ITO)/poly(3,4-ethylenedioxythiophene) polystyrenesulfonate (PEDOT:PSS) (~30 nm)/ 4,4' -cyclohexylidenebis[N,N-bis(4-methylphenyl)-benzenamine] (TAPC) (35 nm)/2,2' ,2'' -(1,3,5-benzinetriyl)- tris(1-phenyl-1-H-

benzimidazole) (TPBi) doped with 8 wt % iridium, tris[2-(2-pyridinyl-N)phenyl-C]
(Ir(ppy)₃) (30 nm)/ TPBi (20 nm)/PBD (40 nm)/Alq₃ (20 nm)/(thermal annealing)/Alq₃ (6
nm)/LiF/Al. The OLED structure and the energy diagram is shown in Figure 2-5.^{2, 6, 15, 41-}

44

The corrugated device and the control device are all the same in fabrication up to finishing depositing 20 nm Alq₃. The corrugated device was then thermally annealed in nitrogen atmosphere in a glovebox at 70 °C for 30 min. During annealing, corrugation formed with the in-plane period peaking around 1.3 μm and the corrugation depth around 100 nm as shown in the AFM image in Figure 2-2. The samples were transferred back to the vacuum chamber after annealing and the rest of the stack was deposited. The entire process was done without any exposure to the ambient. The control devices were fabricated in the same run only without the annealing step. After the deposition of the whole stack, all the devices were encapsulated and LJV characterization was done. Angle-dependent emission intensity was measured and EQE was calculated based on that. Device performance is plotted in Figure 2-6.

Compared with the control device, the corrugated device shows a 35% increase in CE and 20% in EQE at the luminance range from 10 cd/m² to 10000 cd/m². This bias-independent improvement implies that the enhancement results from the optical effect. The different amount of increase in CE and EQE is from the difference in emission spectrum and angular dependence. The enhancement is suspected to come from the extraction of the WG mode and the substrate mode. Note that the entire thickness of the optical cavity including the ITO and the organic layer is less than 300 nm, while the

thickness modulation of the corrugation structure is as large as 100 nm. This modulation is expected to distort the WG mode significantly.

The lower current density of the corrugated device is also worth attention. With a modulated thickness across the pixel, the current was expected to be higher than the planar control device, given the amount of materials are the same for both devices. This might be due to the change in transport property of the ETL. A series of three types of electron dominant devices (EDD) with the bilayer PBD/Alq₃ ETL were fabricated to look into this point. One of the EDDs is the control device without any annealing. The other two were annealed at 60 °C and 70 °C for 30 min, respectively. The device structure and the energy diagram are shown in Figure 2-7 with the JV curves of the three EDDs.

It can be clearly seen that the 60 °C annealed EDD shows the lowest current at the same voltage, almost one order of magnitude than the control planar device, while the 70 °C annealed device has a higher current than the 60 °C annealed one but lower than the planar control one. Though the 70 °C annealed device shows a higher current at low voltages (below 8 V), we attribute this to the leakage current due to the 100 nm thickness modulation. There can be two effects on the current of the EDD due to annealing. The annealing of the material itself decreases the current probably due to the rearrangement of molecules that influences the material mobility. The corrugation increases the current due to the thickness modulation. These two effects take place in the meantime. For the 60 °C annealed device, the decrease is dominating, so the current is much lower than the control device. While the increase becomes more pronounced in the 70 °C annealed device due to more surface roughness shown by the previous AFM images, which lifts the current. But the decrease is still dominating, giving

rise to an overall lower current compared with the control device. The decrease in the electron current in the ETL of the corrugated device gives rise to the lower current in the OLEDs.

In the OLED stack, the HTL material TAPC has a 100 times higher charge mobility than both the materials in the PBD/Alq₃ bilayer ETL. It is expected that the entire device is imbalanced in charge with a dominating hole current. With this said, the further decrease in electron current due to annealing makes the imbalance even worse, which is supposed to lower the device efficiency. Therefore, the overall enhancement in device efficiency by corrugation suggests that the corrugated structure improves the light extraction efficiency of the OLEDs.

One may argue about the generally low efficiency of the devices compared with the reported values in the literature. One possible reason is the PBD ETL. Devices replacing the 40 nm PBD/20 nm Alq₃ bilayer ETL by a 60 nm Alq₃ ETL were fabricated and the peak efficiency was 53 cd/A, higher than the control device.

It is also interesting to look at the effect of thermal annealing on the device performance. Since it is impossible to make annealed planar device with PBD/Alq₃ ETL, a series of OLEDs with Alq₃ ETL were fabricated and treated with different annealing conditions. Either annealing the TPBi HBL or annealing the Alq₃ ETL did not change the efficiency by more than 10%, further confirming the key role of the PBD layer and the resulting corrugated structure in the device performance improvement.

Finally, the operation stability of the corrugated OLED was compared with the control planar device. A more stable HTL material N,N' -di(1-naphthyl)- N,N' - diphenyl-(1,1' -biphenyl)-4,4' -diamine (NPB) was used instead of TAPC. Other the

HTL, the entire device stack in this stability test was the same as in the efficiency test. The stability test was done by driving the device at a constant current density. The starting luminance was set to be 1000 cd/m^2 . To achieve this initial luminance, the current density of the control device was around 3 mA/cm^2 and that of the corrugated device was around 2 mA/cm^2 . The luminance was recorded as a function of time as plotted in Figure 2-8.

The corrugated device shows 100 times longer LT90 compared with the control device. We suspected that this improvement is due to an improved morphological stability. As PBD has a very low glass transition temperature, the morphological change caused by local joule heat during continuous drive contributes to the degradation of the control device.⁴⁵ The change probably due to the recrystallization of PBD could cause the delamination of the top electrode.⁴⁶ Significant morphological change can even be observed by the naked eyes after the encapsulated control device was stored in a dry box for one day.

On the contrary, the thermal annealing used to produce the corrugated device before the deposition of the top electrode already relaxed the stress due to the thermal property mismatch. The later continuous drive of the device can hardly raise the temperature above the annealing temperature $70\text{ }^\circ\text{C}$.⁴⁷ Little morphological change is expected during the stability test, which contributes to the much better stability of the corrugated device.

Summary and Conclusions

In this chapter, the fabrication and characterization of a bilayer corrugated structure are discussed. The corrugated structures were formed by simple thermal annealing of bilayer samples with two organic materials with very different glass

transition temperatures. The corrugation morphology can be controlled by layer thicknesses and the annealing temperature. A bilayer ETL consisting of PBD/Alq₃ can be incorporated into OLEDs as an active layer. Compared with the control device, the corrugated OLED with the bilayer corrugated ETL shows a 35% higher current efficiency. EDDs were fabricated and the results show that the corrugated ETL has a lower current than the planar one, confirming the optical effect of the corrugated structure. More interestingly, the corrugated OLED has a much better operational stability with 100 times longer LT90 from 1000 cd/m² compared with the control device.

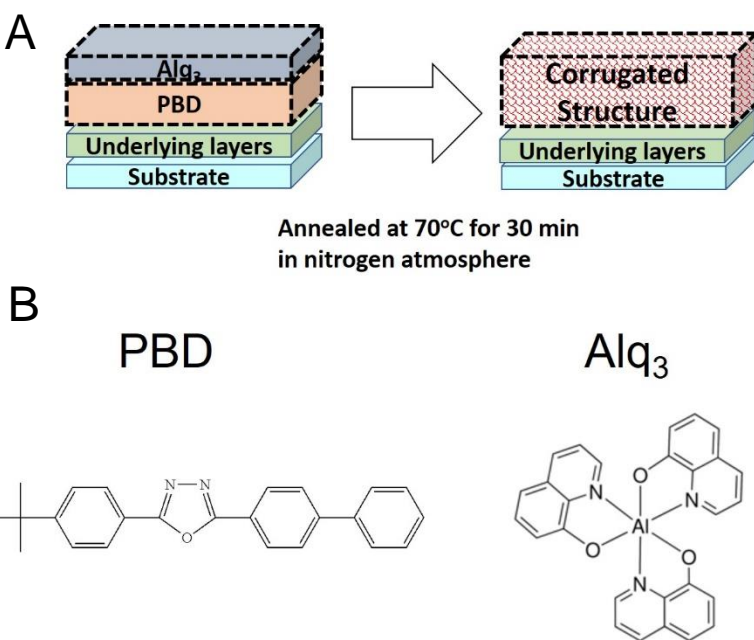


Figure 2-1. Bilayer corrugation sample structure and materials. A) A schematic showing the material stack and the fabrication process for the PBD/Alq₃ corrugation under investigation. B) The molecular structures of PBD and Alq₃.

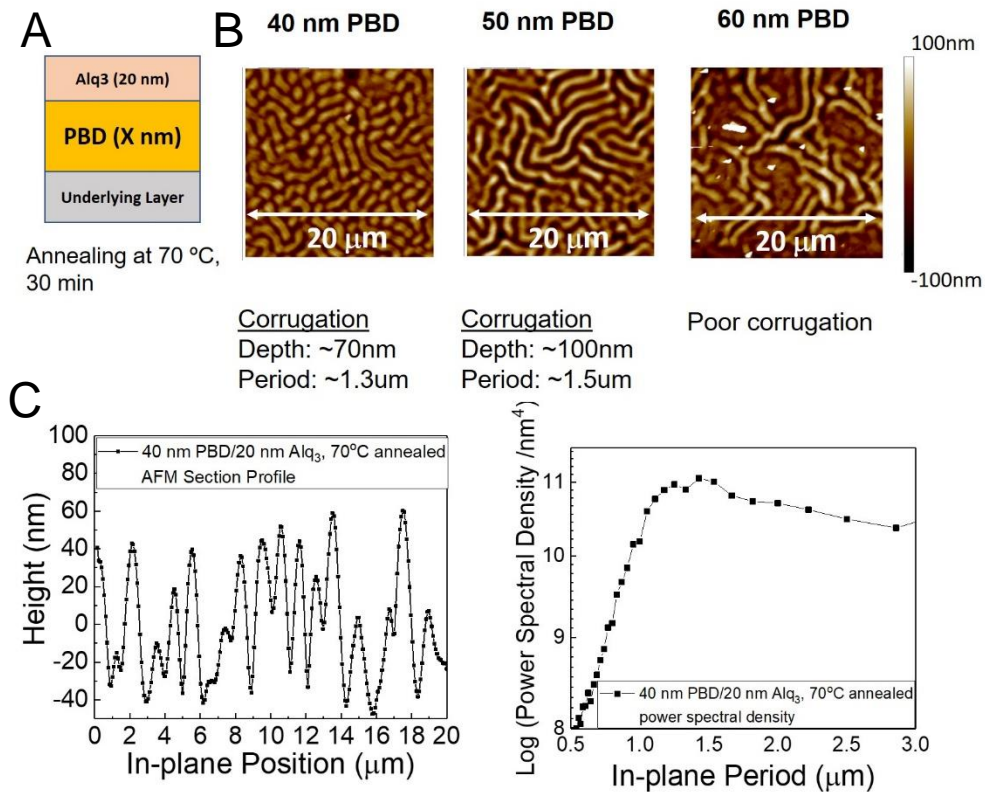


Figure 2-2. Morphology control by PBD thickness. A) Sample structure. B) AFM images of substrate/TPBi/PBD/Alq₃ (20 nm) samples with different PBD thicknesses annealed at 70 °C for 30 min. C) The section profile image and the power spectral density by FFT for the 40 nm PBD corrugation.

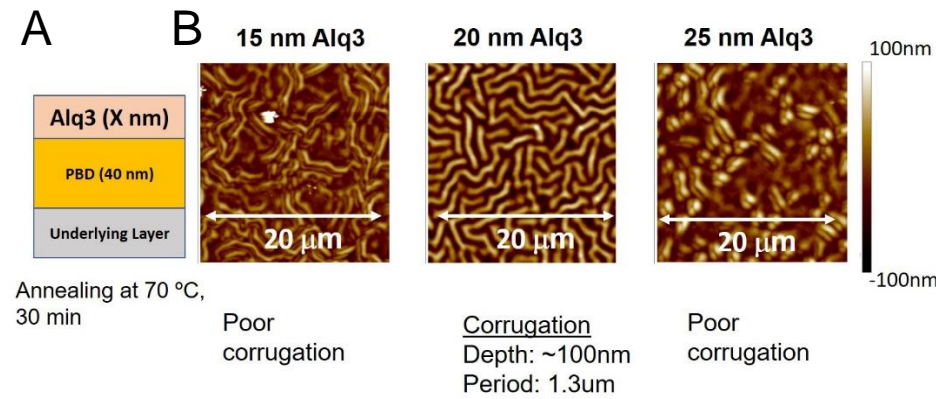


Figure 2-3. Morphology control by Alq₃ thickness. A) Sample structure. B) AFM images of substrate/TPBi/PBD (40 nm)/Alq₃ samples with different Alq₃ thicknesses annealed at 70 °C for 30 min.

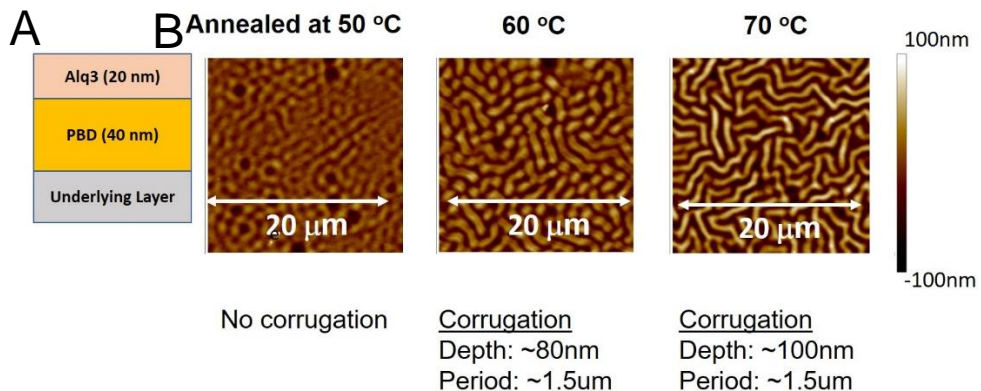


Figure 2-4. Morphology control by annealing temperature. A) Sample structure. B) AFM images of substrate/TPBi/PBD (40 nm)/Alq₃ (20 nm) samples with different annealing temperatures.

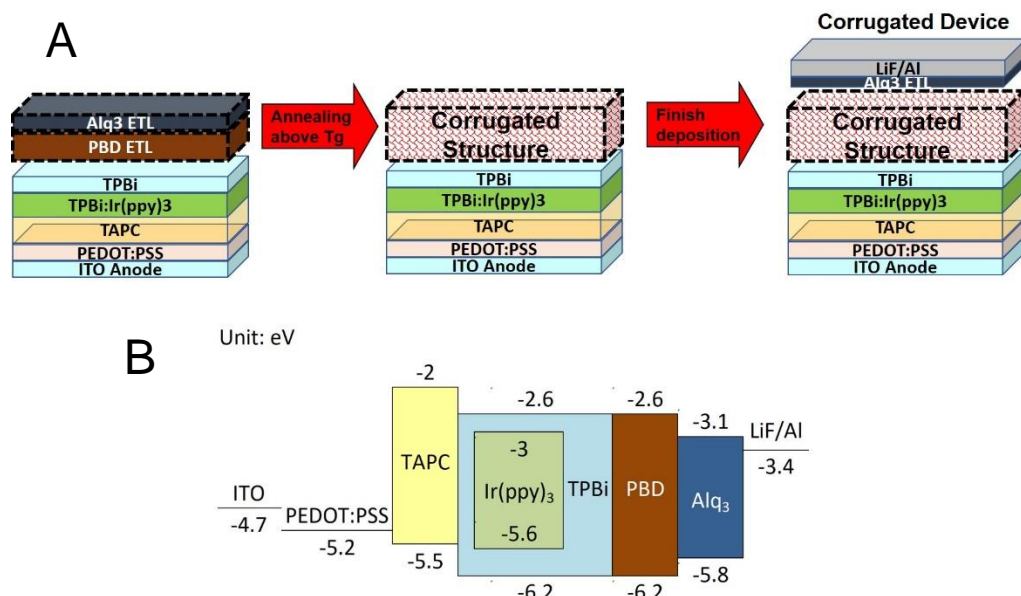


Figure 2-5. Corrugated OLED fabrication and structure. A) Schematics showing the corrugated OLED fabrication process. B) Energy diagram of the OLED stack.

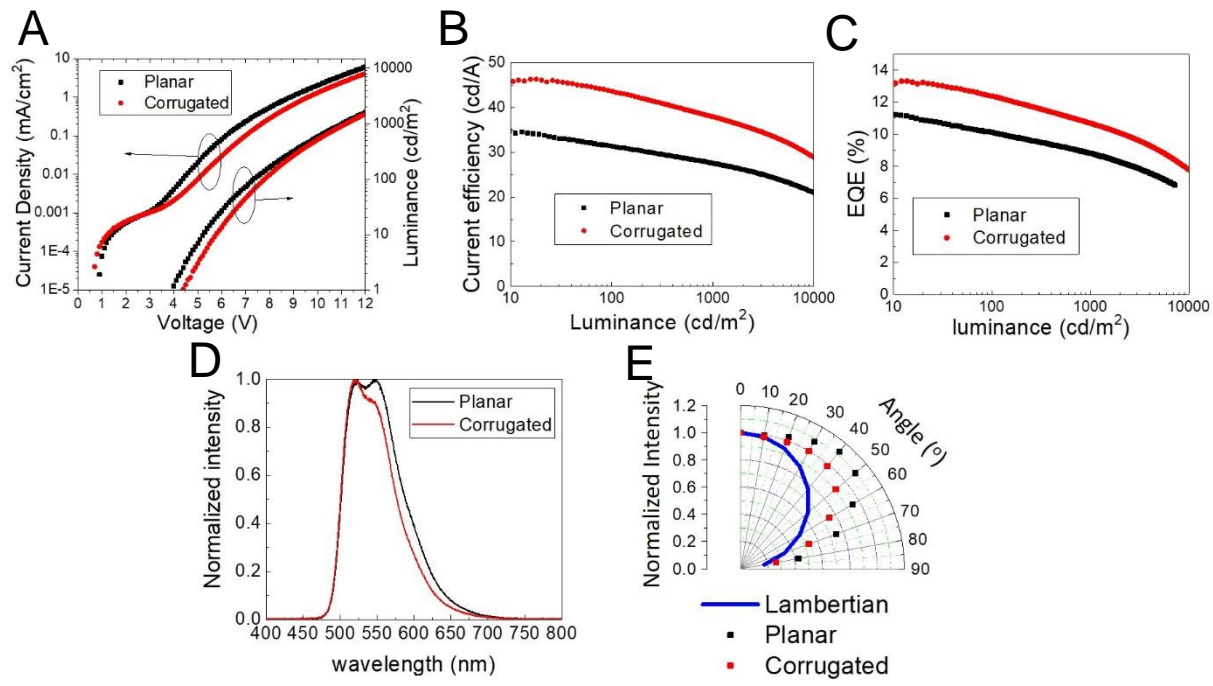


Figure 2-6. The performance of the corrugated OLED (red) and the control planar OLED (black): A) LJV characterization. B) current efficiency. C) EQE. D) EL spectra in the forward direction. E) Angle-dependent EL intensity with the Lambertian distribution.

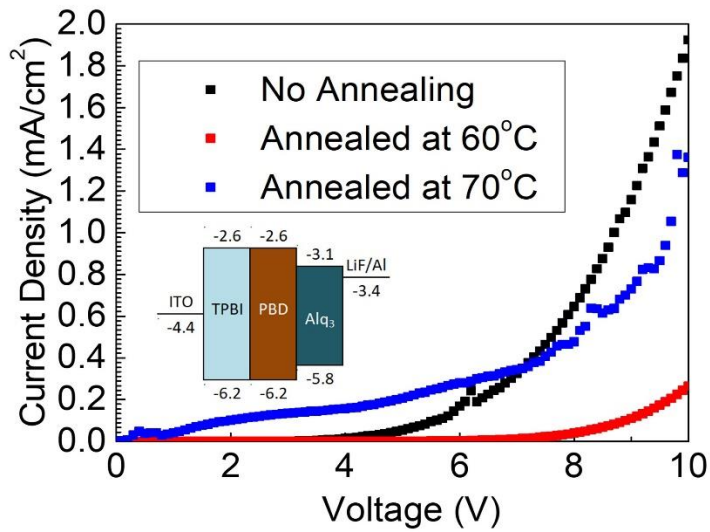


Figure 2-7. The electron dominant device JV performance with the device energy diagram included.

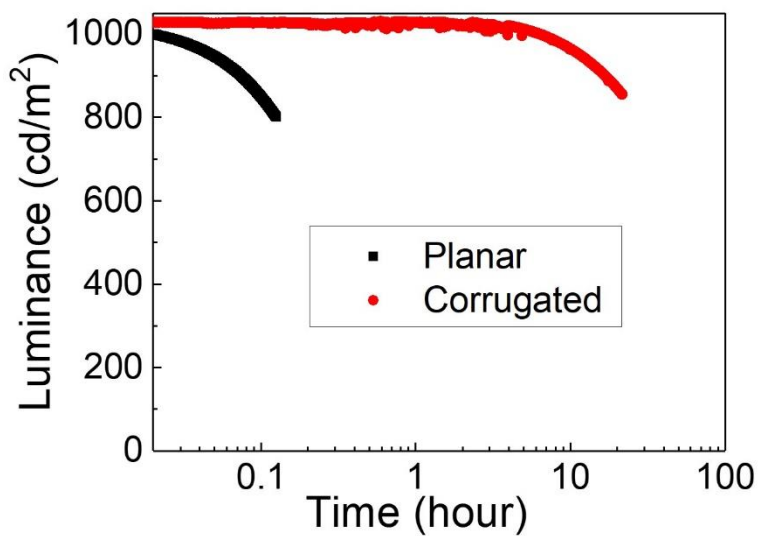


Figure 2-8. The operational stability performance of the corrugated OLED and the control planar OLED.

CHAPTER 3
QUANTITATIVE MODE ANALYSIS OF CORRUGATED OLEDs FROM ANGLE
RESOLVED ELECTROLUMINESCENCE SPECTROSCOPY DATA (ARES)

Introduction

Corrugated structures to enhance the light extraction efficiency of OLEDs are widely used and extensively studied. Surface-modulated structures with a sub-wavelength period can extract waveguide (WG) mode and surface plasmon polariton (SPP) mode by providing an additional in-plane wave vector component to satisfy the boundary condition of electromagnetic wave coupling across the interface between the organic dielectric material and air. The change of in-plane wave vector brought by the sub-wavelength periodic structure can be experimentally measured by angle-resolved spectra measurement and described by Bragg diffraction equation.⁴⁸⁻⁵⁰

$$\overrightarrow{k_{final}} = \overrightarrow{k_{original}} + \overrightarrow{\Delta k} \quad (3-1)$$

Where, $\overrightarrow{\Delta k}$ is the additional in-plane wavevector brought by the periodic structure, related to the in-plane periodicity by,

$$|\overrightarrow{\Delta k}| = \frac{2\pi}{d} \quad (3-2)$$

Where d is the in-plane period.

In a typical planar OLED structure, the in-plane wavevectors $\overrightarrow{k_{original}}$ of the trapped WG mode and SPP mode are bigger than the total wavevector in air $\overrightarrow{k_0}$. By adding $\overrightarrow{\Delta k}$, the magnitude of the resulting in-plane wavevector $\overrightarrow{k_{final}}$ can be smaller than that of $\overrightarrow{k_0}$ so that this mode can be coupled in air, contributing to the light extraction efficiency.

By studying one-dimensional structures with a single $\overrightarrow{\Delta k}$ associated with the structure, researchers already found that for shallow structures (depth on the order of

50 nm with a period on the order of 500 nm), Bragg diffraction equation works accurately for allocation of the features that appear in the angle resolved spectra measurement. However, little has been reported about quantitatively analyzing the extraction efficiency of each mode brought by the periodic structures. The question remains to be answered that how much light is extracted from each trapped mode.

Other than one-dimensional structures, two-dimensional structures, of which $\overrightarrow{\Delta k}$ has non-zero components in both orthogonal in-plane directions, are of special interest in that most structures relatively simpler to realize have a two-dimensional structure with a short-range order. The term ‘poly-crystal’ structure will be used to refer to this kind of structures. In contrast to one-dimensional ‘grating’ structures, OLEDs with ‘poly-crystal’ structures do not have sharp semi-linear features in the w-k plot. Features are ‘blurred’ and ‘broadened’, making the quantitative analysis of the extraction efficiency of each trapped mode more challenging.

Indeed, the ‘poly-crystal’ structures can be viewed as an average of a ‘single-crystal’ hexagonal close-packed structure over all the azimuth angles around the out-of-plane normal direction. Such a ‘single-crystal’ structure provides the access to the analysis of the ‘poly-crystal’ structures. This chapter will talk about the methodology to derive the extraction efficiency of WG mode and SPP mode by using two-dimensional structures from angle-resolved spectra data of OLEDs. First, the semi-quantitative simulation of the angle-resolved spectra of OLEDs with ‘single-crystal’ structures will be described. Second, the simulation will be compared with measured data to find the scattering strength. Third, the scattering strength will be used to calculate the scattering

efficiency of each mode. Fourth, the methodology will be applied in the analysis of ‘poly-crystal’ structures.

Simulation of ‘Single-Crystal’ Nanostructured OLEDs

Considering Bragg diffraction equation on a two-dimensional structure, all the three vectors in this equation do not have to be parallel or antiparallel as depicted in Figure 3-1.

In the depiction above, $k_0 = |\vec{k}_0| = \frac{2\pi}{\lambda}$ determines the range of the air cone. Φ is the angle between $\overrightarrow{k_{final}}$ and $\overrightarrow{\Delta k}$. Φ will be referred to as the reception angle in this chapter as it indicates the direction where the scattering event is received from.

This two-dimensional Bragg diffraction equation is the core of the simulation of the angle resolved spectra. The starting point is the power dissipation spectra as a function of in-plane wavevector of a planar OLED device. Since experimentally only the power dissipation spectra within the air cone can be obtained, the trapped part with bigger air cone can only be calculated. Below in Figure 3-2, it shows the three distinct features in k space of a planar OLED with the device structure we use in the experimental measurement.

In the Figure 3-2, the three features are nearly linear. At each wavelength, each feature is a narrow peak with a peak in-plane wave vector, which will be $\overrightarrow{k_{original}}$ in the scattering event.

On a ‘single-crystal’ hexagonal close-packed structure, only considering first-order scattering, there are six $\overrightarrow{\Delta k}$ with the same magnitude, that is each mode can be scattered to six directions. Each point in the final power dissipation spectra as a function

of in-plane wavevector has scattering events from six directions involved, that is six different reception angles. A schematic is shown in Figure 3-3.

Here the term ‘scattering strength’ will be used to refer to how strong the scattering is. The scattering strength of a mode will be depending on the scattering direction, the geometry of the features of the structure and the modal structure. The scattering strength is a function of the reception angle φ .

Since the simulated results will be compared with the measured results, the final target of the simulation is the angle resolved spectra considering scattering by the structures, which can be described in mathematics as a function $M_\varphi(E, k_{final})$, where E is the photon energy and φ denotes the relative orientation to one of the six $\vec{\Delta k}$. At first, $M_\varphi(E, k_{final})$ will be set to zero. As the scattering event does not change the photon energy, the calculation can be done independently for each photon energy. For each k_{final} in the final result, six Bragg diffraction equations can be solved with six reception angles, $\varphi + l * \frac{\pi}{3}$ ($l = 0, 1, 2, 3, 4, 5$). The six solutions $k_{original}$ will be obtained. We make an approximation that the scattering strength of each mode only depends on the reception angle and the modal structure, but not on the photon energy. We have,

$$M_{\varphi,j}(E, k_{final}) = \sum_i \sum_{l=0}^5 S_{i,j,\varphi+l*\frac{\pi}{3}} M_{0i}(E, k_{original,\varphi+l*\frac{\pi}{3}}) \quad (3-3)$$

Where i denotes the three modes TMWG, TEWG and SPP. $S_{i,\varphi+l*\frac{\pi}{3}}$ is the scattering strength as a function of modes and reception angle. $k_{original,\varphi+l*\frac{\pi}{3}}$ is the original wavevector associated with the scattering event with the reception angle $\varphi + l * \frac{\pi}{3}$. M_{0i} is the power dissipation spectra of the planar OLED decomposed to each mode calculated by simulation using Setfos. This decomposition can be done because the

three modes are well separated, especially considering TM and TE polarization. j denotes the polarization, s or p. It is interesting to see that the SPP mode, which has a TM nature, can actually be scattered to the s polarized light at some certain φ , which is a not surprising result of the change in the observation direction.

Using equation, we are able to simulate semi-quantitatively the angle resolved spectra of the OLED with the ‘single-crystal’ structure. The simulation is semi-quantitative because only the wavevectors of the features can be quantitatively allocated, but how strong each feature remains completely unknown. $S_{i,j,\phi}$ can only be obtained by comparing simulated and measured results. The simulation method to obtain $S_{i,j,\phi}$ will be briefly discussed in the next Chapter.

Calculation of Scattering Strength by Comparison between Simulation and Measurement

In order to compare the simulated and the measured results, the measured results have to be processed. Our first assumption is that the corrugated structure does not affect the original air mode and substrate mode. The scattered WG mode and SPP mode will appear in the final spectra as additional features. As the simulation is calculating these features, we need to extract these features from the measured data. In this work, the measured spectra of the control device fabricated in the same batch as the corrugated device will be used as the ‘baseline’ and by subtracting the ‘background’ from the measured data of the corrugated device, we can obtain the spectra only consisting of the ‘feature’. And then a direct comparison can be done between simulated and measured data. In Figure 3-4, four pairs of comparisons are shown.

In order to obtain the four figures showing the simulated data, $S_{i,j,\phi}$ was set to be such that the intensity of each mode in the simulation matches the measurement. The

positions of the features from simulation and measurement match very well, except for the part where the crossing of two features happens in (c). An anti-crossing behavior is clearly detected in the measurement,⁵¹ while our simulation based on Bragg diffraction equation is not able to predict such a behavior.

The main purpose of this comparison is to figure out the origins of the measured features, i.e. which feature is from which mode. Only after this successful assignment of features can we quantitatively estimate the extraction efficiency of each mode.

Note that all the three features are near-linear in the spectra of the planar OLED. However, curved features are observed in both the measured and the simulated spectra. This feature ‘shape’ transformation comes from the ‘non-parallel’ scattering of the mode, i.e. the scattering wave vector $\overrightarrow{\Delta k}$ is neither parallel nor anti-parallel to the original wavevector. This can be easily derived from Bragg diffraction equation.

Provided the reception angle φ , we have

$$k_{\text{original}}^2 = k_{\text{final}}^2 + \Delta k^2 - 2k_{\text{final}} \cdot \Delta k \cdot \cos\varphi \quad (3-4)$$

Approximately, $\overrightarrow{\Delta k}$ is not dependent on wavelength and k_{original} has a linear relationship with the photon energy. Assuming $k_{\text{original}} = a \cdot E + b$, where a and b are constants, we have,

$$(a \cdot E + b)^2 = k_{\text{final}}^2 + \Delta k^2 - 2k_{\text{final}} \cdot \Delta k \cdot \cos\varphi \quad (3-5)$$

Here two different examples will be given to show how the feature ‘shape’ transformation happens.

If the scattering is parallel or anti-parallel, and $\varphi = 0$ or π , we have

$$\begin{aligned} (a \cdot E + b)^2 &= k_{\text{final}}^2 + \Delta k^2 \mp 2k_{\text{final}} \cdot \Delta k = (k_{\text{final}} \mp \Delta k)^2 \\ k_{\text{final}} \mp \Delta k &= |a \cdot E + b| \end{aligned} \quad (3-6)$$

k_{final} has a linear relationship with the photon energy, too.

If the scattering is perpendicular to $\overrightarrow{k_{final}}$, $\varphi = \frac{\pi}{2}$, we have

$$(a \cdot E + b)^2 = k_{final}^2 + \Delta k^2$$

$$\left(\frac{E+b}{\frac{\Delta k}{a}}\right)^2 - \left(\frac{k_{final}}{\Delta k}\right)^2 = 1 \quad (3-7)$$

This is a hyperbola equation.

In the four sets of comparison shown in Figure 3-4, angle and wavelength are used instead of wave vector and photon energy to make the plots more straightforward. Considering that both k_{final} and E are inversely proportional to wavelength and k_{final} is proportional to the sine of the polar angle θ , we can easily have that $\sin\theta$ and λ have a linear relationship in the case of parallel or anti-parallel scattering and that they have a hyperbolic relationship in the case of perpendicular scattering. At small angles, $\sin\theta \approx \theta$. Therefore, the features still appear linear even on angle-wavelength plots. At larger angles, the deviation becomes more pronounced.

If k_{final} equals 0, we have

$$(a \cdot E + b)^2 = \Delta k^2 \quad (3-8)$$

This equation indicates that no matter what the reception angle is, all the resulting features originating from one mode (a certain pair of (a, b)) merge to one single wavelength (photon energy) in the normal direction ($k_{final} = 0, \theta = 0$). Knowing this, we can now easily understand the features we have in the simulated and measured results. There are apparently two bundles of features. One bundle merge at around 550 nm in the normal direction and the other bundle merge above 600 nm which we don't show in the figures because it cannot be confirmed in the measurement of a

green OLED device. In the simulation, we can easily predict that the merging point is at around 630 nm. By knowing the original wavevectors of each mode and Δk , we can easily figure out that the 550-nm bundle of features are scattered TMWG mode and the 630-nm bundle of features are scattered SPP mode. If we look closely at the measured figures, there are also very weak features merging at around 590 nm, they are scattered TEWG mode. For two reasons, TEWG is not included in the simulation. First, it is very weak compared to TMWG and SPP, which indicates that the scattering of TEWG is negligible and that the estimation of its scattering efficiency is trivial and very inaccurate. Second, the TEWG in the Setfos simulation is too sharp and very difficult to process in the later simulation to obtain the final spectra. This is due to the non-absorbing organic stack and ITO layer.

Note that the two detection angles 175° and 155° are not special angles regarding the symmetry of the structure. We can obtain information of scattering strength from 12 different reception angles for the two different polarizations. By tracking each feature in the simulation, we can figure out the reception angle associated with each feature. In Figure 3-5, assignments of each feature are shown.

As expected, the scattering events associated with angles close to parallel directions yield semi-linear shape features, while the scattering events associated with angles close to perpendicular directions yield curved shape features. Some of the SPP features with small reception angles are missing because they can only be seen at longer wavelengths which do not have detectable signals in the measurement of the green OLEDs. By comparing the features' intensity between measured and simulated

results, the scattering strength associated with each mode and reception angles can be obtained. The results are shown in Figure 3-6.

The scattering strength should be centrosymmetric as the entire system is. This makes it possible to evaluate the scattering strength of the missing features in the measurement. Also, within the error, the scattering strength has reflection symmetry as the entire system does. Based on these plots, we can see that all features appear in each plot with no scattering strength equal to zero. Even the feature of SPP mode from 175° appears in the S polarized plot, though very weak. This might be due to the imperfect alignment of the polarizer. The absolute value of the scattering strength does not have physical significance, but the comparison between TMWG and SPP mode scattering can be done. In general, the scattering strength of SPP mode is 50% higher than that of TMWG mode.

Even though the measurement and simulation are only done with two non-special detection angles 175° and 155° , we have 24 points covering the entire scattering strength curves, which already enables us to estimate the scattering efficiency of each mode without measuring the spectra at other detection angles. Ideally, measurement and simulation can be done with all detection angles from 0° to 30° , given the symmetry of the system, with arbitrary angle increments. However, this requires much more time. Here it will be shown that how the scattering efficiency is calculated from the scattering strength plots shown in Figure 3-6.

Calculation of Scattering Efficiency of Trapped Modes

First, the amount of intensity in the features can be calculated.

$$I_i = \sum_{k_{final}} \sum_E \sum_{\varphi=0^\circ}^{360^\circ} \sum_j \sum_{l=0}^5 S_{i,j,\varphi+l*\frac{\pi}{3}} M_{0i}(E, k_{original,\varphi+l*\frac{\pi}{3}}) \quad (3-9)$$

Given the six-fold symmetry of the system, we have,

$$I_i = 6 \times \sum_{k_{final}} \sum_E \sum_{\varphi=0^o}^{60^o} \sum_j \sum_{l=0}^5 S_{i,j,\varphi+l*\frac{\pi}{3}} M_{0i}(E, k_{original,\varphi+l*\frac{\pi}{3}}) \\ = 6 \times \sum_{k_{final}} \sum_E \sum_j \sum_{\varphi=0^o}^{360^o} S_{i,j,\varphi} M_{0i}(E, k_{original,\varphi}) \quad (3-10)$$

The entire curve $S_{i,j,\varphi}$ is constructed from the discrete scattering strength plots by linear interpolation. In the equation above, i denotes the mode, either TMWG or SPP. j denotes the polarization. With this equation, we can evaluate the amount of light intensity contained in the features of each mode. The next step will be the evaluation of the light intensity contained in the trapped modes of a planar device structure. This calculation can be done using the commercial software Setfos. Attention should be paid here as both the intensity in the extracted features from the corrugated device and the intensity in the trapped mode from the planar device have to be normalized to the baseline planar device angle resolved spectra data so that the comparison between them is relevant and the scattering efficiency can be calculated as the ratio of the extracted intensity to the originally trapped intensity. Below are two basic equations.

$$\text{Efficiency improvement} = \frac{\text{Total intensity in Features}}{\text{Total intensity in Baseline}} \quad (3-11)$$

$$\text{Mode scattering efficiency} = \frac{\text{Extracted intensity}}{\text{Originally trapped intensity}} \quad (3-12)$$

Using the first equation, it can be calculated that SPP contributes to $(9\pm1)\%$ enhancement in EQE. TMWG contributes to $(6\pm2)\%$ enhancement in EQE, considering 3 times wide feature width in the measurement plot compared with simulation. If TEWG contributes a negligible amount to the EQE, then the total enhancement should be $(15\pm2)\%$, which is a little more than the measured EQE enhancement from $\sim 20\%$ to $\sim 22\%$. Possible explanations for this discrepancy are as follows. First, in the calculation,

the measured data of the planar control device is used as the baseline to calculate the enhancement brought by the additional features. The assumption behind this is that the scattering structure does not alter the original air mode and substrate mode. If the baseline is lower than the measured control device data, then the total enhancement based the simulation is overestimated. However, this possible change in the original air mode and substrate mode cannot be analyzed based on features as they are both featureless. The featureless change in angle resolved spectra can be analyzed if the complication from the device stability issue and optical misalignment is avoided, which will not be included in this dissertation. Second, all the calculation and analysis presented here are purely optical, while the measured device efficiency does not only depend on device optics. On one hand, the charge imbalance or the non-unity PL quantum yield can lead to an EQE enhancement lower than the light extraction efficiency enhancement. On the other hand, as the corrugated structure not only impacts the optics of the device, but also impacts the electrical property of the device. The latter part is much less discussed about in literature, but the role it plays should not be neglected. Due to the inhomogeneity brought by the non-planar structure, injection and transport of carriers are also influenced. This electrical change alone can influence the device efficiency, which is beyond the scope of the optical analysis presented in this dissertation.

Based on Setfos simulation, originally the mode distribution is Air 28.6%, WG 15.4%, SPP 30.5%. Thus, the extraction efficiency of SPP is $28.6\% * 9\% / 30.5\% = (8 \pm 1)\%$ % and the extraction efficiency of WG is $28.6\% * 6\% / 15.4\% = (11 \pm 2)\%$.

Calculation of ‘Poly-Crystal’ Nanostructured OLEDs

As mentioned in the introduction, the simulation results from ‘single-crystal’ 6-folded close packed structures can be used to analyze ‘poly-crystal’ structures with the same peak in-plane period. Unlike ‘single-crystal’ structures, the scattering event now can happen towards random directions as depicted in Figure 3-7.

Therefore, the resulting spectra due to the Bragg diffraction by a ‘Poly-crystal’ structure can be constructed from the one by a ‘single-crystal’ structure by randomizing the detection angle φ . This can be well illustrated as shown in Figure 3-8.

The in-plane wave vector components k_x and k_y are related to φ by,

$$k_x = \frac{2\pi}{\lambda} \cos\varphi \quad (3-13)$$

$$k_y = \frac{2\pi}{\lambda} \sin\varphi \quad (3-14)$$

The two blurred features, one outer ring and one near the center, shown in the ‘poly-crystal’ structure figure can be constructed by simply averaging the ‘single-crystal’ structure figure over the polar angle, which indicates that the feature near the center is from the scattered WG mode and the outer ring is from the scattered SPP mode. This also shows that the blurring of features of the ‘poly-crystal’ structures does not necessarily come from the distribution of the in-plane period, i.e. a distribution of Δk . The blurring is also a direct result of angular averaging.

The scattering efficiency can be calculated as the two features are already assigned. The intensity contained in the features can be calculated after the baseline is subtracted from the measured data. The measured features are shown in Figure 3-9.

The weak feature on the left down corner is the scattered WG mode and the stronger feature is the scattered SPP mode. The scattering efficiency of each mode can

be calculated. SPP contributes to $(8\pm1)\%$ above baseline. WG contributes to $(0.2\pm0.1)\%$ above baseline. The total enhancement is $(8\pm1)\%$, which is less than the enhancement usually observed experimentally $\sim 20\%$. The discrepancy between them can be explained by similar reasons described in the ‘single-crystal’ situation. The extraction efficiency of each mode can also be evaluated. Originally the model distribution is Air 28.6%, WG 15.4%, SPP 30.5%. The extraction efficiency of WG is about 0%, while the extraction efficiency of SPP is about $28.6\% * 0.08 / 30.5\% = (8\pm1)\%$.

Summary and Conclusions

In this chapter, the methodology is described to analyze the angle-resolved spectra data of corrugated OLEDs. A detailed simulation method is described to construct the angle-resolved spectra of OLEDs with ‘single-crystal’ hexagonal corrugated structures. Based on the comparison between the simulated and the measured results, the scattering strength as a function of mode, reception angle and polarization can be extracted and can be used to evaluate the extraction efficiency of each mode by the corrugated structure. Then, the simulation results of the ‘single-crystal’ structure are used to analyze features in the angle-resolved spectra of OLEDs with ‘poly-crystal’ corrugated structures. The extraction efficiency of the ‘poly-crystal’ structure is also evaluated.

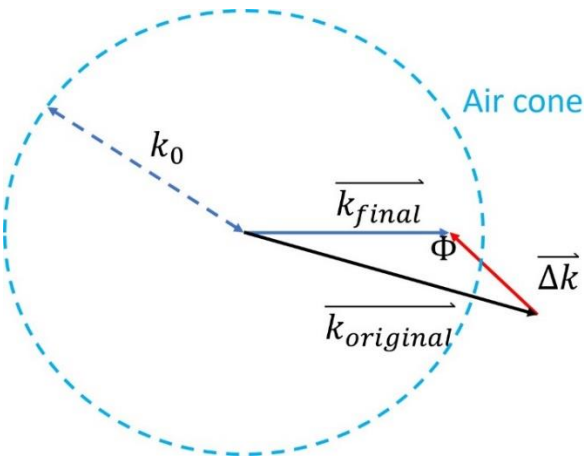


Figure 3-1. A schematic showing the air cone and Bragg diffraction equation.

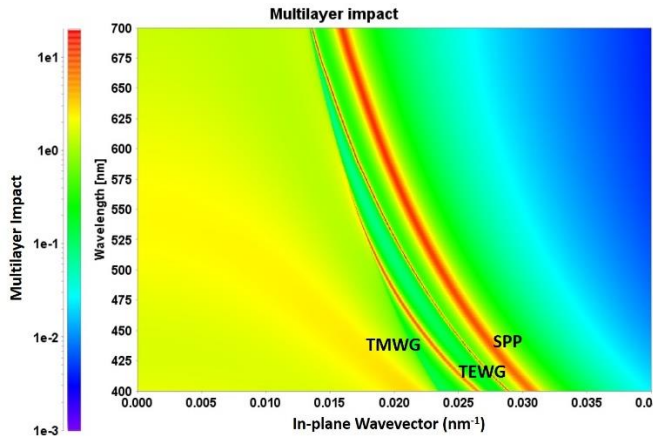


Figure 3-2. The multilayer impact spectrum as a function of in-plane wavevector of a planar OLED. The three features in red are TMWG, TEWG and SPP from left to right, respectively.

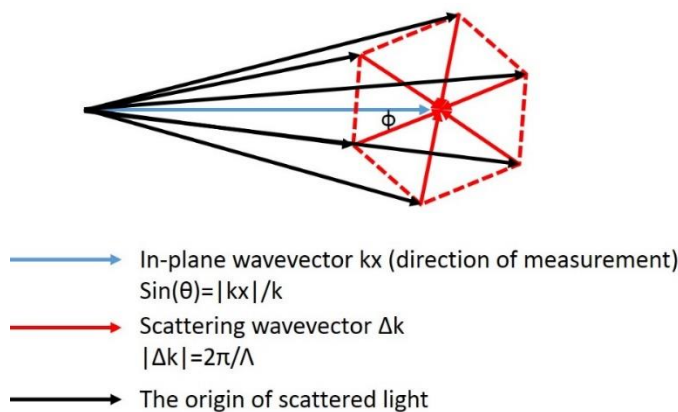


Figure 3-3. A schematic depicting the six-direction scattering associated with a hexagonal structure.

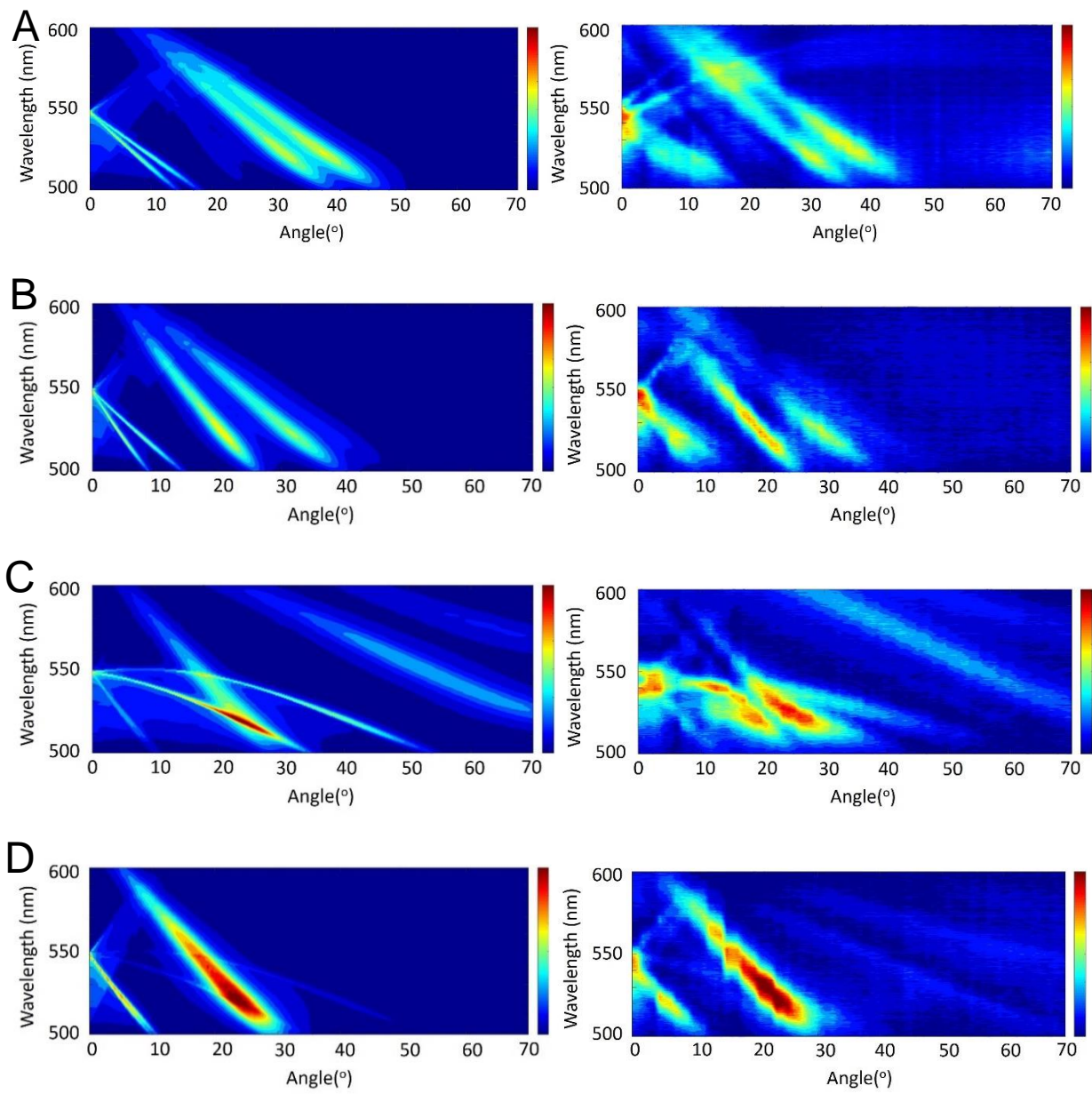


Figure 3-4. A comparison between simulated and measured data. The left four figures show the simulated data and the right four figures show the measured data. The four set of data are from two detection angles ϕ and two polarization directions. A) $\phi = 175^\circ$, S polarized. B) $\phi = 175^\circ$, P polarized. C) $\phi = 155^\circ$, S polarized. D) $\phi = 155^\circ$, P polarized.

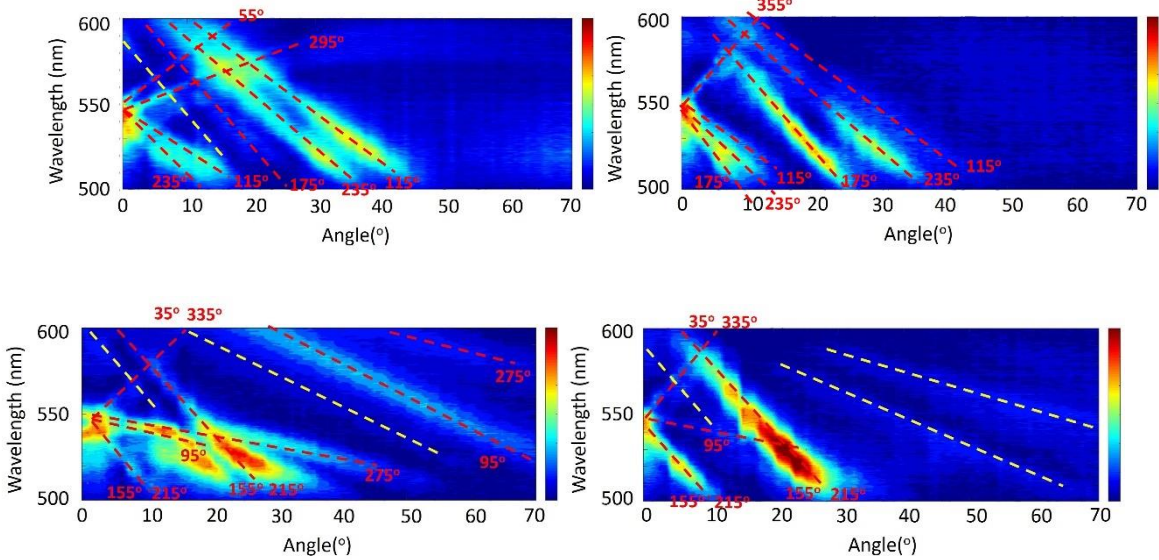


Figure 3-5. Dashed lines highlighting the features with the associated reception angles. Dashed lines in red show scattered TMWG and SPP modes, which are simulated. Dashed lines in yellow show scattered TEWG mode, which is not included in the simulation. The reason is explained previously.

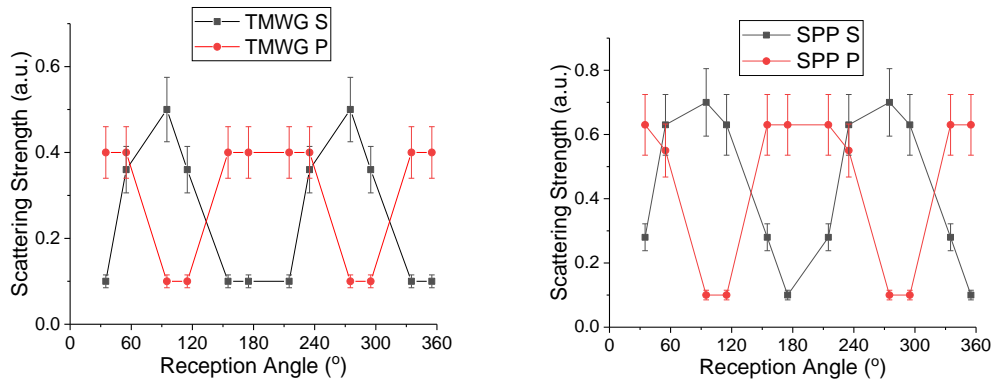


Figure 3-6. Plots of scattering strength of TMWG and SPP modes as a function of reception angle and polarization.

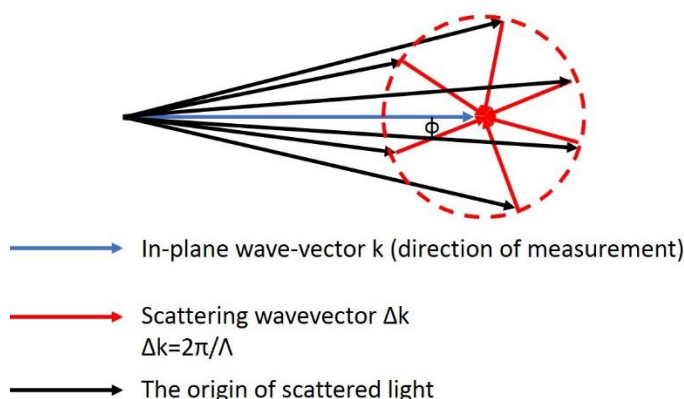


Figure 3-7. A schematic depicting Bragg diffraction equation with random scattering directions.

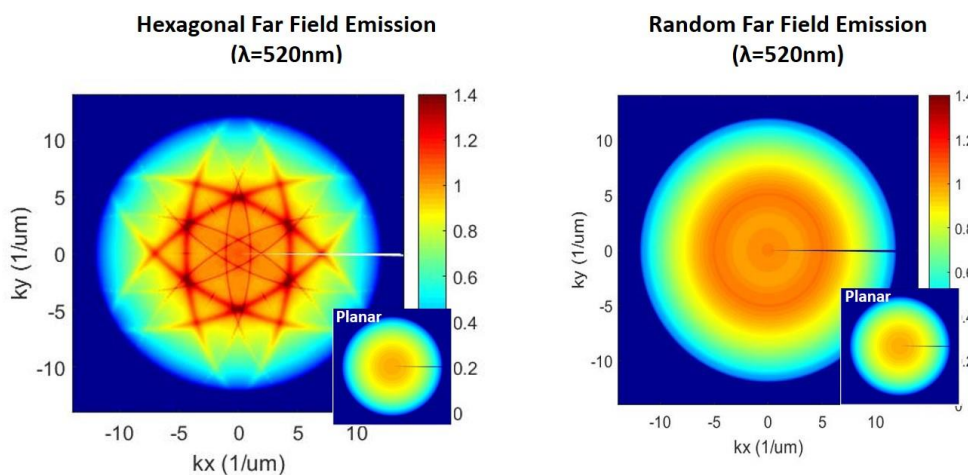


Figure 3-8. A comparison of far field emission pattern at 520 nm between 'single-crystal' structure and 'poly-crystal' structure.

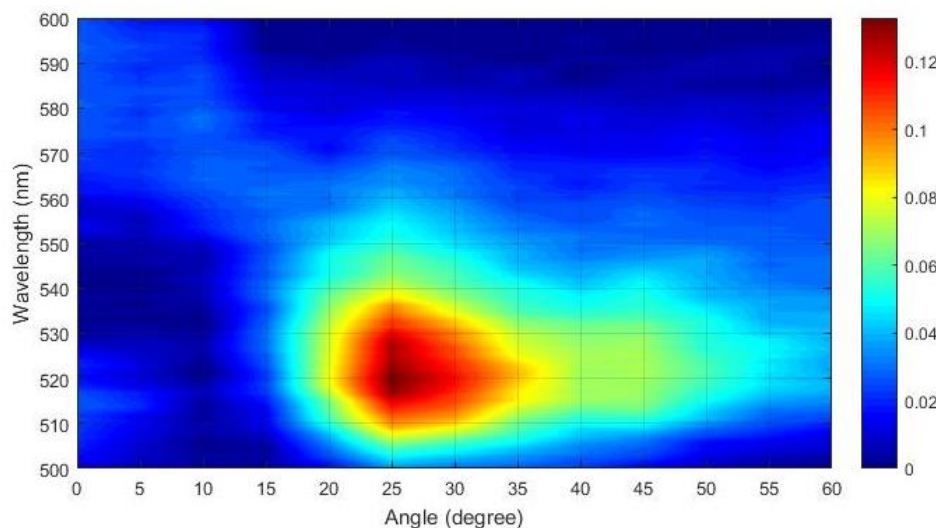


Figure 3-9. The measured angle resolved spectra data with the baseline subtracted.

CHAPTER 4
OPTICAL SIMULATION OF CORRUGATED OLEDs BY FDTD AND THE COMBINED
EFFECTS OF OPTICAL AND ELECTRICAL PERSPECTIVES

Introduction

In last chapter, a detailed methodology based on Bragg diffraction equation is described to evaluate the angle of the features and the scattering efficiency of each mode by the corrugated structure based on OLED angle-resolved spectra measurement. However, the simulation based on Bragg diffraction equation itself cannot predict the scattering strength without the comparison with the measured data. This makes this optical simulation totally useless without real experimental data when the extraction efficiency comparison is needed to pick one corrugated structure over another one. The reason behind this is the limitation of Bragg diffraction equation. To overcome this limitation, finite-difference time-domain (FDTD) method is used to numerically solve Maxwell's equations. With this method, scattering structures can be treated in more details than merely its spatial periodicity. We do not any longer use terms such as 'hexagonal' to label structures. We can differentiate the structures by the geometric shape of the repeating unit.

FDTD has long been used to simulate the optics of OLEDs. By simply placing an oscillating dipole source in the optical cavity, the light extraction can be simulated in a natural way by monitoring the electric field outside the optical cavity. However, things get complicated when it comes to corrugated structures rather than planar structures, especially when the change of light extraction is needed quantitatively from planar structures to corrugated structures. This is complicated because the extraction is different for dipoles at different locations in the corrugated optical cavity, while it is location independent in a planar optical cavity due to the continuous in-plane

translational symmetry. Then multiple simulations need to be done with various dipole locations. Multiple dipoles cannot be put in a single run of simulation because there will be non-physical interference among dipoles. A different approach will be described in order to study the extraction of each mode based on reciprocity theorem of light. The in-coupling efficiency into the cavity from a far-field dipole source with different incident angles will be modeled. This problem is equivalent to the out-coupling efficiency from the cavity to different emission angles. The advantage of the calculation of in-coupled light field is that the distribution of in-coupled light field is directly related to where the dipole can have a higher out-coupling efficiency. This distribution of in-coupled light field can also be directly compared with the in-homogenous static state electric field when a bias is applied across the two electrodes.

As mentioned in the last chapter, corrugated structures can introduce non-uniform static electric field between two electrodes when a bias is applied. This introduces a non-uniform distribution of electric current as well as exciton generation across the device pixel area. Therefore, to achieve the optimum device efficiency, we want the dipole source in the high current region to also have a high light extraction efficiency. This coupled effect between electrical and optical perspective is seldom reported. Most of the simulation work only focuses on the optical effect. However, it will be shown that the electrical effect is playing a significant role in the extraction efficiency of each mode.

In this chapter, the first section will describe the optical simulation theory based on reciprocity theorem. The second section will compare the extraction efficiency of TMWG of two different structures with dome shape and square shape structures. The

third section will compare the extraction efficiency of TMWG of two different structures with dome shape and hole shape structures.

Optical Simulation by FDTD using Reciprocity Theorem

The reciprocity theorem is used in the FDTD simulation presented in this chapter. It is depicted in Figure 4-1.⁵²⁻⁵⁴

Based on Bragg diffraction equation, the out-coupled light field as a function of angle from a corrugated OLED has peaks at angles where resonance happens. Therefore, the in-coupled light field intensity as a function of incident angle of light has peaks at those angles. Here the far-field dipole source can be treated as a plane wave source. If the incident angles are swept, peaks should be found as the intensity of the in-coupled light changes. The polarization of the incident light can also be controlled to see the in-coupling of different modes. In this chapter, the in-coupling of TMWG will be investigated by simulation, so the incident plane wave will be p polarized. Meanwhile, a simplified one-dimensional grating structure will be used to describe the problem and our capability to address the problem. In this way, the scattering wave vector will be parallel with the original wave vector as defined in the last chapter. Two pairs of different structures are compared.

Comparison between ‘Dome’ and ‘Square’ Structures

The structures in this section are shown in Figure 4-2.

In the two structures, both have a period of 400 nm in the x direction (horizontal). Only one period is shown in the figure. The height of the structure is 50 nm and the width is 200 nm. Both structures have continuous translational symmetry in the y direction (perpendicular to the screen). The left structure has a half elliptic cylinder ‘dome’ shape feature and the right structure has a rectangular ‘square’ shape feature.

From top to bottom, the materials are glass ($n=1.5$), ITO ($n=2$), organic materials ($n=1.75$), aluminum (built-in n and k values from literature). The simulation background is set to be glass with $n=1.5$. The thickness of ITO is 100 nm, the thickness of organic materials is 135 nm. All the simulations are done with one single wavelength (520 nm).

Based on Setfos simulation, in the planar OLED structure, the in-plane wavevector of the TMWG peak is $19 \mu\text{m}^{-1}$. Given the scattering wave vector $\Delta k = \frac{2\pi}{d} = 15.7 \mu\text{m}^{-1}$, after parallel scattering, the final in-plane wave vector is $3.3 \mu\text{m}^{-1}$, which corresponds to $\theta = \arcsin(3.3 / (\frac{2\pi}{0.52} * 1.5)) = 10.5^\circ$ in glass. This indicates that if the incident angle of the p polarized plane wave source is swept and the in-coupled light field is monitored, there should be a peak around 10.5° . A cross-sectional monitor is placed at $y=0$ to monitor the field.

The light field in a planar cavity can be fully calculated using transfer matrix methods. At such a small incident angle 10.5° in glass, the p polarized incident light is hardly in-coupled to the z component of the light field in the planar cavity. Therefore, the in-coupled E_z intensity is used to quantify the in-coupling efficiency of TMWG. In Figure 4-3, the in-coupled E_z is shown for the two ‘dome’ shape and ‘square’ structures.

The plots show the distribution of the z component of the light field at the peak incident angles. The incident angles where the peak intensity is different for the two structures and they are both different from the angle 10.5° calculated by Bragg diffraction equation. This implies that the real peak’s wavevector can deviate slightly from the angle calculated by Bragg diffraction equation depending on the detailed corrugated geometric structure.

In the red region, the in-coupled light field is stronger, implying that the dipole put in this region couple more with far-field dipole source. In the opposite way, the dipole put in the red region has a higher extraction efficiency of TMWG. However, in a real device, dipoles, which are basically radiating excitons, can only be generated in the emitting layer. The emitting layer is usually put near the middle of the organic layers and is around 20 nm thick. Assuming in thermal evaporation, all the layers deposited follow the morphology of the substrate, the emitting layer is also corrugated as highlighted in Figure 4-4.

It can be seen that within the range of the emitting layer, the distribution of in-coupled light field z component is non-uniform. This implies that the light extraction efficiency of TMWG strongly depends on where the light is generated within the emitting layer. To evaluate the light extraction efficiency, the intensity within the emitting layer should be integrated. We also performed the in-coupling simulation with different incident angles. In Figure 4-5, the integrated intensity is plotted as a function of angles in air for the two structures. For a better comparison, the in-coupled intensity integrated over the EML in a planar cavity is also plotted.

As expected, the intensity of the z component of the light field in-coupled to the planar cavity is negligibly small. Two factors contribute to this. One is previously mentioned. The p polarized incident light itself does not have a significant z component, based on simple diffraction, reflection and interference theory, the amount of z component light field in the planar cavity should be small. The other factor is that even the small amount of in-coupled z component light field is not uniform across the depth of the active layer and has its minimum where the EML is. According to the plots, the peak

intensities of the two corrugated structures are almost the same around 150 (a.u.) and as mentioned before, the peaks appear at different angles. A further integration can be done over all the angle in the shown range, though this range might not cover the entire features. The ratio between the two structures is 1:1.17 (Dome: Square), implying a higher coupling efficiency of the square structure compared with the dome structure. However, this optical coupling efficiency does not suffice to address the entire problem. Electrical properties of the corrugated cavity need to be considered. Under electrical injection, if excitons are generated in the red region in the plots, the generated light will have a higher extraction efficiency, while if excitons are generated in the blue region in the plots, the generated light will have a lower extraction efficiency. The distribution of excitons is directly related to the distribution of current density and hence the distribution of electric field.

Without the corrugated structures, an OLED structure can be simplified to a parallel-plate capacitor. Under static voltage bias on the two opposite electrodes, the static electric field in the cavity is uniform across the pixel. With the corrugated structures, under static voltage bias on the two opposite electrodes, the static electric field in the corrugated cavity is not uniform anymore and can be modeled using finite difference methods to solve Poisson's equation without any charges in the cavity.

As described previously, the distribution of exciton generation across the pixel is needed to consider its combined effect with the optical light extraction efficiency. Here the distribution of static electric field in the corrugated cavity will be used instead of the distribution of exciton generation as an approximation to demonstrate the effect of non-uniform exciton generation distribution. This simulation considering combined electrical

and optical effect will be a semi-quantitative estimation. In Figure 4-6 are the plots showing the distribution of the static electric field in the corrugated cavity with the two studied structures.

In the electrical simulation, the bias across the two corrugated plates are both set to be 4 volts. It can be clearly seen that the electric field is concentrated where the distance between two plates is smaller. This concentration of electric field is more pronounced in the square structured cavity due to its sharp edges. Though in the real device, the injected space charges and the field dependent mobility of organic semiconductor materials will make the real current density distribution deviate from the electric field distribution shown in the plots. This static electric field simulation can still help roughly estimate the distribution of current density across the pixel and hence the exciton generation distribution. This can give a semi-quantitative understanding of the combined optical and electrical effect of corrugated structure on light extraction efficiency of OLEDs.

One step ahead of simply integrating the E_z over the EML region and getting the plots. The static electric field in the EML region is added as a ‘weight’. The integrand is changed to be the product of E_z and the static electric field. The updated integrated intensity plots are shown in Figure 4-7.

The first thing that needs to be noted here is that the shape of both curves does not change. This means that the light intensities concentrated at the structure edges, which are amplified by the also concentrated static electric field, are indeed part of the in-coupled TMWG and have the featured in-plane wavevector. Again, an integration over incident angle can be done and this time the ratio between dome and square

becomes 1:1.47. The difference is bigger than the one only considering the optical effect 1:1.17, thanks to the electrical effect.

Comparison between ‘Rod’ and ‘Hole’ Structures

In this section, another pair of structures are compared in conjunction with the experiment undergoing in our lab in the meantime. The dome structure in the last section will be referred as ‘rod’ and the other structure is a ‘flipped’ dome structure and will be referred as ‘hole’. These two terms are selected according to real two-dimensional structures in the experiment. The results of this section will be used to understand the experimental results. The two structures are shown in Figure 4-8.

In the two structures above, the only difference is that the geometric structure is inverted upside-down. The period is 400 nm, the feature height (or depth) is 50 nm and the feature width is 200 nm. The static electric field distribution will be inverted upside-down, which implies that the distribution of electric field intensity in the EML across the pixel will stay unchanged. In Figure 4-9, the in-coupled light intensity is shown at the angle where each structure has the peak intensity with the emitting layer highlighted in red.

Comparing the two structures above, we see that the strong concentration in the middle of the feature in the ‘rod’ structure does not appear in the ‘hole’ structure. Instead, there are two semi-symmetric strong concentrations on top of the feature in the ‘hole’ structure, which happen to be coinciding with the concentrated static electric field, implying that the electrical effect will be pronounced with the ‘hole’ structure despite the much weaker concentration of static electric field associated with the dome structure compared with the square structure. The plots of integrated intensity as a function of incident angles only considering the optical effect are shown first in Figure 4-10.

The integration over this range of incident angle can be done and the ratio Rod: Hole is 1:1.23. Considering the electrical effect, the plots of the ‘weighted’ intensity are shown in Figure 4-11.

In spite of the relatively weak static electric field concentration effect associated with the less sharp features in the dome shape structure, the electrical effect is still pronounced due to the coinciding light field and the static electric field distribution on top of the feature. After integration over the incident angle, the ratio between Rod and Hole is 1:1.38. The difference brought by taking the electrical effect into consideration is smaller compared with the square structure. However, the comparison between Rod and Hole structures is more interesting because in the experiment the two structures are fabricated by nano-imprinting using the same master mode. Their extraction behaviors are so much different in TMWG, but this difference cannot be predicted by Bragg diffraction equation.

Summary and Conclusions

Optical simulation using FDTD method is done to understand the light extraction effect of corrugated structure on OLEDs. Reciprocity theorem is used to study the coupling of TMWG mode. Two pairs of corrugated structures are compared. Electrical effect brought by non-uniform static electric field is taken into consideration. The combined optical and electrical effect on the light extraction is evaluated. Based on our calculation, the ‘Rod’ structure is less efficient than the ‘Square’ and the ‘Hole’ structures to extract TMWG. The efficiency difference can be significantly amplified (~2x) by the electrical effect.

$$\text{Out-coupling of in-cavity dipole} \quad \overleftarrow{E_1} \cdot \overrightarrow{P_2} = \overrightarrow{E_2} \cdot \overrightarrow{P_1} \quad \text{In-coupling of plane wave from far field}$$

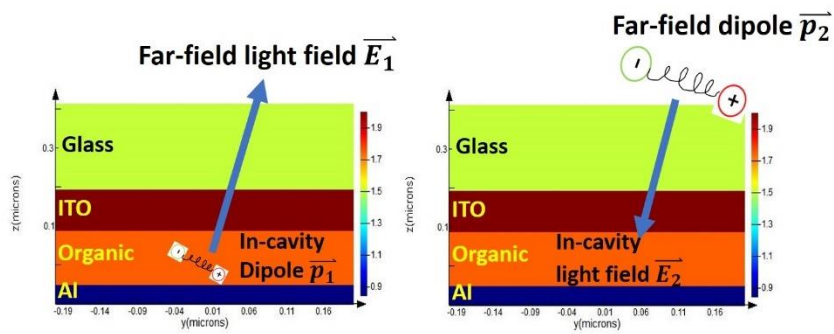


Figure 4-1. The out-coupling problem towards a certain emission angle of an in-cavity dipole is equivalent to the in-coupling problem of a far-field dipole from that direction into the cavity.

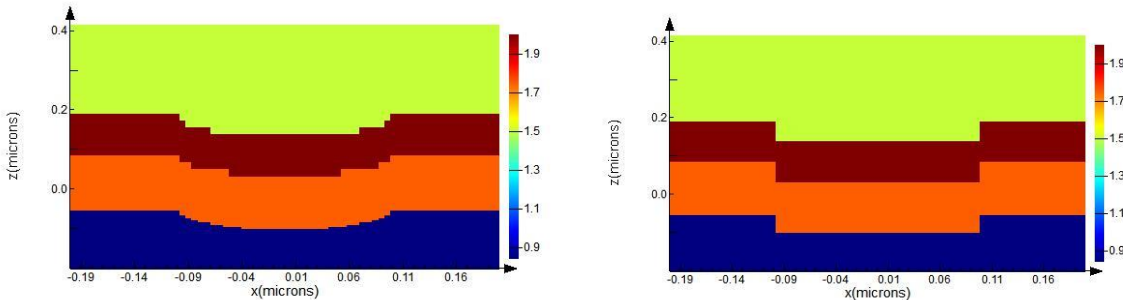


Figure 4-2. The refractive index contour of two grating structures.

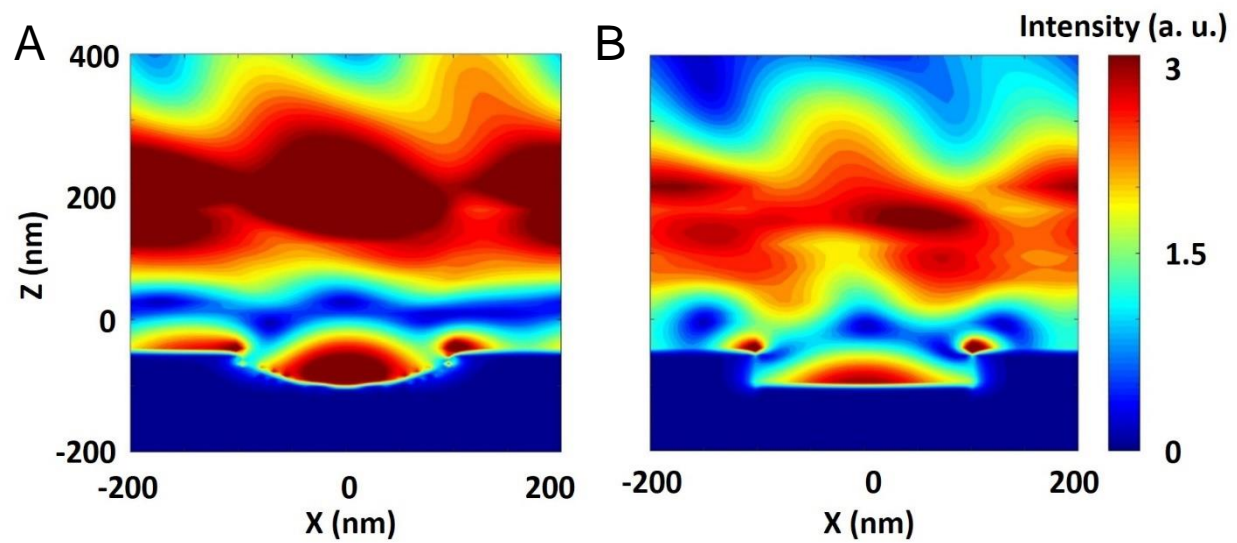


Figure 4-3. The z component of the light field. A) At 9.8° incident angle for ‘dome’ structure. B) At 11.95° incident angle for ‘square’ structure.

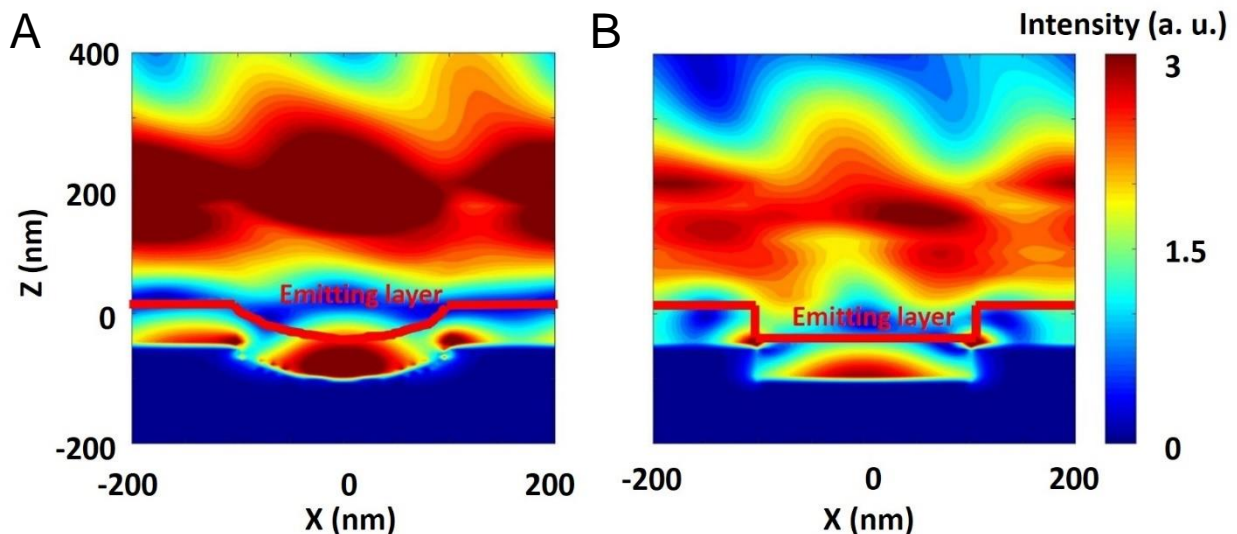


Figure 4-4. The z component of the light field with the emitting layer highlighted in red. A) At 9.8° incident angle for ‘dome’ structure. B) At 11.95° incident angle for ‘square’ structure.

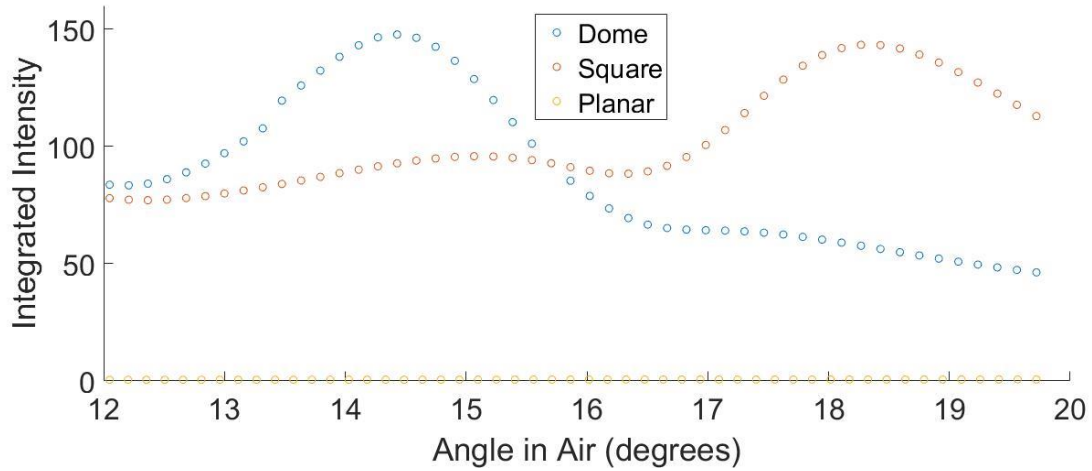


Figure 4-5. Plots showing the integrated E_z over the EML as a function of incident angles for two structures.

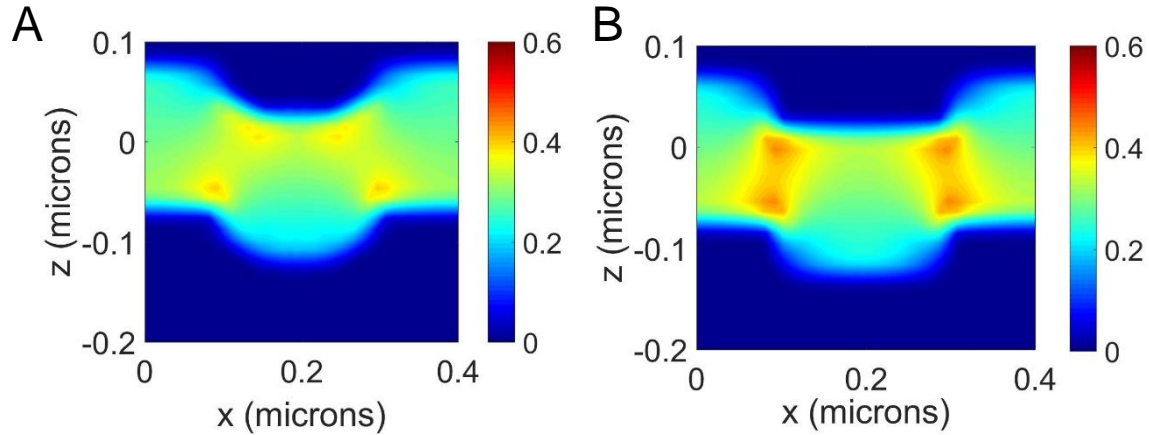


Figure 4-6. Plots showing the static electric field intensity distribution inside the cavity with two structures. A) Dome. B) square.

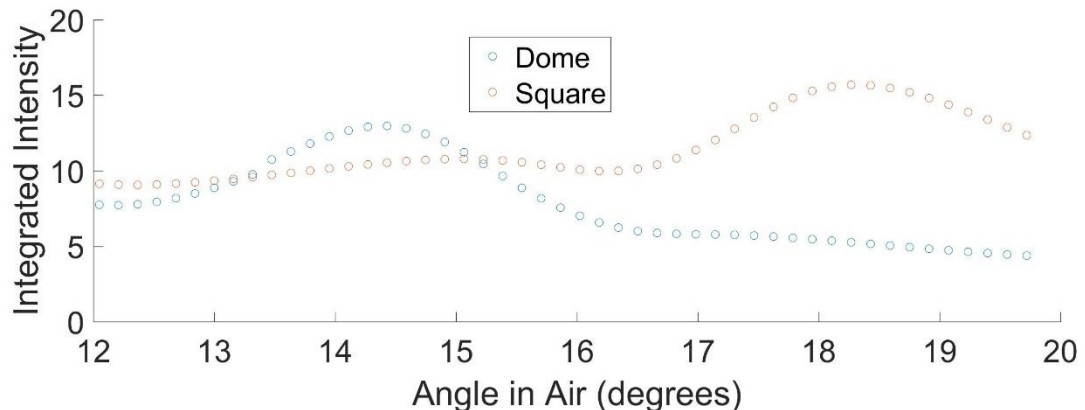


Figure 4-7. Plots showing the integrated E_z over the EML weighted by the static electric field as a function of incident angles for two structures.

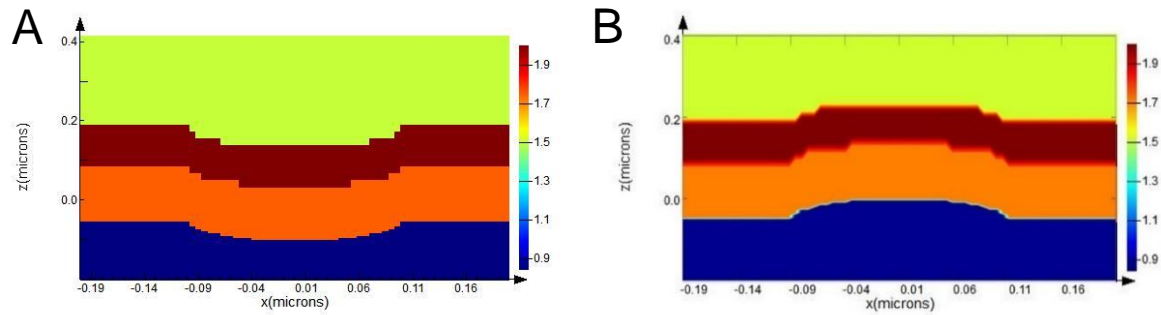


Figure 4-8. The refractive index map of the two structures. A) 'Rod'. B) 'Hole'.

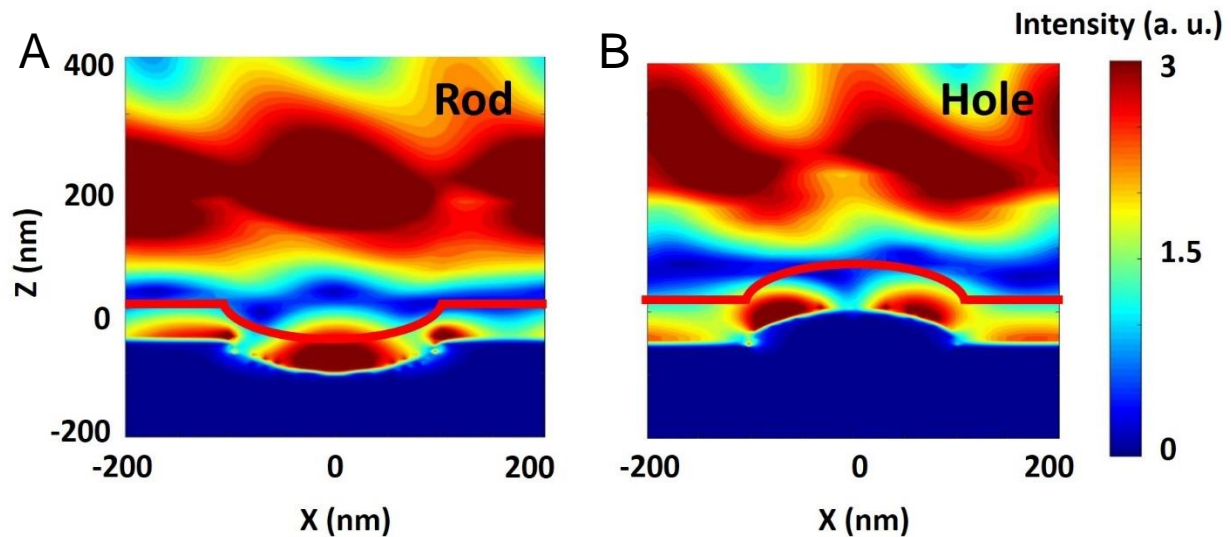


Figure 4-9. The z component of the light field with the emitting layer highlighted in red. A) At 9.8° incident angle for 'rod' structure. B) At 8.93° incident angle for 'hole' structure.

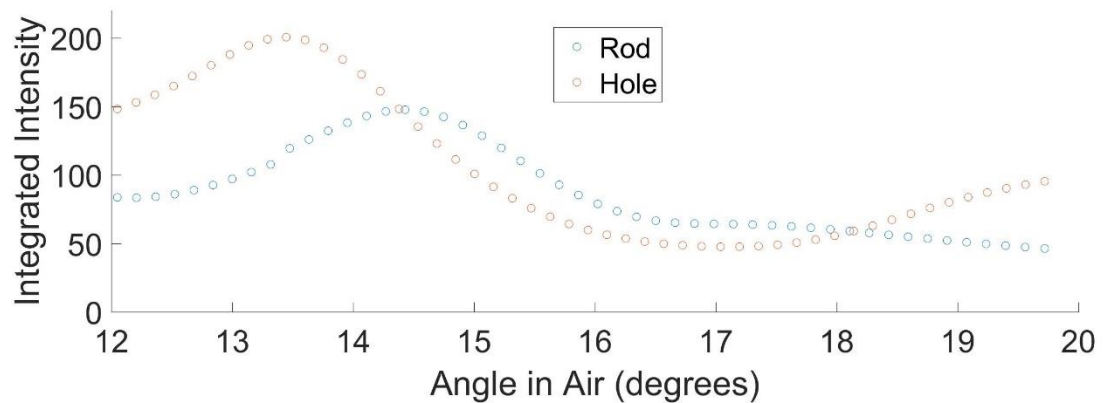


Figure 4-10. Plots showing the integrated E_z over the EML as a function of incident angles for two structures.

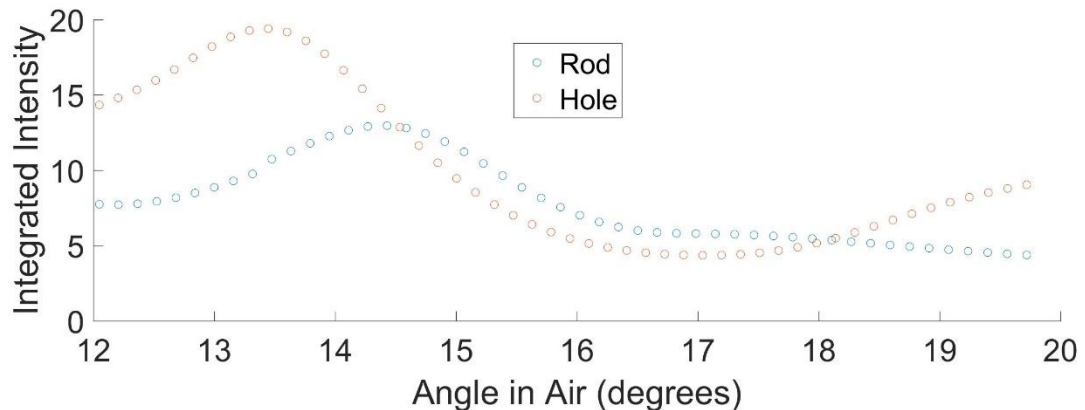


Figure 4-11. Plots showing the integrated E_z over the EML weighted by the static electric field as a function of incident angles for two structures.

CHAPTER 5

PHOTOLUMINESCENCE AND ELECTROLUMINESCENCE DEGRADATION ANALYSIS IN ORGANIC LIGHT EMITTING DIODES

Introduction

The invention of phosphorescent and TADF materials have improved the IQE of OLEDs to near 100%. By designing the molecules, researchers have realized emitters with red, green and blue light.^{43, 55-59} With different light extraction technologies, the EQE can be improved to as high as 80%. However, the operational stability of OLEDs remains to be an issue that limits the practical use in displays and lighting application. Particularly, there are no TADF or phosphorescent blue OLEDs meeting the requirement of operational stability for commercial use.^{60, 61} Thus, investigations on the degradation mechanism is still of great interest and importance.

It is well accepted that the OLED operational stability strongly relies on the control of emission zone.^{57, 61-64} In the case of electroluminescence, not all the emitters in the entire EML contribute to the emission. The distribution profile of excitons in the EML determines the local exciton density, which is directly related to the reaction rate of TTA and TPQ. The high-energy reaction products of TTA and TPQ are believed to be contributing to the intrinsic degradation of OLED materials.⁶⁵⁻⁶⁷

However, it is usually challenging to determine the emission profile in the OLED. A commonly used approach is to insert a thin sensing layer in the EML.^{62, 64} The thin sensing layer usually contains dyes with a lower energy emission. By analyzing the additional lower energy peak in the emission spectrum of the OLEDs with the sensing layer, researchers are able to estimate the local exciton density. By inserting the sensing layer at different locations, the exciton profile can be measured. This method assumes that the thin sensing layer has little effect on the transport properties of the

EML. This assumption is sometimes questionable as the dyes with a lower emission energy are often charge traps.

In this chapter, a new and simple methodology will be introduced to quantitatively probe the emission zone of OLEDs by comparing the PL degradation of OLEDs with the EL degradation during continuous electrical operation. This methodology measures the emission zone on the original working device in a single run of stability test without adding additional layers in the device structure. This approach is first validated by investigating the emitter concentration effect on the stability of OLEDs using the well-known TADF emitter (4s,6s)-2,4,5,6-tetra(9H-carbazol-9-yl)isophthalonitrile (4CzIPN).^{5,68-71} The results are consistent with the results reported in the literature. We then applied this approach to investigate the emitter concentration effect on the stability of OLEDs using another TADF emitter 4-carbazolyl-2-methylisoindole-1,3-dione (Dopant 1). Based on our results, the Dopant 1 OLEDs show much less pronounced emitter concentration effect due to the relatively worse electron transport in the EML, compared with 4CzIPN OLEDs. We were able to widen the emission zone by the use of a mixed host. The effect was confirmed by using the new methodology.

Characterization of Degradation

The stability test was done by driving the OLEDs at a constant current density. In this chapter, all the devices were electrically stressed at 25 mA/cm². The EL spectrum was recorded as a function of time. A key measurement of this study is the PL degradation during the electrical stress. PL spectrum from the OLED was measured at various time intervals by temporarily turning off the electrical bias and exciting the OLED with a continuous monochromatic light source with the emission wavelength 405 nm. Note that the PL degradation measurement in this study is different from the UV

degradation, in which the PL was measured when the device is stressed by UV light. In this study, the degradation of the device is only from the electrical current. The exposure to near UV 405 nm light is so little that it has negligible effect on the device. This is confirmed in the experiment when the EL intensity after every PL measurement was observed to be consistent with the one before the PL measurement. Figure 5-1 shows the experimental setup. The UV source beam was split by a beam splitter. A photodiode was used to monitor the intensity of the UV source to make sure the light source has stable intensity in every PL measurement.

Theoretical Model

To probe the emission zone based the PL degradation measurement, we need to know how the emission zone affects the OLED PL degradation. The control of the emission zone is important and interesting because in a lot of situations, the device stack does not have a balanced charge transport and the emission zone does not cover the entire EML. Considering a structure with a hole (electron) dominant EML and a HBL (EBL) with a high HOMO (LUMO) barrier to confine holes (electrons) in the EML, the charges and excitons tend to concentrate in a narrow emission zone near the EML/HBL (EML/EBL) interface under electrical bias. Degradation reactions such as TTA and TPQ have a higher rate in the emission zone. Therefore, degradation produces such as molecular fragments also have a higher concentration in the emission zone near the interface, further facilitating the EL degradation. On the contrary, in the PL measurement, the in-coupled excitation light generates excitons uniformly in the relatively thin EML (~20 nm), which can be easily seen in the simulation using the transfer matrix method. The entire EML contributes to the PL. The interface-concentrated degradation impacts on the PL significantly less than it does on the EL.

This results in a generally slower PL degradation than the EL degradation during the electrical stress, as shown in Figure 5-1. This phenomenon has been reported in the literature, too. For a device with a very balanced charge, the emission zone more uniformly covers the entire EML with the degradation products uniformly distributed. The difference between the PL and EL degradation rates would be less pronounced. Therefore, by comparing with the EL degradation, the PL degradation data can be used to probe the emission zone under the electrical bias.

Emitter Concentration Effect on Stability of 4CzIPN OLEDs

To better confirm the model in experiments. A series of OLEDs were fabricated using the well-known TADF emitter (4s,6s)-2,4,5,6-tetra(9H-carbazol-9-yl)isophthalonitrile (4CzIPN). In the OLEDs, a hole dominant material, 3,3-di(9H-carbazol-9-yl)biphenyl (mCBP) was used as the host and 2,4,6-tris(biphenyl-3-yl)-1,3,5-triazine (T2T) was used as the HBL. This combination of mCBP:4CzIPN/T2T used in OLEDs has been extensively investigated in the literature and it has been found that with an emitter concentration of 10% in volume in the EML, the EML is hole dominant with the emission zone concentrated near the interface with T2T.^{63, 68, 69, 72} The emitter material 4CzIPN is deep electron traps in the EML due to its LUMO offset with the host mCBP greater than 1 eV. However, with a higher emitter concentration, researchers have found that the trap assisted transport of electrons is enhanced so that the emission is widened with an improved device stability as expected. As the emitter concentration largely affects the emission zone in this type of devices, it is interesting to investigate the emitter concentration effect on device stability using our model based on the PL degradation measurement.

OLEDs with three different emitter concentrations were fabricated, 10%, 20% and 30% volume ratios. 1,4,5,8,9,11-Hexaaazatriphenylenehexacarbonitrile(HAT-CN) was used as the HIL. N,N' -Bis(naphthalen-1-yl)-N,N' -bis(phenyl)benzidine(NPB) and Tris(4-carbazoyl-9-ylphenyl)amine (TcTa) were used as the bilayer HTL. 2,9-Bis(naphthalen-2-yl)-4,7-diphenyl-1,10-phenanthroline (NBphen) was used as the ETL. 8-Hydroxyquinolinolato-lithium (Liq) was used as the EIL and aluminum was used as the top reflective cathode. The layer thicknesses and the energy diagram are shown in Figure 5-2.^{69, 73-75} Also shown are the normalized PL and EL degradation at the current density of 25 mA/cm².

As expected with our model, the device with a higher emitter concentration shows less difference in the PL and EL degradation rates due to a wider emission zone, which also results in a better stability, consistent with the results reported in the literature. One thing worth attention here is that the PL and EL degradation almost have the same degradation rates for the 30% emitter concentration OLED. This confirms that factors other than the quenching due to degradation products such as a changed charge balance play a negligible role in the degradation in this type of OLEDs and that the quenching affects the PL and EL similarly. This finding is consistent with a previous report by Sandanayaka, et al.⁷² They also had conclusions that in the OLEDs with the mCBP:4CzIPN/T2T combination, the EL degradation is primarily due to the formation of quenching sites instead of the changed charge balance.

The emission zone length can be extracted from the measured PL and EL data mathematically. Previously, mathematical models extracting information about emission zone have been discussed based on the transient PL data.⁶⁵ In this chapter, a

mathematical model based on the simpler PL data will be discussed. There are a few assumptions made before the model is presented. First, the excitons generated in the EL case have an exponential profile distribution with the maximum at the EML/HBL interface. This assumption is a widely used assumption and is consistent with the measured results using the sensing layer method in the mCBP:4CzIPN/T2T based OLEDs.⁶³ Second, the degradation reaction rate is proportional to the concentration of excitons. Third, the degradation products quench the excitons in the same way regardless of whether they are photo-excited or electrically excited.

We first write the rate equation of excitons with the concentration $N(x, t)$,

$$G(x) = \frac{1}{\tau} \cdot N(x, t) + K_Q \cdot Q(x, t) \cdot N(x, t) \quad (5-1)$$

Where $G(x)$ is the exciton generation rate with an exponential spatial profile. Thus,

$$G(x) = G(x = 0) \cdot \exp(-\frac{x}{L}) \quad (5-2)$$

where L denotes the effective emission zone length, x denotes the distance from the concentration maximum, i.e. the EML/HBL interface, τ is the exciton lifetime, and $Q(x, t)$ is the quenching site concentration with a generating rate constant K_Q . The rate equation of the quenching site is

$$\frac{\partial Q(x, t)}{\partial t} = K_G \cdot N(x, t) \quad (5-3)$$

The quenching site generation rate is proportional to the exciton concentration by the rate constant K_G . In a fresh, pre-stress device, $Q(x, 0) = 0$. The EL and PL intensity normalized to the initial intensity can be expressed by the concentration of excitons and quenching site as,

$$\text{Normalized EL} = \left[\int_0^W dx \cdot N(x, t) \right] / \left[\int_0^W dx \cdot N(x, 0) \right] \quad (5-4)$$

$$Normalized PL = \left[\int_0^W dx \cdot \frac{1}{1+K_Q \cdot Q(x,t) \cdot \tau} \right] / W \quad (5-5)$$

Where W in the integration limits is the thickness of the EML, which is 20 nm in all the OLEDs in this chapter. The distribution of photo-generated exciton is assumed to have a uniform distribution confirmed by the transfer matrix method, in which the results show the deviation from a uniform distribution is less than 10%. We then can use the two equations of normalized PL and EL intensity to fit the measured data. The effective emission zone length L and the product of the two rate constants K_Q and K_G are used as the fitting parameter. In this model, we cannot determine whether the generation or quenching site or the quenching effect on the excitons is playing a more important role. The exciton lifetime for 4CzIPN is 3.7 μ s from the literature.⁵ As shown in Figure 5-3, the model and the measured data fit well. The extracted effective emission zone length is 4.5 ± 0.4 nm, 7 ± 1 nm and 16 ± 9 nm for the 10% emitter device, the 20% emitter device and the 30% emitter device, respectively.

The effective emission zone length measures the distance from the interface where the concentration drops to about 37%. It determines how fast the concentration decreases away from the interface, so it is not limited by the thickness of the EML. An effective emission zone length larger than the thickness of the EML indicates the distribution is close to uniform. Our results of the effective emission zone length are also consistent with the measured values in the literature by using the sensing layer method. Song et al. found it to be around 8 nm and longer than 18 nm for the 10% emitter device and the 30% emitter device, respectively.⁶³

Emitter Concentration Effect on Stability of Dopant 1 OLEDs

Having modeled the PL degradation data of 4CzIPN OLEDs successfully, we investigated the emitter concentration effect on device stability using another TADF emitter Dopant 1. The OLEDs containing Dopant 1 had exactly the same structure with the 4CzIPN OLEDs for a better comparison. The device structure and the energy diagram are shown in Figure 5-4. Similar to 4CzIPN, Dopant 1 has a LUMO offset with mCBP greater than 1 eV, making it deep electron traps in the EML too. We might expect a similar emitter concentration effect on the device stability by affecting the emission zone length.

three types of devices were fabricated with three different emitter volume ratios: 10%, 20% and 30% and the degradation of PL and EL was measured with a constant 25 mA/cm² current density. The exciton lifetime was 6.8 μ s measured by transient PL measurements. The measured data were fitted and the results are shown in Figure 5-5.

The effective emission zone length was extracted from the fitting. It is 3.3±0.2 nm, 3.0±0.1 nm and 3.5±0.1 nm for the 10%, 20% and 30% device, respectively. Unlike the 4CzIPN OLEDs, the widening of the emission zone was not realized by a higher emitter concentration. Since the widening of the emission zone at the higher emitter concentration of 4CzIPN is due to the enhanced electron transport of the EML, this different trend of Dopant 1 devices indicates that the Dopant 1 emitter does not facilitate the electron transport even the concentration is as high as 30%. The device drive voltages of the OLEDs with the two emitters were compared and the results confirm the relatively poor electron transport of the EML of Dopant 1 OLEDs. The drive voltages at 1 cd/m², which is the luminance turn-on voltage, and at 1 mA/cm², which is the diode current turn-on voltage of the devices with the two emitters and three different emitter

concentrations are summarized in Figure 5-6. It can be seen that the Dopant 1 OLEDs generally have a higher drive voltage compared with the 4CzIPN OLEDs and that the Dopant 1 OLEDs have a higher drive voltage with a higher emitter concentration while the 4CzIPN OLEDs have a lower drive voltage with a higher emitter concentration. These two facts both indicate the worse electron transport of the Dopant 1 emitter in the hole dominant mCBP host compared with 4CzIPN. The less efficient electron transport via Dopant 1 results in the narrow emission zone, limiting the device operational stability.

Mixed Host Effect on Dopant 1 OLEDs Stability

As the higher emitter concentration could not widen the emission zone and thus improve the device stability of Dopant 1 OLEDs, we sought to achieve this by using another widely studied approach changing the single material mCBP host into a co-host by mixing the HBL material T2T in the EML.⁴⁵ We also wanted to look into the interplay between the mixed host with the emitter concentration. Two sets of devices were fabricated. One set had a low emitter concentration of 6% and the other set had a high emitter concentration of 30%. In each set of devices, three types of devices were made. One control device was made using mCBP single host. The other two were made with a mixed host but with two different volume ratios of T2T in the EML, 10% and 20%. All the devices were stressed at the same 25 mA/cm² condition and the degradation of PL and EL was monitored and fitted with our model. The results are shown in Figure 5-7.

As shown by the data, a mixed host improved the device stability. But the improvement was more significant on devices with a low emitter concentration. As discussed previously, the Dopant 1 emitter acts as deep electron traps given the large LUMO offset with the host material mCBP and the electron transport via the trapping

sites is very inefficient even the emitter concentration is as higher as 30% volume ratio. Indeed, a high emitter concentration in this situation implies so many electron transport retarders that a moderate volume ratio 20% of T2T was not able to facilitate the electron transport. On the contrary, in the situation of a low emitter concentration, the lag in the electron transport is easily compensated by the adding of electron transport T2T. We also quantified the effect of using the mixed host in the situation of the low emitter concentration. It is shown that the effective emission zone length increased from 2.6 ± 0.1 nm in the control device to 6.5 ± 0.2 nm in the 20% T2T mixed host device.

The effect of widening the emission zone on the device stability can be simulated further using our model. We modeled the PL and EL degradation based on the measured data of a 10% volume ratio Dopant 1 single host device. The simulation data are shown in Figure 5-8. We show that if the effective emission zone length can be elongated by a factor of two from 3.1 nm to 6.2 nm, the LT80 (the time during which EL degrades by 20% of the initial luminance) at 25 mA/cm² can be improved by about 80%. This is consistent with the measured data by using a 20% T2T mixed host. Our simulation also indicates the limitation of lifetime improvement by emission zone widening. The improvement can only be as much as 100%. In order to further improve the device stability, other approaches need to be developed. The use of materials with better intrinsic stability can reduce the rate constants K_G of defect generation. The use of emitters with a shorter exciton lifetime can make the exciton less prone to quenching.

Summary and Conclusions

In this chapter, we introduce a simple and new approach to investigate the emission zone of OLEDs by doing comparison between the device EL and PL degradation under continuous electrical stress. Based on our model, a much slower PL

degradation than the EL degradation indicates a narrow emission zone, while a similar PL and EL degradation rate indicates a wide emission zone. This model was validated by investigating the emitter concentration effect on the device stability of OLEDs using the well-studied emitter 4CzIPN. We applied this methodology to study the emitter concentration effect on the device stability of OLEDs using a new emitter Dopant 1. Our results show that the inefficient electron transport of Dopant 1 OLED EML leads to a narrow emission zone, limiting the device stability. A mixed host is shown to be able to widen the emission zone and improve the device stability.

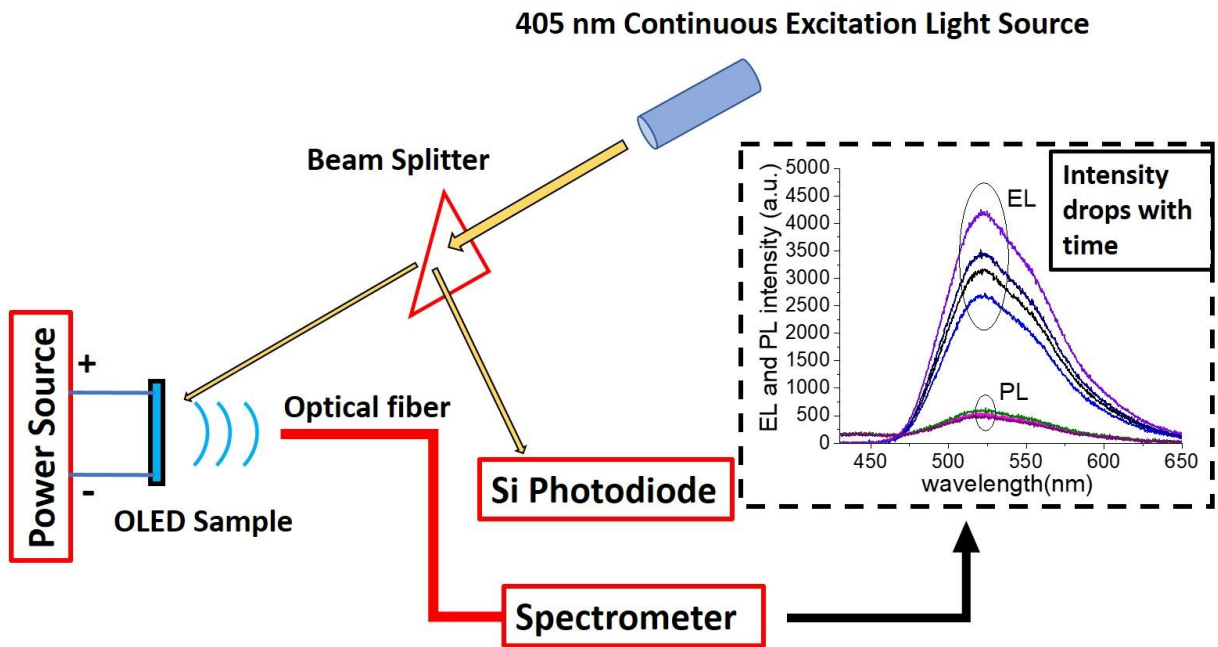


Figure 5-1. The measurement setup of PL measurement during a constant-current degradation test. Inset: A plot showing an example data set measured from a green OLED showing the degradation of both EL and PL.

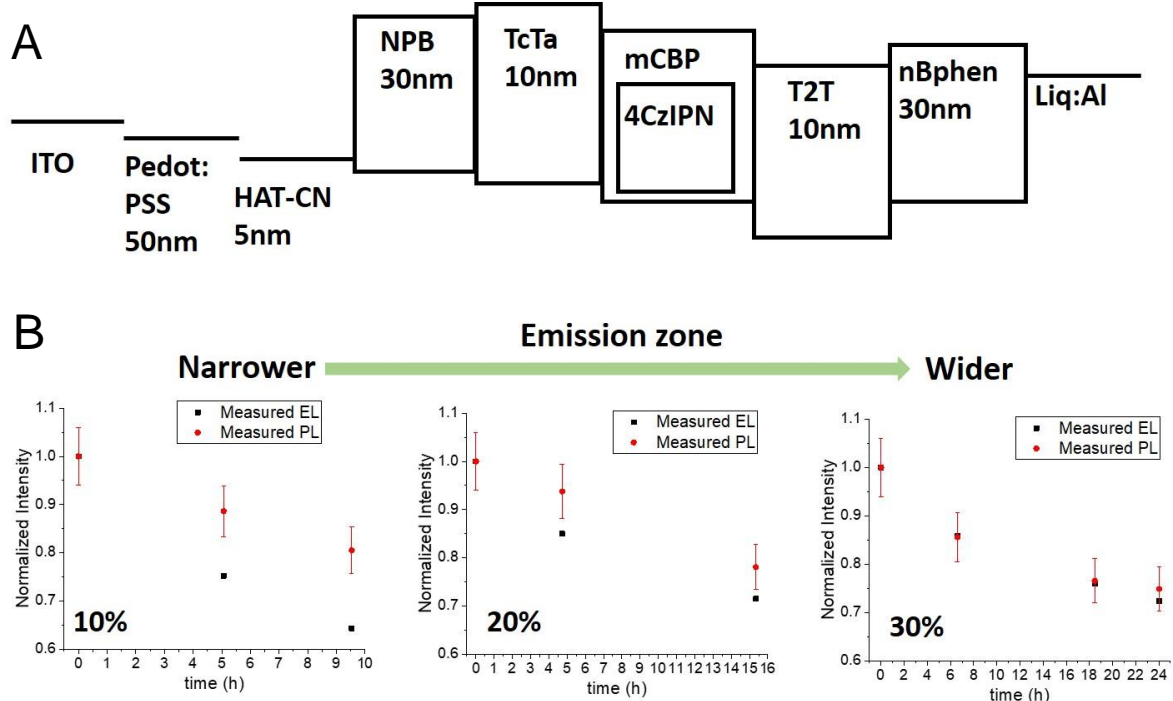


Figure 5-2. Emitter concentration effect of 4CzIPN OLEDs. A) Device structure and energy diagram of 4CzIPN devices. B) Normalized OLED EL and PL degradation. The thickness of emitting layer is 20 nm.

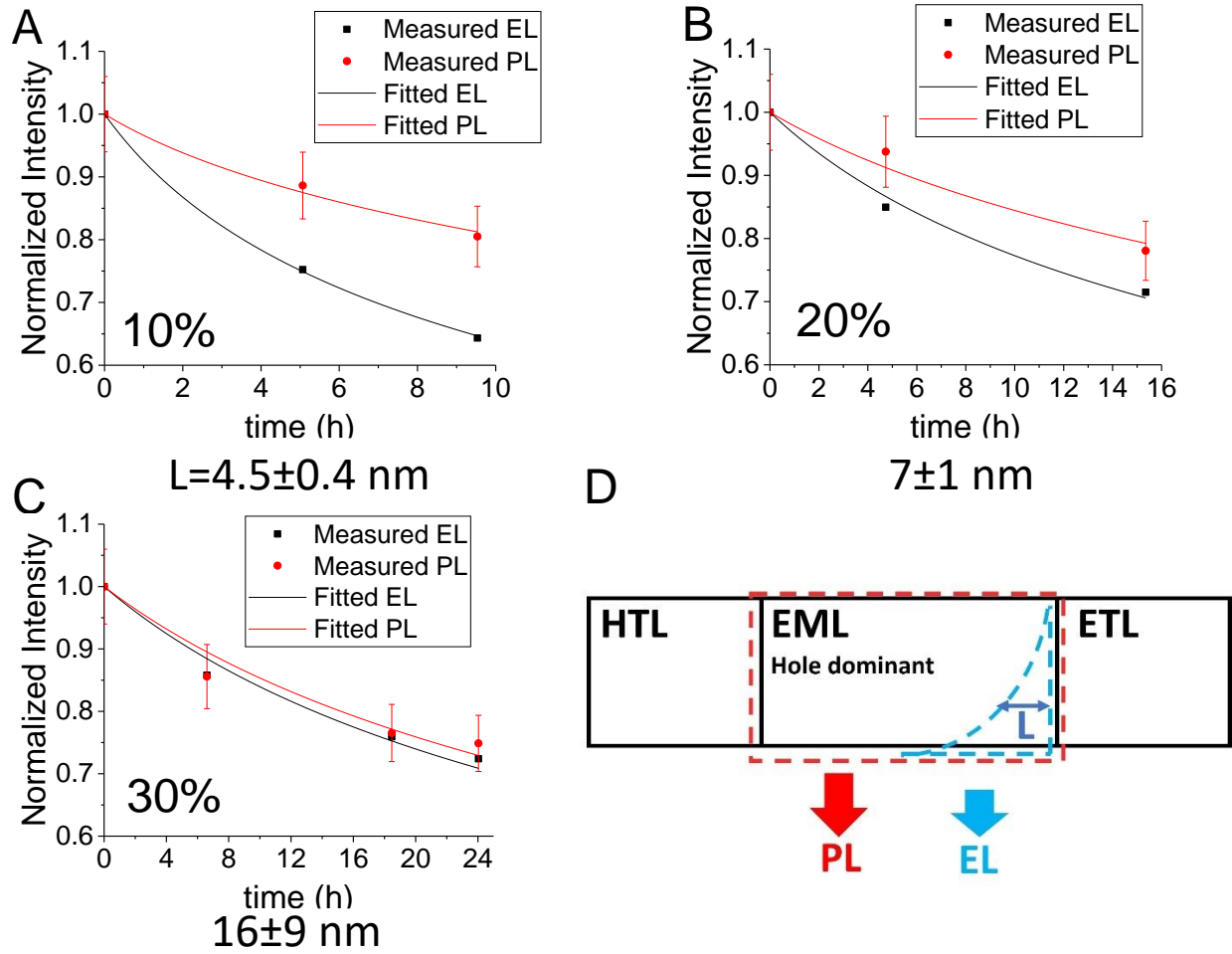
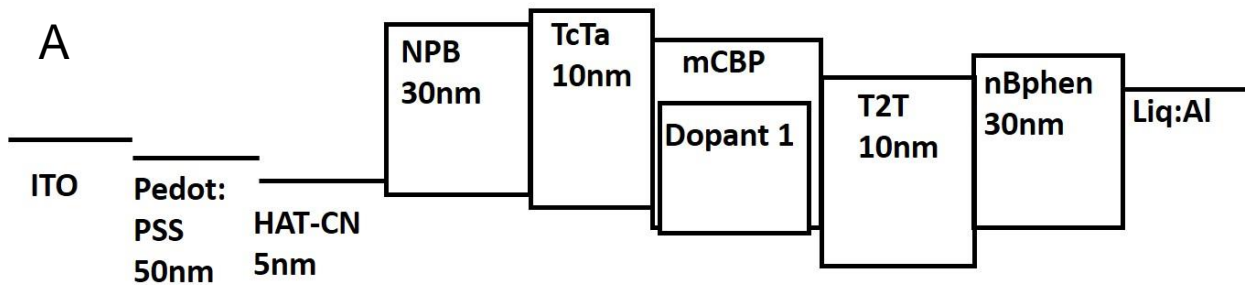
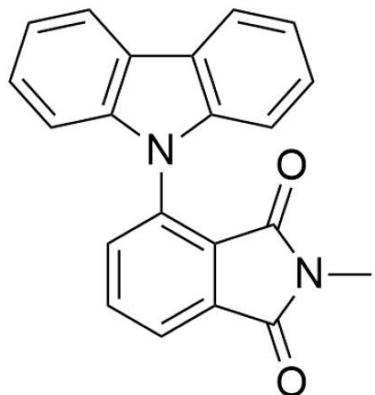


Figure 5-3. Measured and fitted EL and PL degradation of 4CzIPN devices with different emitter concentrations. A) 10%. B) 20%. C) 30%. D) A schematic showing the effective emission zone length.



B



Dopant 1

Figure 5-4. Dopant 1 OLED structure. A) Device structure and energy diagram of Dopant 1 devices. B) Molecular structure of Dopant 1. The thickness of the EML is 20 nm.

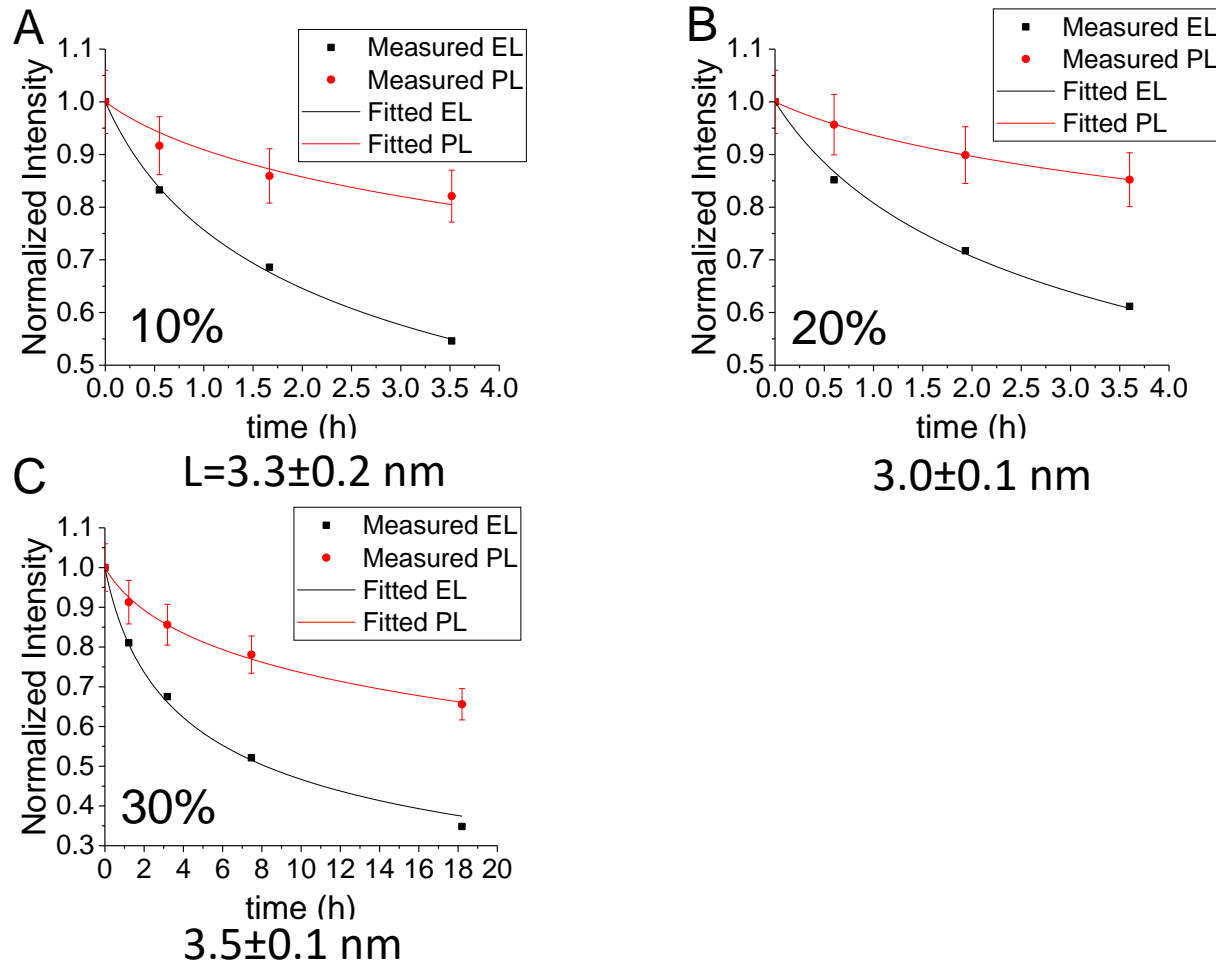


Figure 5-5. Measured and fitted EL and PL degradation of Dopant 1 devices with different emitter concentrations. A) 10%. B) 20%. C) 30%.

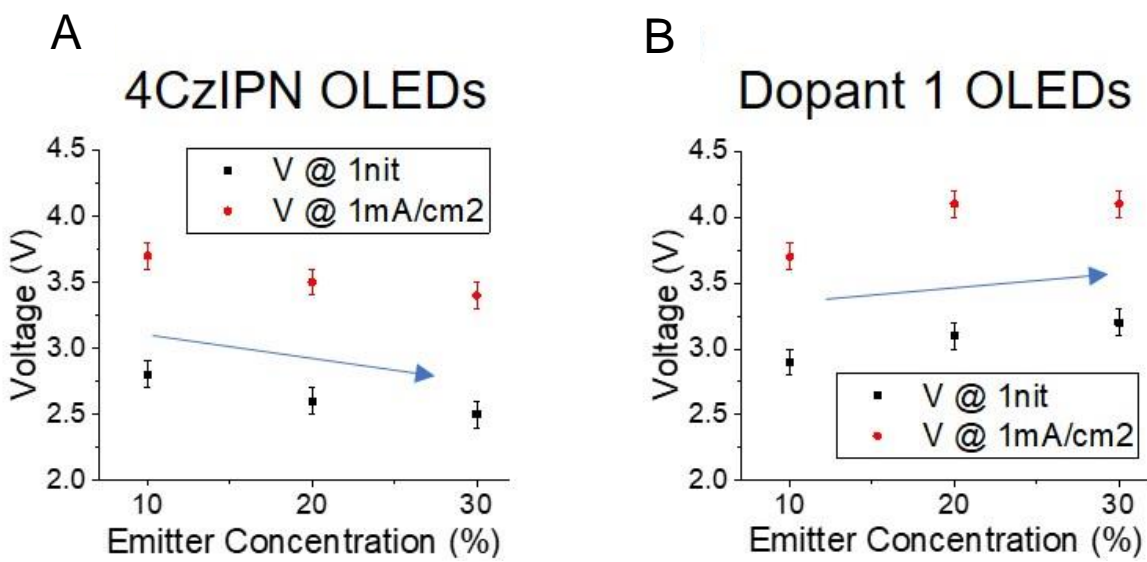
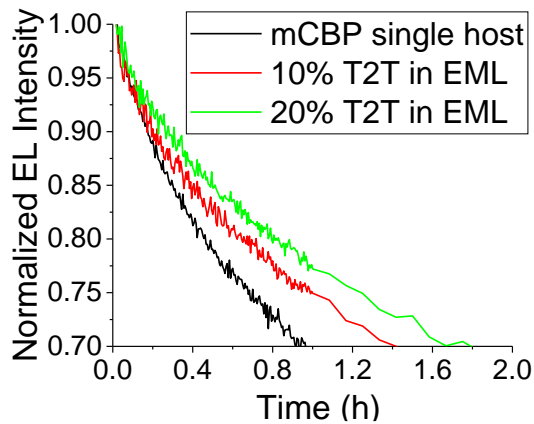
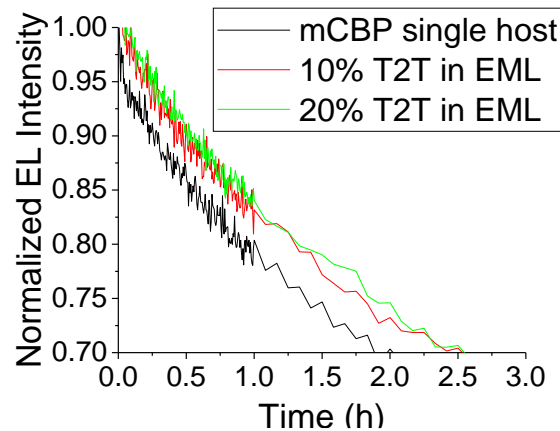


Figure 5-6. Drive voltages of OLED devices. A) 4CzIPN OLED devices. B) Dopant 1 OLED devices.

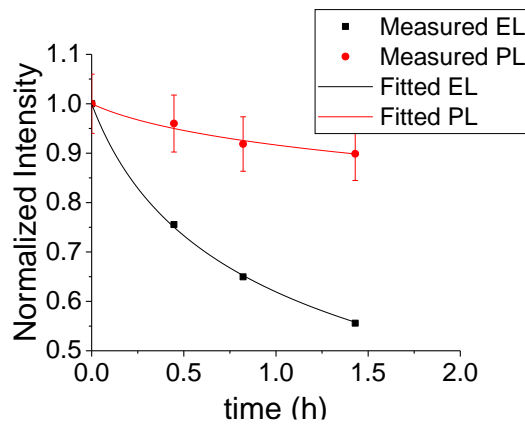
A 6% emitter concentration



30% emitter concentration

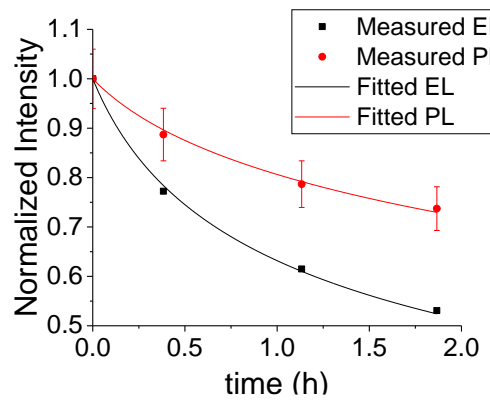


B 6% emitter, single host



$$L=2.6 \pm 0.1 \text{ nm}$$

6% emitter, 20% T2T in EML



$$6.5 \pm 0.2 \text{ nm}$$

Figure 5-7. The effect of a mixed host on the OLED stability and emission zone length. A) OLED EL degradation data from devices with a mixed host and two different emitter concentrations. B) Measured and fitted EL and PL degradation of low emitter concentration (6%) Dopant 1 devices with a single host and a mixed host with 20% T2T.

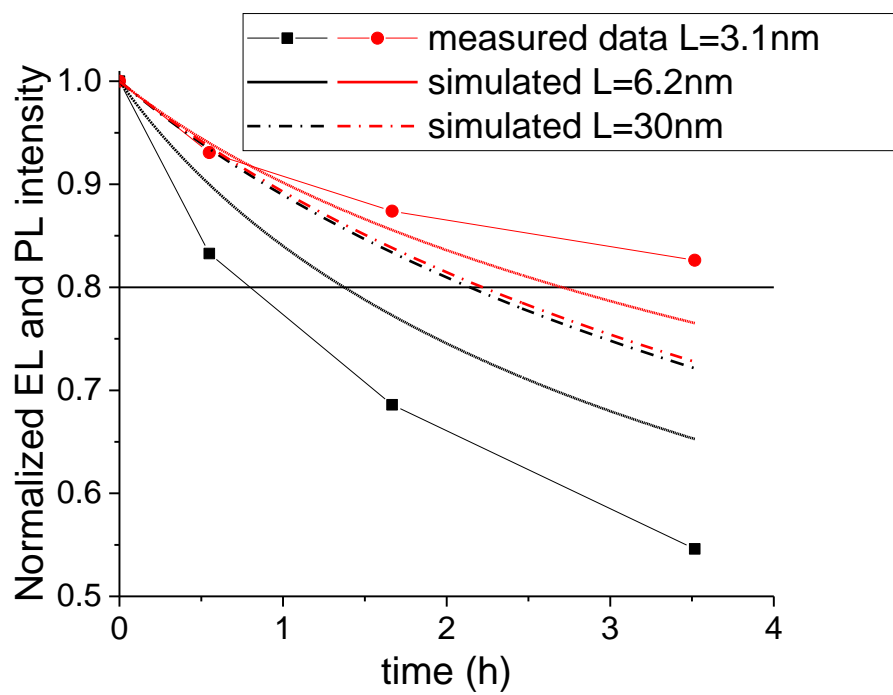


Figure 5-8. Simulated data with different effective emission zone lengths based on measured 10% emitter concentration single host Dopant 1 OLED data.

CHAPTER 6

SUMMARY AND FUTURE WORK

In this thesis, series of studies have been conducted on the fabrication and optical properties of corrugated OLEDs and on the degradation mechanisms of common OLEDs. Due to the high refractive indices of organic materials, ITO and glass, the light extraction efficiency of common bottom emission OLEDs is limited to 25-30%. And the operational stability of OLEDs still remains an issue. First, I gave a brief introduction on the optical properties of OLEDs and the dynamics of species in OLEDs.

Second, I introduce a simple process to fabricate a corrugated OLED containing a corrugated bilayer ETL. This corrugated bilayer ETL consists of two electron transport organic semiconductor materials with tremendously different glass transition temperatures. Due to the big difference in the thermal and the mechanical properties, upon annealing, bilayer corrugated structure forms. We show that the morphology of the corrugated structure can be tuned by the annealing temperature and the thicknesses of the two layers. We then demonstrate a corrugated OLED with the corrugated bilayer ETL. With an appropriate combination of materials and annealing temperature, we show that the corrugated OLED with a 35% higher current efficiency compared to a planar control OLED. Additionally, the operational lifetime of the corrugated OLED is greatly improved compared with the control device with the LT90 from 1000 cd/m² enhanced by 100 times.

Third, I talk about the methodology to derive the extraction efficiency of WG mode and SPP mode by using two-dimensional structures from angle-resolved spectra data of OLEDs. First, the semi-quantitative simulation of the angle-resolved spectra of OLEDs with ‘single-crystal’ structures is described. Second, the simulation is compared

with measured data to find the scattering strength. Third, the scattering strength is used to calculate the scattering efficiency of each mode. Fourth, the methodology is applied in the analysis of ‘poly-crystal’ structures.

Fourth, to understand the scattering efficiency, I conduct FDTD simulation to simulate the optical properties of corrugated OLEDs combined with electrical effect. The first section describes the optical and electrical simulation theory based on reciprocity theorem. The second section compares the extraction efficiency of TMWG of two different structures with dome shape and square shape structures. The third section compares the extraction efficiency of TMWG of two different structures with dome shape and hole shape structures.

Fifth, a new and simple methodology is introduced to quantitatively probe the emission zone of OLEDs by comparing the PL degradation of OLEDs with the EL degradation during continuous electrical operation. This methodology measures the emission zone on the original working device in a single run of stability test without adding additional layers in the device structure. This approach is first validated by investigating the emitter concentration effect on the stability of OLEDs using the well-known TADF emitter (4s,6s)-2,4,5,6-tetra(9H-carbazol-9-yl) isophthalonitrile (4CzIPN). The results are consistent with the results reported in the literature. We then applied this approach to investigate the emitter concentration effect on the stability of OLEDs using another TADF emitter 4-carbazolyl-2-methylisoindole-1,3-dione (Dopant 1). Based on our results, the Dopant 1 OLEDs show much less pronounced emitter concentration effect due to the relatively worse electron transport in the EML, compared with 4CzIPN

OLEDs. We were able to widen the emission zone by the use of a mixed host. The effect was confirmed by using the new methodology.

My work in this thesis only covers a small area of OLED study. There will be more future work on related topics. First, I will investigate on what is the best corrugation to extract SPP mode and WG mode. Second, I will investigate on the effect of corrugation on device stability. Third, it is interesting to see the Purcell effect of strong microcavities on device stability.

LIST OF REFERENCES

- (1) Myers, J. D.; Xue, J. G., Organic Semiconductors and their Applications in Photovoltaic Devices. *Polym. Rev.* **2012**, 52 (1), 1-37.
- (2) Mesta, M.; Carvelli, M.; de Vries, R. J.; van Eersel, H.; van der Holst, J. J. M.; Schober, M.; Furno, M.; Lussem, B.; Leo, K.; Loebel, P.; Coehoorn, R.; Bobbert, P. A., Molecular-scale simulation of electroluminescence in a multilayer white organic light-emitting diode. *Nat. Mater.* **2013**, 12 (7), 652-658.
- (3) Nayak, P. K., Exciton binding energy in small organic conjugated molecule. *Synth. Met.* **2013**, 174, 42-45.
- (4) Adachi, C.; Baldo, M. A.; Thompson, M. E.; Forrest, S. R., Nearly 100% internal phosphorescence efficiency in an organic light-emitting device. *J. Appl. Phys.* **2001**, 90 (10), 5048-5051.
- (5) Uoyama, H.; Goushi, K.; Shizu, K.; Nomura, H.; Adachi, C., Highly efficient organic light-emitting diodes from delayed fluorescence. *Nature* **2012**, 492 (7428), 234-+.
- (6) Park, Y.; Choong, V.; Gao, Y.; Hsieh, B. R.; Tang, C. W., Work function of indium tin oxide transparent conductor measured by photoelectron spectroscopy. *Appl. Phys. Lett.* **1996**, 68 (19), 2699-2701.
- (7) Schlaf, R.; Murata, H.; Kafafi, Z. H., Work function measurements on indium tin oxide films. *J. Electron Spectrosc. Relat. Phenom.* **2001**, 120 (1-3), 149-154.
- (8) Sugiyama, K.; Ishii, H.; Ouchi, Y.; Seki, K., Dependence of indium-tin-oxide work function on surface cleaning method as studied by ultraviolet and x-ray photoemission spectroscopies. *J. Appl. Phys.* **2000**, 87 (1), 295-298.
- (9) Chen, S. F.; Wang, C. W., Influence of the hole injection layer on the luminescent performance of organic light-emitting diodes. *Appl. Phys. Lett.* **2004**, 85 (5), 765-767.
- (10) You, H.; Dai, Y. F.; Zhang, Z. Q.; Ma, D. G., Improved performances of organic light-emitting diodes with metal oxide as anode buffer. *J. Appl. Phys.* **2007**, 101 (2).
- (11) Tang, C. W.; Vanslyke, S. A., Organic electroluminescent diodes. *Appl. Phys. Lett.* **1987**, 51 (12), 913-915.
- (12) Jabbour, G. E.; Kippelen, B.; Armstrong, N. R.; Peyghambarian, N., Aluminum based cathode structure for enhanced electron injection in electroluminescent organic devices. *Appl. Phys. Lett.* **1998**, 73 (9), 1185-1187.
- (13) Song, W. J.; So, S. K.; Wong, K. W.; Choi, W. K.; Cao, L. L., Study of lithium fluoride/tris(8-hydroxyquinolino)-aluminum interfacial chemistry using XPS and ToF-SIMS. *Appl. Surf. Sci.* **2004**, 228 (1-4), 373-377.

- (14) Lussem, B.; Riede, M.; Leo, K., Doping of organic semiconductors. *Phys. Status Solidi A* **2013**, *210* (1), 9-43.
- (15) Ikai, M.; Tokito, S.; Sakamoto, Y.; Suzuki, T.; Taga, Y., Highly efficient phosphorescence from organic light-emitting devices with an exciton-block layer. *Appl. Phys. Lett.* **2001**, *79* (2), 156-158.
- (16) Synowicki, R. A., Spectroscopic ellipsometry characterization of indium tin oxide film microstructure and optical constants. *Thin Solid Films* **1998**, *313*, 394-397.
- (17) Saxena, K.; Jain, V. K.; Mehta, D. S., A review on the light extraction techniques in organic electroluminescent devices. *Opt. Mater.* **2009**, *32* (1), 221-233.
- (18) Salehi, A.; Ho, S.; Chen, Y.; Peng, C.; Yersin, H.; So, F., Highly Efficient Organic Light-Emitting Diode Using A Low Refractive Index Electron Transport Layer. *Adv. Opt. Mater.* **2017**, *5* (11).
- (19) Barnes, W. L., Fluorescence near interfaces: the role of photonic mode density. *J. Mod. Opt.* **1998**, *45* (4), 661-699.
- (20) Bulovic, V.; Khalfin, V. B.; Gu, G.; Burrows, P. E.; Garbuzov, D. Z.; Forrest, S. R., Weak microcavity effects in organic light-emitting devices. *Phys. Rev. B* **1998**, *58* (7), 3730-3740.
- (21) Lu, M. H.; Sturm, J. C., Optimization of external coupling and light emission in organic light-emitting devices: modeling and experiment. *J. Appl. Phys.* **2002**, *91* (2), 595-604.
- (22) Brutting, W.; Frischeisen, J.; Schmidt, T. D.; Scholz, B. J.; Mayr, C., Device efficiency of organic light-emitting diodes: Progress by improved light outcoupling. *Phys. Status Solidi A* **2013**, *210* (1), 44-65.
- (23) Kim, Y. H.; Lee, J.; Kim, W. M.; Fuchs, C.; Hofmann, S.; Chang, H. W.; Gather, M. C.; Muller-Meskamp, L.; Leo, K., We Want Our Photons Back: Simple Nanostructures for White Organic Light-Emitting Diode Outcoupling. *Adv. Funct. Mater.* **2014**, *24* (17), 2553-2559.
- (24) Koo, W. H.; Jeong, S. M.; Araoka, F.; Ishikawa, K.; Nishimura, S.; Toyooka, T.; Takezoe, H., Light extraction from organic light-emitting diodes enhanced by spontaneously formed buckles. *Nat. Photonics* **2010**, *4* (4), 222-226.
- (25) Xiang, C. Y.; Koo, W.; So, F.; Sasabe, H.; Kido, J., A systematic study on efficiency enhancements in phosphorescent green, red and blue microcavity organic light emitting devices. *Light: Sci. Appl.* **2013**, *2*.
- (26) Penninck, L.; Mladenowski, S.; Neyts, K., The effects of planar metallic interfaces on the radiation of nearby electrical dipoles. *J. Opt.* **2010**, *12* (7).

- (27) Chutinan, A.; Ishihara, K.; Asano, T.; Fujita, M.; Noda, S., Theoretical analysis on light-extraction efficiency of organic light-emitting diodes using FDTD and mode-expansion methods. *Org. Electron.* **2005**, 6 (1), 3-9.
- (28) Lee, Y. J.; Kim, S. H.; Huh, J.; Kim, G. H.; Lee, Y. H.; Cho, S. H.; Kim, Y. C.; Do, Y. R., A high-extraction-efficiency nanopatterned organic light-emitting diode. *Appl. Phys. Lett.* **2003**, 82 (21), 3779-3781.
- (29) Yee, K. S., Numerical solution of initial boundary value problems involving Maxwell's equations in isotropic media. *IEEE Trans. Antennas Propag.* **1966**, AP14 (3), 302-&.
- (30) So, S. K.; Choi, W. K.; Cheng, C. H.; Leung, L. M.; Kwong, C. F., Surface preparation and characterization of indium tin oxide substrates for organic electroluminescent devices. *Appl. Phys. A: Mater. Sci. Process.* **1999**, 68 (4), 447-450.
- (31) Forrest, S. R.; Bradley, D. D. C.; Thompson, M. E., Measuring the efficiency of organic light-emitting devices. *Adv. Mater.* **2003**, 15 (13), 1043-1048.
- (32) Coulson, C. A.; Rushbrooke, G. S., Note on the method of molecular orbitals. *Proc. Cambridge Philos. Soc.* **1940**, 36, 193-200.
- (33) Peng, C.; Liu, S. Y.; Fu, X. Y.; Pan, Z. X.; Chen, Y.; So, F.; Schanze, K. S., Corrugated Organic Light Emitting Diodes Using Low T-g Electron Transporting Materials. *ACS Appl. Mater. Interfaces* **2016**, 8 (25), 16192-16199.
- (34) Koo, W. H.; Boo, S.; Jeong, S. M.; Nishimura, S.; Araoka, F.; Ishikawa, K.; Toyooka, T.; Takezoe, H., Controlling buckling structure by UV/ozone treatment for light extraction from organic light emitting diodes. *Org. Electron.* **2011**, 12 (7), 1177-1183.
- (35) Koo, W. H.; Zhe, Y.; So, F., Direct Fabrication of Organic Light-Emitting Diodes on Buckled Substrates for Light Extraction. *Adv. Opt. Mater.* **2013**, 1 (5), 404-408.
- (36) Park, B.; Jeon, H. G., Spontaneous buckling in flexible organic light-emitting devices for enhanced light extraction. *Opt. Express* **2011**, 19 (19), A1117-A1125.
- (37) Kim, J.; Lee, H. H., Wave formation by heating in thin metal film on an elastomer. *J. Polym. Sci., Part B: Polym. Phys.-Polymer Physics* **2001**, 39 (11), 1122-1128.
- (38) Simba, R.; Boyer, R. F., On a General Relation Involving the Glass Temperature and Coefficients of Expansion of Polymers. *J. Chem. Phys.* **1962**, 37 (5).
- (39) Kulkarni, A. P.; Tonzola, C. J.; Babel, A.; Jenekhe, S. A., Electron transport materials for organic light-emitting diodes. *Chem. Mater.* **2004**, 16 (23), 4556-4573.
- (40) Fenter, P.; Schreiber, F.; Bulovic, V.; Forrest, S. R., Thermally induced failure mechanisms of organic light emitting device structures probed by X-ray specular reflectivity. *Chem. Phys. Lett.* **1997**, 277 (5-6), 521-526.

- (41) Crispin, X.; Jakobsson, F. L. E.; Crispin, A.; Grim, P. C. M.; Andersson, P.; Volodin, A.; van Haesendonck, C.; Van der Auweraer, M.; Salaneck, W. R.; Berggren, M., The origin of the high conductivity of poly(3,4-ethylenedioxythiophene)-poly(styrenesulfonate) (PEDOT-PSS) plastic electrodes. *Chem. Mater.* **2006**, *18* (18), 4354-4360.
- (42) Goushi, K.; Kwong, R.; Brown, J. J.; Sasabe, H.; Adachi, C., Triplet exciton confinement and unconfinement by adjacent hole-transport layers. *J. Appl. Phys.* **2004**, *95* (12), 7798-7802.
- (43) Reineke, S.; Lindner, F.; Schwartz, G.; Seidler, N.; Walzer, K.; Lussem, B.; Leo, K., White organic light-emitting diodes with fluorescent tube efficiency. *Nature* **2009**, *459* (7244), 234-U116.
- (44) Goushi, K.; Yoshida, K.; Sato, K.; Adachi, C., Organic light-emitting diodes employing efficient reverse intersystem crossing for triplet-to-singlet state conversion. *Nat. Photonics* **2012**, *6* (4), 253-258.
- (45) Scholz, S.; Kondakov, D.; Lussem, B.; Leo, K., Degradation Mechanisms and Reactions in Organic Light-Emitting Devices. *Chem. Rev.* **2015**, *115* (16), 8449-8503.
- (46) Aziz, H.; Popovic, Z. D., Degradation phenomena in small-molecule organic light-emitting devices. *Chem. Mater.* **2004**, *16* (23), 4522-4532.
- (47) Zhou, X.; He, J.; Liao, L. S.; Lu, M.; Ding, X. M.; Hou, X. Y.; Zhang, X. M.; He, X. Q.; Lee, S. T., Real-time observation of temperature rise and thermal breakdown processes in organic LEDs using an IR imaging and analysis system. *Adv. Mater.* **2000**, *12* (4), 265-269.
- (48) Worthing, P. T.; Barnes, W. L., Efficient coupling of surface plasmon polaritons to radiation using a bi-grating. *Appl. Phys. Lett.* **2001**, *79* (19), 3035-3037.
- (49) Fuchs, C.; Schwab, T.; Roch, T.; Eckardt, S.; Lasagni, A.; Hofmann, S.; Lussem, B.; Muller-Meskamp, L.; Leo, K.; Gather, M. C.; Scholz, R., Quantitative allocation of Bragg scattering effects in highly efficient OLEDs fabricated on periodically corrugated substrates. *Opt. Express* **2013**, *21* (14), 16319-16330.
- (50) Frischeisen, J.; Niu, Q. A.; Abdellah, A.; Kinzel, J. B.; Gehlhaar, R.; Scarpa, G.; Adachi, C.; Lugli, P.; Brutting, W., Light extraction from surface plasmons and waveguide modes in an organic light-emitting layer by nanoimprinted gratings. *Opt. Express* **2011**, *19* (1), A7-A19.
- (51) Schwab, T.; Fuchs, C.; Scholz, R.; Zakhidov, A.; Leo, K.; Gather, M. C., Coherent mode coupling in highly efficient top-emitting OLEDs on periodically corrugated substrates. *Opt. Express* **2014**, *22* (7), 7524-7537.

- (52) Zhang, S. Y.; Martins, E. R.; Diyaf, A. G.; Wilson, J. I. B.; Turnbull, G. A.; Samuel, I. D. W., Calculation of the emission power distribution of microstructured OLEDs using the reciprocity theorem. *Synth. Met.* **2015**, 205, 127-133.
- (53) Zhang, X. L.; Feng, J.; Song, J. F.; Li, X. B.; Sun, H. B., Grating amplitude effect on electroluminescence enhancement of corrugated organic light-emitting devices. *Opt. Lett.* **2011**, 36 (19), 3915-3917.
- (54) Kim, J. W.; Jang, J. H.; Oh, M. C.; Shin, J. W.; Cho, D. H.; Moon, J. H.; Lee, J. I., FDTD analysis of the light extraction efficiency of OLEDs with a random scattering layer. *Opt. Express* **2014**, 22 (1), 498-507.
- (55) Lamansky, S.; Djurovich, P.; Murphy, D.; Abdel-Razzaq, F.; Lee, H. E.; Adachi, C.; Burrows, P. E.; Forrest, S. R.; Thompson, M. E., Highly phosphorescent bis-cyclometalated iridium complexes: Synthesis, photophysical characterization, and use in organic light emitting diodes. *J. Am. Chem. Soc.* **2001**, 123 (18), 4304-4312.
- (56) Adachi, C.; Baldo, M. A.; Forrest, S. R.; Lamansky, S.; Thompson, M. E.; Kwong, R. C., High-efficiency red electrophosphorescence devices. *Appl. Phys. Lett.* **2001**, 78 (11), 1622-1624.
- (57) Lee, J.; Chen, H. F.; Batagoda, T.; Coburn, C.; Djurovich, P. I.; Thompson, M. E.; Forrest, S. R., Deep blue phosphorescent organic light-emitting diodes with very high brightness and efficiency. *Nat. Mater.* **2016**, 15 (1), 92-+.
- (58) Fleetham, T.; Li, G. J.; Li, J., Phosphorescent Pt(II) and Pd(II) Complexes for Efficient, High-Color-Quality, and Stable OLEDs. *Adv. Mater.* **2017**, 29 (5).
- (59) Miwa, T.; Kubo, S.; Shizu, K.; Komino, T.; Adachi, C.; Kaji, H., Blue organic light-emitting diodes realizing external quantum efficiency over 25% using thermally activated delayed fluorescence emitters. *Sci. Rep.* **2017**, 7.
- (60) Scholz, S.; Kondakov, D.; Luessem, B.; Leo, K., Degradation Mechanisms and Reactions in Organic Light-Emitting Devices. *Chem. Rev.* **2015**, 115 (16), 8449-8503.
- (61) Kim, M.; Jeon, S. K.; Hwang, S. H.; Lee, J. Y., Stable Blue Thermally Activated Delayed Fluorescent Organic Light-Emitting Diodes with Three Times Longer Lifetime than Phosphorescent Organic Light-Emitting Diodes. *Adv. Mater.* **2015**, 27 (15), 2515-2520.
- (62) Coburn, C.; Lee, J.; Forrest, S. R., Charge Balance and Exciton Confinement in Phosphorescent Organic Light Emitting Diodes. *Adv. Opt. Mater.* **2016**, 4 (6), 889-895.
- (63) Song, W.; Lee, W.; Kim, K. K.; Lee, J. Y., Correlation of doping concentration, charge transport of host, and lifetime of thermally activated delayed fluorescent devices. *Org. Electron.* **2016**, 37, 252-256.

- (64) Zhang, Y. F.; Lee, J.; Forrest, S. R., Tenfold increase in the lifetime of blue phosphorescent organic light-emitting diodes. *Nat. Commun.* **2014**, 5.
- (65) Giebink, N. C.; D'Andrade, B. W.; Weaver, M. S.; Mackenzie, P. B.; Brown, J. J.; Thompson, M. E.; Forrest, S. R., Intrinsic luminance loss in phosphorescent small-molecule organic light emitting devices due to bimolecular annihilation reactions. *J. Appl. Phys.* **2008**, 103 (4), 9.
- (66) Popovic, Z. D.; Aziz, H.; Hu, N. X.; Ioannidis, A.; dos Anjos, P. N. M., Simultaneous electroluminescence and photoluminescence aging studies of tris(8-hydroxyquinoline) aluminum-based organic light-emitting devices. *J. Appl. Phys.* **2001**, 89 (8), 4673-4675.
- (67) Zhang, Y. J.; Aziz, H., Degradation Mechanisms in Blue Phosphorescent Organic Light Emitting Devices by Exciton-Polaron Interactions: Loss in Quantum Yield versus Loss in Charge Balance. *ACS Appl. Mater. Interfaces* **2017**, 9 (1), 636-643.
- (68) Nakanotani, H.; Masui, K.; Nishide, J.; Shibata, T.; Adachi, C., Promising operational stability of high-efficiency organic light-emitting diodes based on thermally activated delayed fluorescence. *Sci. Rep.* **2013**, 3, 5.
- (69) Tsang, D. P. K.; Adachi, C., Operational stability enhancement in organic light-emitting diodes with ultrathin Liq interlayers. *Sci. Rep.* **2016**, 6, 9.
- (70) Seino, Y.; Inomata, S.; Sasabe, H.; Pu, Y. J.; Kido, J., High-Performance Green OLEDs Using Thermally Activated Delayed Fluorescence with a Power Efficiency of over 100 lm W-1. *Adv. Mater.* **2016**, 28 (13), 2638--.
- (71) Komatsu, R.; Sasabe, H.; Inomata, S.; Pu, Y. J.; Kido, J., High efficiency solution processed OLEDs using a thermally activated delayed fluorescence emitter. *Synth. Met.* **2015**, 202, 165-168.
- (72) Sandanayaka, A. S. D.; Matsushima, T.; Adachi, C., Degradation Mechanisms of Organic Light-Emitting Diodes Based on Thermally Activated Delayed Fluorescence Molecules. *J. Phys. Chem. C* **2015**, 119 (42), 23845-23851.
- (73) Kim, Y. K.; Kim, J. W.; Park, Y., Energy level alignment at a charge generation interface between 4,4(')-bis(N-phenyl-1-naphthylamino)biphenyl and 1,4,5,8,9,11-hexaaazatriphenylene-hexacarbonitrile. *Appl. Phys. Lett.* **2009**, 94 (6), 3.
- (74) Kim, B. S.; Lee, J. Y., Engineering of Mixed Host for High External Quantum Efficiency above 25% in Green Thermally Activated Delayed Fluorescence Device. *Adv. Funct. Mater.* **2014**, 24 (25), 3970-3977.
- (75) Chu, X. B.; Guan, M.; Niu, L. T.; Zhang, Y.; Li, Y. Y.; Liu, X. F.; Zeng, Y. P., The utilization of low-temperature evaporable CsN₃-doped NBphen as an alternative and efficient electron-injection layer in OLED. *Phys. Status Solidi A* **2014**, 211 (7), 1605-1609.

BIOGRAPHICAL SKETCH

Cheng Peng (彭骋) was born in Urumqi, Xinjiang, China. After graduating from Urumqi No.1 High School, he went to Peking University in Beijing, China for his B.S. in physics. In 2012, he came to United States and started graduate school in University of Florida in Gainesville, Florida. In this Ph. D. program, he did research focused on organic semiconductors and opto-electronics devices in materials science and engineering.